VOLUME 7 NUMBER 2 2016 ISSN 2218-7987

International Journal of Mathematics and Physics

Al-Farabi Kazakh National University

International Journal of Mathematics and Physics is publishing two numbers in a year by al-Farabi Kazakh National University, al-Farabi ave., 71, 050040, Almaty, the Republic of Kazakhstan
website: http://ijmph.kaznu.kz/

Any inquiry for subscriptions should be send to:
Prof. Tlekkabul Ramazanov, al-Farabi Kazakh National University
al-Farabi ave., 71, 050040, Almaty, the Republic of Kazakhstan
e-mail: Tlekkabul.Ramazanov@kaznu.kz

Printed in Kazakhstan

Editorial

The most significant scientific achievements are attained through joint efforts of different sciences, mathematics and physics are among them. Therefore publication of the Journal, which shows results of current investigations in the field of mathematics and physics, will allow wider exhibition of scientific problems, tasks and discoveries.

One of the basic goals of the Journal is to promote extensive exchange of information between scientists from all over the world. We propose publishing service for original papers and materials of Mathematical and Physical Conferences (by selection) held in different countries and in the Republic of Kazakhstan.

Creation of the special International Journal of Mathematics and Physics is of great importance because a vast amount of scientists are willing to publish their articles and it will help to widen the geography of future dissemination. We will also be glad to publish papers of scientists from all the continents.

The Journal will publish experimental and theoretical investigations on Mathematics, Physical Technology and Physics. Among the subject emphasized are modern problems of Calculus Mathematics, Algebra and Mathematical Analysis, Differential Equations and Mechanics, Informatics and Mathematical Modeling, Calculus of Approximations and Program Systems, Astronomy and Space Research, Theoretical Physics and Plasma Physics, Chemical Physics and Radio Physics, Thermophysics, Nuclear Physics and Nanotechnology.

The Journal is issued on the base of al-Farabi Kazakh National University. Leading scientists from different countries of the world agreed to join the Editorial Board of the Journal.

The Journal will be published two times a year by al-Farabi Kazakh National University. We hope to receive papers from many laboratories which are interested in applications of the scientific principles of mathematics and physics and are carrying out researches on such subjects as production of new materials or technological problems.

UDC 519.6, 504.3.054

*Zhakebayev D., Abdibekova A., Dyuisaliyev Ye.

Faculty of Mechanics and Mathematics,
al-Farabi Kazakh National University, Almaty, Kazakhstan
*e-mail: dauren.zhakebaev@kaznu.kz

Numerical modeling of the spreading oil slick in the Caspian Sea

Abstract. This paper considers the process of filling and migration of fossil fuels - oil - in the Caspian Sea, depending on the weather conditions. As a rule, for environmentalists performing analysis of the emergency, it is necessary to know in which direction will move the oil slick, how to change the composition of the oil, how much oil will evaporate and a number of other questions that can be answered using mathematical modeling. The theoretical basis of a mathematical model for the process consists of the hydrodynamics equations of the sea, equations of transfer and changes in the concentration of the oil component, as well as the continuity equation is taken into account, expressing the an invariance of the total amount of mass of poured oil, which have formed a film on the surface of the sea. As a result, the migration trajectory, the change in concentration and temperature of the oil slick on the sea surface from a fixed source, depending on weather conditions are defined. This model allows to calculate the area and determine the migration trajectory of the oil slick on the Caspian Sea depending on the weather conditions, and carry out the numerical simulation of oil spills in the open sea at different initial masses of spilled oil.

Key words: oil spill, the Caspian Sea, oil slick, marine environment, weather conditions, mathematical modeling, oil migration, concentration of oil, numerical simulation.

Development and mastering of oil fields on the Caspian shelf represent the production of the increased risk of environmental pollution for the Caspian Sea and the environment of the surrounding areas. Any high-tech production is not insured from accidents, and in case of emergencies, the consequences can cause irreversible processes in the environment [1-4].

The real concern for the condition of the ecological environment is the multinational oil companies in relation to the protection of the environment and the sea. The program of the companies stated that in the event of a spill of a small amount of oil in the open sea, the oil will evaporate, and the case of a significant oil spill in the open sea it will be set on fire and the event of a disaster will be delivered from the UK special equipment for collecting oil, and even indicated delivery time after the accident - 20-24 hours.

According to preliminary calculations, this time is enough, with a fair wind to oil was in the coastal zone in the rushes, where it is not possible to collect [5, 6]. This carefree attitude of oil companies to environmental causes, at least, puzzling.

So currently requires new approaches to tackle the problem. This new direction is the development of methods and algorithms for the direct numerical simulation of Aero-and hydrodynamics to environmental problems when ahead in unsteady mode to follow the development of events, actually occurring in nature. Since the research is conducted on the up-to-date computer technologies and high speed of modern computers allows to stay ahead of the real physical process. At the moment time a considerable amount of work in the field of numerical simulation of pollution and oil spill, but all the research works were limited to modeling based on single-speed mathematical model.

In this paper the mathematical modeling of the spreading oil slick on the surface of the Caspian Sea with an air temperature of 200 C, at rest is considered.

For this two-dimensional mathematical model of a three-component model based on the motion equations of the multiphase medium, taking into account the velocity components of the "gas-oil-water" was examined. Figure 1 shows a multiphase environment where green is colored region of the air flow over the sea- "gas", the blue color shows the oil slick - "oil" is having physical properties of a viscous liquid, and the areadressed in red is sea water – "water".

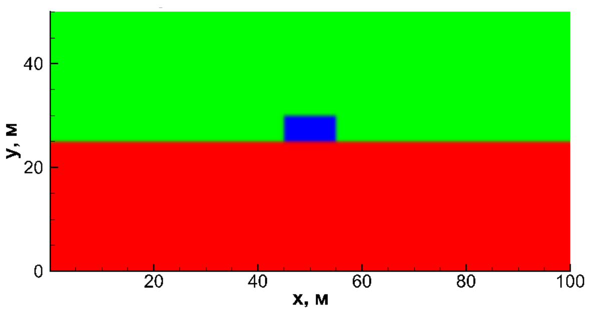

Figure 1 – Schematic illustration of the problem statement

Mathematical modeling

The theoretical basis of mathematical models for the process of the spreading of the oil slick based on the solution of the continuity equation for each component, the continuity equation for the mixture momentum equation:

$$\begin{cases} \dfrac{\partial \rho_k}{\partial t} + \operatorname{div} \rho_k \mathrm{v}_k = 0, \quad k = 1 \ldots N, & (1) \\ \operatorname{div} \mathrm{v} = 0, & (2) \\ \rho \dfrac{\partial \mathrm{v}}{\partial t} + \rho \nabla \cdot (\mathrm{v} \otimes \mathrm{v}) = -\nabla p + \nabla \tau + f, & (3) \end{cases}$$

where v_k – speed of movement components; v – speed mix; p – pressure; $f = (0, -\rho g)$ – vector of external forces; g – acceleration of free fall.

The real ρ_k^0 density of the components is defined as the weight of the k -th component in the unit volume of the component. In turn, the density (partial density) component ρ_k is the mass per unit volume of the components of the mixture. The volume fraction of the components is defined as the ratio of the components to the volume of the mixture:

$$\sum_{k=1}^{N} c_k = 1, \tag{4}$$

$$\rho_k = c_k \rho_k^0, \quad k = 1 \ldots N, \tag{5}$$

and the mixture density ρ is determined by the law

$$\rho = \sum_{k=1}^{N} \rho_k \tag{6}$$

Using (5), the first equation (1) can be obtained in terms of the continuity equation of the volume fraction

$$\frac{\partial c_k}{\partial t} + \operatorname{div} c_k \mathrm{v}_k = 0, \quad k = 1 \ldots N, \tag{7}$$

the sum of which gives equation (2). As the speed of the mixture is taken to be the volumetric average velocity

$$\mathrm{v} = \sum_{k=1}^{N} c_k \mathrm{v}_k \tag{8}$$

The viscous stress tensor τ, which is considered for non-Newtonian fluids is given by:

$$\tau = \mu_e D, \tag{9}$$

$$\begin{gathered} \mu_e = \mu_e(\dot\gamma), \quad \dot\gamma = \sqrt{\frac{1}{2} D \cdot D}, \\ D = D_{\mathrm{i,j}} = \frac{\partial \mathrm{v_i}}{\partial \mathrm{x_j}} + \frac{\partial \mathrm{v_j}}{\partial \mathrm{x_i}} \end{gathered} \tag{10}$$

Non-Newtonian fluids: $\mu_e = (\tau_0 + k\dot\gamma)\dot\gamma^{-1}$– Bingham fluid, where τ_0 – the yield stress of visco-plastic fluid; $\dot\gamma$ - shear rate; n, k – parameters of rheological models.

The dynamic viscosity μ of the mixture is determined linearly

$$\mu = \sum_{k=1}^{N} c_k \mu_k \tag{11}$$

where μ_k – the dynamic viscosity of the k – thcomponents.

Components such as gas bubbles or solid particles are considered as the dispersed ($k \in K_{dispersed}$), and others – the carrying ($k \in K_{carrier}$). Phase carriers move with the same speed $v^{carrier}$:

$$\mathrm{v}_k = \mathrm{v}^{\mathrm{carrier}}, \quad k \in K_{carrier} \tag{12}$$

the velocity difference between the dispersed and carrying phases are determined by Stokes' law:

$$\mathrm{v}_k = \mathrm{v}^{\mathrm{carrier}} + u_k^{settling}, \quad k \in K_{carrier} \tag{13}$$

$$u_k^{settling} = \frac{(\rho_k^0 - \rho) \cdot d_k^2}{18\mu} g, \tag{14}$$

where d_k – the diameter of the dispersed k phase particles

Substituting (12) and (13) a definition (8) gives

$$\mathrm{v} = \mathrm{v}^{\text{carrier}} + \sum_{k \in K_{dispersed}} c_k u_k^{settling}. \tag{15}$$

This yields an expression for the speed of the carrier phase through high speed mixture

$$\mathrm{v}^{\text{carrier}} = \mathrm{v} - \sum_{k \in K_{dispersed}} c_k u_k^{settling}. \tag{16}$$

Speed disperse phase is now explicitly computed from (13).

The initial and boundary conditions:

At the initial moment of the bottom half of the area is sea water $(c_{water} = 1)$.

On the surface of the sea water is the oil column with dimensions 10×5 м $(c_{oil} = 1)$, in other points of the region is the air $(c_{air} = 1)$.

The boundary conditions imply an appeal to zero speed at the lower boundary, and other boundaries are turning to zero only the wall normal component of velocity.

The numerical algorithm

Numerical implementation of the model is composed by the following algorithm: at the first stage, the Navier-Stokes equation is solved without taken pressure into account, at the second stage the Poisson equation for pressure is solved, derived from the continuity equation with given velocity fields from the first stage, by using the matrix sweep method. The obtained pressure field in the next stage is used to recalculate the final velocity field [7]. At the fourth stage the concentration equation for of the components of a viscous liquid is solved according to the defined velocity field. At the last stage the equation for concentration of the components of a viscous liquid is solved according to the final recalculated velocity field.

The intermediate velocity field is defined by using the Crank-Nicholson scheme in combination with a five-point sweep method.

The horizontal component component of velocity at the grid point $\left(i + \frac{1}{2} j\right)$:

$$\frac{\partial u_1}{\partial \tau} + \frac{\partial (u_1 u_1)}{\partial x_1} + \frac{\partial (u_1 u_2)}{\partial x_2} = \frac{1}{\mathrm{Re}} \left(\frac{\partial^2 u_1}{\partial x_1^2} + \frac{\partial^2 u_1}{\partial x_2^2} \right) \tag{17}$$

Equation (17) at the application of the scheme Crank-Nicholson takes the following form

$$\begin{gathered} \hat{u}^{n+1}_{1\, i+\frac{1}{2} j} - u^{n}_{1\, i+\frac{1}{2} j} = -\frac{3\tau}{2} [hx]^n_{i+\frac{1}{2} j} + \frac{\tau}{2} [hxp]^{n-1}_{i+\frac{1}{2} j} + \\ + \tau [ax]^n_{i+\frac{1}{2} j} + \frac{\tau}{2} \cdot \frac{1}{\mathrm{Re}} \cdot \left(\frac{\partial^2 \hat{u}_1}{\partial x_1^2} \right)^{n+1}_{i+\frac{1}{2} j} + \frac{\tau}{2} \cdot \frac{1}{\mathrm{Re}} \cdot \left(\frac{\partial^2 \hat{u}_1}{\partial x_2^2} \right)^{n+1}_{i+\frac{1}{2} j} \end{gathered} \tag{18}$$

where

$$[hx]^n_{i+\frac{1}{2} j} = \left(\frac{\partial u_1 u_1}{\partial x_1} \right)^n_{i+\frac{1}{2} j} + \left(\frac{\partial u_1 u_2}{\partial x_2} \right)^n_{i+\frac{1}{2} j}$$

$$[hxp]^{n-1}_{i+\frac{1}{2} j} = \left(\frac{\partial u_1 u_1}{\partial x_1} \right)^{n-1}_{i+\frac{1}{2} j} + \left(\frac{\partial u_1 u_2}{\partial x_2} \right)^{n-1}_{i+\frac{1}{2} j}$$

$$[ax]^n_{i+\frac{1}{2} j} = \frac{1}{2} \cdot \frac{1}{\mathrm{Re}} \cdot \left[\left(\frac{\partial^2 u_1}{\partial x_1^2} \right)^n_{i+\frac{1}{2} j} + \left(\frac{\partial^2 u_1}{\partial x_2^2} \right)^n_{i+\frac{1}{2} j} \right]$$

Then the left side of the equation (18) is denoted by $q_{i+\frac{1}{2} j}$

$$q_{i+\frac{1}{2} j} \equiv \hat{u}^{n+1}_{1\, i+\frac{1}{2} j} - u^{n}_{1\, i+\frac{1}{2} j} \tag{19}$$

Component $\hat{u}^{n+1}_{1\, i+\frac{1}{2} j}$ is found from the equation (19)

$$\hat{u}^{n+1}_{1\, i+\frac{1}{2} j} = q_{i+\frac{1}{2} j} + u^{n}_{1\, i+\frac{1}{2} j}$$

Replacing all $\hat{u}^{n+1}_{1\, i+\frac{1}{2} j}$ from the equation (18) takes the following form

$$\begin{gathered} q_{i+\frac{1}{2} j} - \frac{\tau}{2} \cdot \frac{1}{\mathrm{Re}} \cdot \left(\frac{\partial^2 q}{\partial x_1^2} \right)^{n+1}_{i+\frac{1}{2} j} - \frac{\tau}{2} \cdot \frac{1}{\mathrm{Re}} \cdot \left(\frac{\partial^2 q}{\partial x_2^2} \right)^{n+1}_{i+\frac{1}{2} j} = \\ = -\frac{3\tau}{2} [hx]^n_{i+\frac{1}{2} j} + \frac{\tau}{2} [hxp]^{n-1}_{i+\frac{1}{2} j} + 2 \cdot \tau [ax]^n_{i+\frac{1}{2} j} \end{gathered} \tag{20}$$

The equation (20) looks in the following way

$$\left[1 - \frac{\tau}{2} \cdot \frac{1}{\mathrm{Re}} \cdot \frac{\partial^2}{\partial x_1^2} - \frac{\tau}{2} \cdot \frac{1}{\mathrm{Re}} \cdot \frac{\partial^2}{\partial x_2^2} \right] q_{i+\frac{1}{2} j} = d_{i+\frac{1}{2} j} \tag{21}$$

where

$$d_{i+\frac{1}{2}j} = -\frac{3\tau}{2}\left[hx\right]^{n}_{i+\frac{1}{2}j} + \frac{\tau}{2}\left[hxp\right]^{n-1}_{i+\frac{1}{2}j} + 2\cdot\tau\left[ax\right]^{n}_{i+\frac{1}{2}j}$$

To obtain the second order of accuracy with respect to time:

$$\left[1-\frac{\tau}{2}\cdot\frac{1}{\mathrm{Re}}\cdot\frac{\partial^2}{\partial x_1^2}\right]\left[1-\frac{\tau}{2}\cdot\frac{1}{\mathrm{Re}}\cdot\frac{\partial^2}{\partial x_2^2}\right]q_{i+\frac{1}{2}j} = d_{i+\frac{1}{2}j} \qquad (22)$$

To determine $q_{i+\frac{1}{2}j}$ the equation (22) is solved in 2 stages.

$$\left[1-\frac{\tau}{2}\cdot\frac{1}{\mathrm{Re}}\cdot\frac{\partial^2}{\partial x_1^2}\right]A_{i+\frac{1}{2}j} = d_{i+\frac{1}{2}j}$$

$$\left[1-\frac{\tau}{2}\cdot\frac{1}{\mathrm{Re}}\cdot\frac{\partial^2}{\partial x_2^2}\right]q_{i+\frac{1}{2}j} = A_{i+\frac{1}{2}j}$$

The first stage $A_{i+\frac{1}{2}j}$ is searched in the direction of x_1 coordinates:

$$\left[1-\frac{\tau}{2}\cdot\frac{1}{\mathrm{Re}}\cdot\frac{\partial^2}{\partial x_1^2}\right]A_{i+\frac{1}{2}j} = d_{i+\frac{1}{2}j}$$

$$A^{n+1}_{i+\frac{1}{2}j} - \frac{\tau}{2}\cdot\frac{1}{\mathrm{Re}}\cdot\left(\frac{\partial^2 A}{\partial x_1^2}\right)^{n+1}_{i+\frac{1}{2}j} = d_{i+\frac{1}{2}j}$$

$$A^{n+1}_{i+\frac{1}{2}j} - \frac{\tau}{2}\cdot\frac{1}{\mathrm{Re}}\cdot\frac{-A^{n+1}_{i+\frac{5}{2}j} + 16\cdot A^{n+1}_{i+\frac{3}{2}j}}{12\Delta x_1^2} +$$

$$+\frac{-30\cdot A^{n+1}_{i+\frac{1}{2}j} + 16\cdot A^{n+1}_{i-\frac{1}{2}j} - A^{n+1}_{i-\frac{3}{2}j}}{12\Delta x_1^2} = d_{i+\frac{1}{2}j}$$

$$\begin{gathered} s_1\cdot A^{n+1}_{i+\frac{5}{2}j} - 16\cdot s_1\cdot A^{n+1}_{i+\frac{3}{2}j} + \left(1+30\cdot s_1\right)\cdot A^{n+1}_{i+\frac{1}{2}j} - \\ -16\cdot s_1\cdot A^{n+1}_{i-\frac{1}{2}j} + s_1\cdot A^{n+1}_{i-\frac{3}{2}j} = d_{i+\frac{1}{2}j} \end{gathered} \qquad (23)$$

where $s_1 = \dfrac{\tau}{24\cdot\mathrm{Re}\cdot\Delta x_1^2}$

This equation (23) is solved by five-point sweep method, the result of which $A^{n+1}_{i+\frac{1}{2}jk}$ is defined.

At the second stage $q_{i+\frac{1}{2}jk}$ is sought in the direction of the x_2 coordinates:

$$\left[1-\frac{\tau}{2}\cdot\frac{1}{\mathrm{Re}}\cdot\frac{\partial^2}{\partial x_2^2}\right]q_{i+\frac{1}{2}j} = A_{i+\frac{1}{2}j}$$

$$q^{n+1}_{i+\frac{1}{2}j} - \frac{\tau}{2}\cdot\frac{1}{\mathrm{Re}}\cdot\left(\frac{\partial^2 q}{\partial x_2^2}\right)^{n+1}_{i+\frac{1}{2}j} = A^{n+1}_{i+\frac{1}{2}j}$$

$$q^{n+1}_{i+\frac{1}{2}j} - \frac{\tau}{2}\cdot\frac{1}{\mathrm{Re}}\cdot\frac{-q^{n+1}_{i+\frac{1}{2}j+2} + 16\cdot q^{n+1}_{i+\frac{1}{2}j+1}}{12\Delta x_2^2} +$$

$$+\frac{-30\cdot q^{n+1}_{i+\frac{1}{2}j} + 16\cdot q^{n+1}_{i+\frac{1}{2}j-1} - q^{n+1}_{i+\frac{1}{2}j-2}}{12\Delta x_2^2} = A^{n+1}_{i+\frac{1}{2}j}$$

$$s_2\cdot q^{n+1}_{i+\frac{1}{2}j+2} - 16\cdot s_2\cdot q^{n+1}_{i+\frac{1}{2}j+1} + \left(1+30\cdot s_2\right)\cdot q^{n+1}_{i+\frac{1}{2}j} -$$

$$-16\cdot s_2\cdot q^{n+1}_{i+\frac{1}{2}j-1} + s_2\cdot q^{n+1}_{i+\frac{1}{2}j-2} = A^{n+1}_{i+\frac{1}{2}j}$$

where $s_2 = \dfrac{\tau}{24\cdot\mathrm{Re}\cdot\Delta x_2^2}$

This equation (24) is solved by a three-point sweep, as a result of which is $q^{n+1}_{i+\frac{1}{2}j}$ is obtained.

After the value determination of $q^{n+1}_{i+\frac{1}{2}j}$, the $\hat{u}_1{}^{n+1}_{i+\frac{1}{2}j}$ is defined in following way

$$\hat{u}_1{}^{n+1}_{i+\frac{1}{2}j} = q_{i+\frac{1}{2}j} + u_1{}^{n}_{i+\frac{1}{2}j}$$

Components of the velocity $\hat{u}_2{}^{n+1}_{ij+\frac{1}{2}}$ is obtained in the similar way.

Results of numerical simulation

The numerical simulation the following values were determined: oil film thickness of occurrence, the dynamics of oil spreading, depending on time and the diameter of the spreading oil slick.

In this problem the spreading of the pollutant is consideredat the domain L = 100 m, H = 50 m. The number of points on the x-axis is equal to 256, in y – 128. Figures 2 – 5 shows a multi-phase environment where green is colored region of the air flow over the sea-"gas", where the density and dynamic viscosity equal ρ_{gas} = 1.27 kg/m^3; μ_{gas} = 1.7 × 10^{-5} Pa·sec respectively, is shown in blue with $\rho_{pollu\ tant}$ = 900 kg/m^3 density of pollutant, having the physical properties of the viscous fluid $\mu_{pollu\ tant}$ = 0.1 × 10^{-2} Pa·sec, and the region is colored red respectively is sea water – "water", where; ρ_{water} = 1020 kg/m^3; μ_{water} = 0.9 × 10^{-3} Pa·sec.

Comparison of results of test problem and experimental task on the basis of the model

In this problem, we consider the process of collapse of the dam Figure 6, the domain size are 1.25x0.7 m. Computational domain size number of dots in the x equals 142, y-axis - 80. The sides of the rectangle are solid walls, in which is placed slip condition. Figure 7 shows the dynamics of fluid distribution.The calculation of the present work in comparison with the calculation of work Minakov [9] and experimental data by Martin [10]. The initial height of the liquid column are 0:4 m.

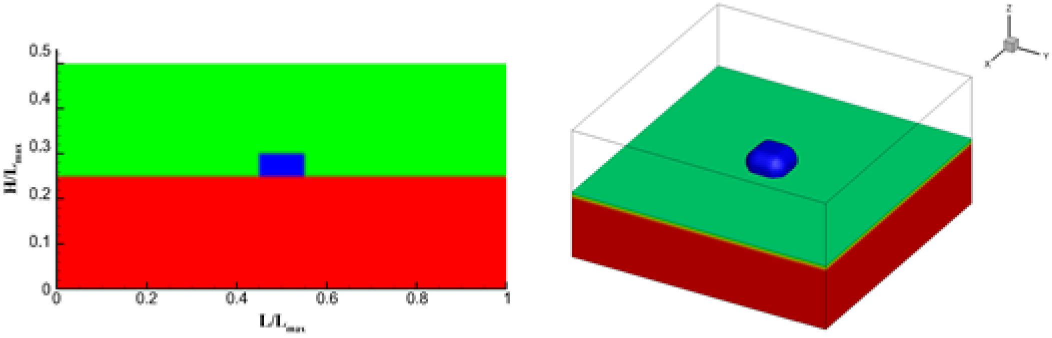

Figure 2 – The dynamics of the spreading of the pollutant on the surface of the sea at t=0 sec.

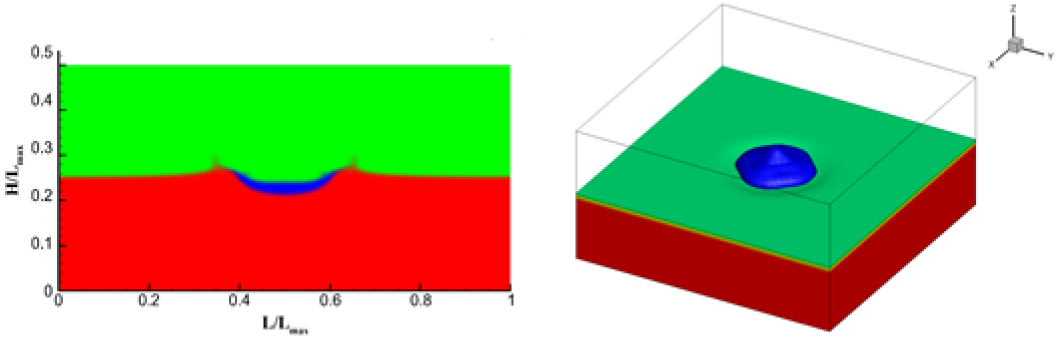

Figure 3 – The dynamics of the spreading of the pollutant on the surface of the sea at t=2 sec.

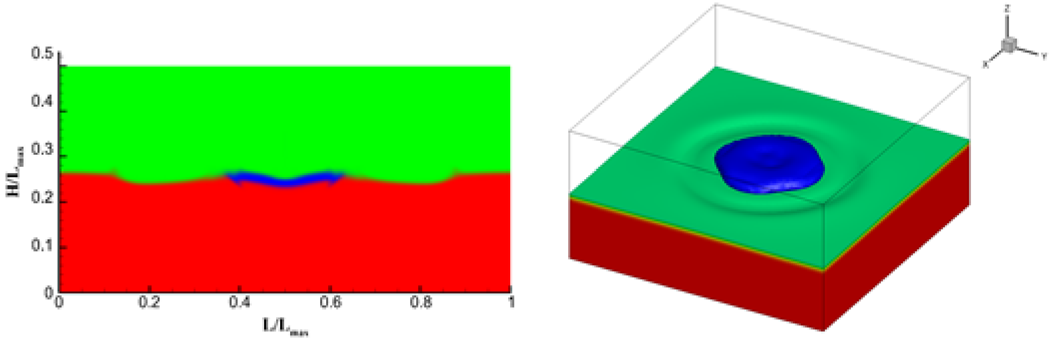

Figure 4 – The dynamics of the spreading of the pollutant on the surface of the sea at t=6 sec.

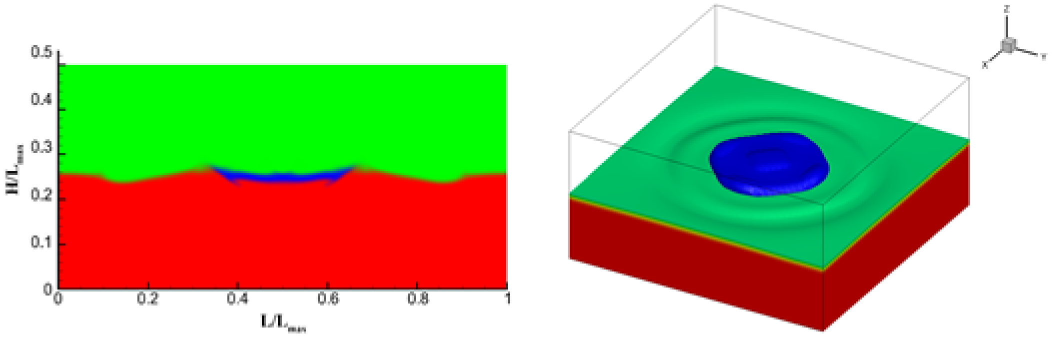

Figure 5 – The dynamics of the spreading of the pollutant on the surface of the sea at t=7sec.

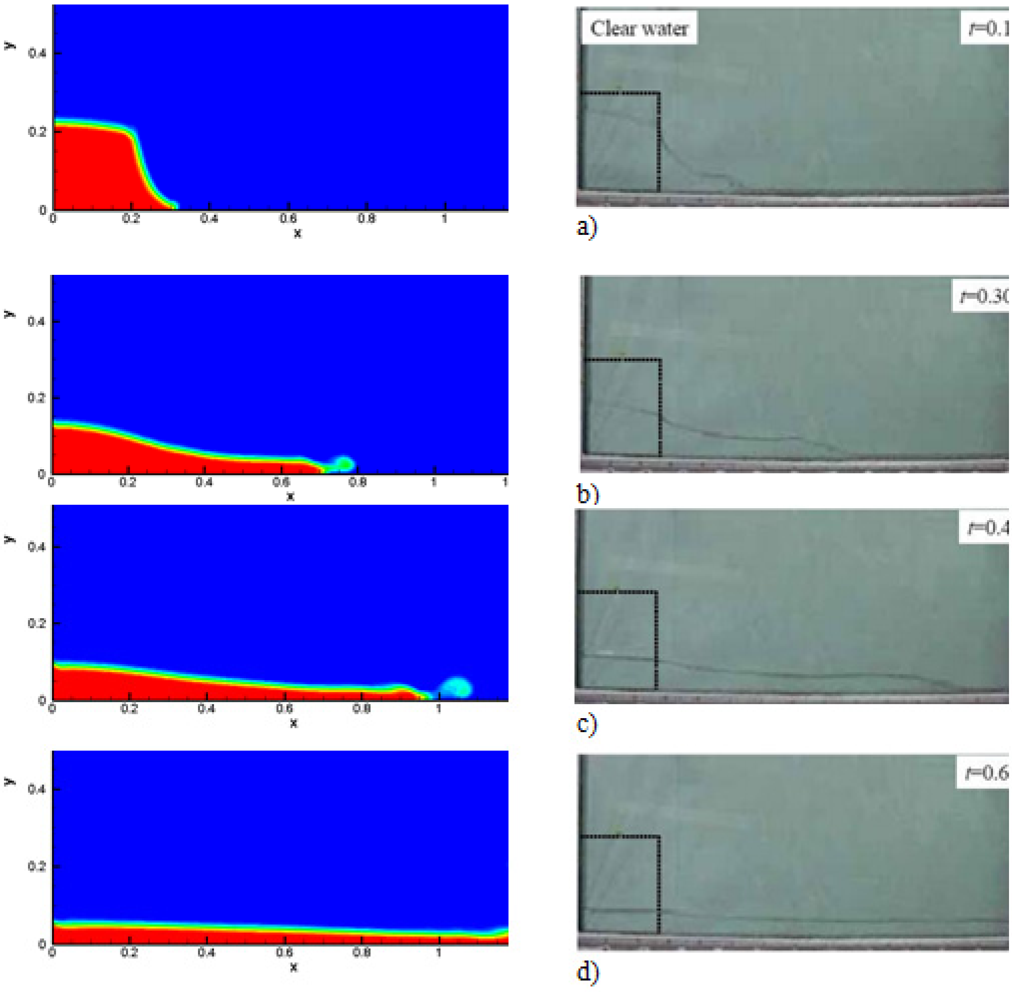

Figure 6 – Distribution of the volume fraction of water in different times
(numerical results on the left, to the right of the experimental results of Sassa and Sekiguchi [8]):
a) t=0.15 sec; b) t=0.3 sec; c) t=0.45 sec; d) t=0.6 sec.

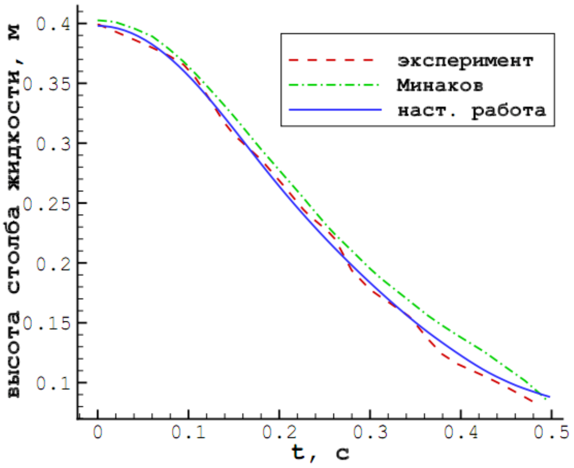

Figure 7 – the height of the liquid column near the left wall depending on time.

Conclusion

Drawing an analysis of the results it can be concluded, that the developed model of the spreading of an oil slick on the seawater surface allowing the researchers, who are involved in the evaluation of environmental damage, to determine the trajectory of the migration of an oil slick on the Caspian Sea and to obtain the most objective result of a process of spreading of oil and oil products.

The numerical simulation of oil spills in the open sea under different scenarios, including the different initial mass of spilled oil, the various types of produced and transported oil through the Caspian sea is carried out.

The work is supported by grant funding research programs and projects of the Ministry of education and Sciences, grant No. 1905/GF-4 "Development of software complex for assessment of the anthropogenic pollution from industrial regions of Kazakhstan by methods of mathematical modeling".

References

1. Kachurin, N.M. Levkin, N.D., Commissars, M.S. // Geoecological problems of coal mining regions: monograph. Tula: Izd. Tulgu, 2011. – 560 p.

2. Kilanova, N.In. Klimova, E.G., Zudin, A.N. Estimation of concentration and emissions from a passive gas on the basis of absorption data for a region of Siberia // Intern. Conf. by measuring, modeling and information systems for the study of the environment (Enviromis-2012): Selected works. – Irkutsk, 2012. – P. 185-187.

3. Potapov, V.P., Giniyatullina, O.L., Andreeva, N.In. Information-mathematical model of environmental pollution in coal-producing regions // Innovation Convention "Kuzbass: education, science, innovations". Vol. 2. – 2012. – P. 159-162.

4. Canepa, E., D'Alberti, F., D'Amati, F., Triacchini, G. The GIS-based SafeAirView software for the concentration assessment of radioactive pollutants after an accidental release // Science of the total environment, 2007. – Vol. 373, No 1. – P. 32-42.

5. Integrated water resources management: mathematical models and information technology / Preprint ed. by L.A. Rukhovets. SPb EMI RAS, 2007. – 65 p.

6. Abdibekov U.S., Poems, A.K., Zhakebaev, D.B., Karuna O.L. the Modeling of transfer process and evaporation of the oil film from the surface of the sea // Oil and gas, 2014. – Vol. 83, No 5. – P. 23-27.

7. Zhumagulov B.T., Zhakebayev D.B., Abdibekova A.U. The decay of MHD turbulence depending on the conducting properties of environment // Magnetohydrodynamics, 2014. – Vol. 50, No. 2. – P. 121-138.

8. Sassa S., Sekiguchi H. et al. Modelling of sediment gravity flows with progressive solidification // Kyoto Daigaku Bōsai Kenkyūjonenpō. 2005. – Vol. 48. – P. 757-774.

9. Minakov A. Numerical simulation of viscous incompressible fluid flows with moving boundaries. 2008.

10. Martin J., Moyce W. Part IV. An experimental study of the collapse of liquid columns on a rigid horizontal plane // Philosophical Transactions of the Royal Society of London A: Mathematical, Physical and Engineering Sciences. 1952. –Vol. 244, No882. – P.312-324.

UDC 532;517.4;519.6

*Issakhov A., Alpar S., Zhazylbekov N.

Faculty of Mechanics and Mathematics,
al-Farabi Kazakh National University, Almaty, Kazakhstan
*e-mail: alibek.issakhov@gmail.com

Numerical modeling of elliptic equations on unstructured and hybrid grids

Abstract. In reality, most of the physical processes are described by partial differential equations. At the same time, many application problems require numerical simulations in areas with complex geometry. Description of computational areas with complex geometric shape is best performed on unstructured and hybrid grids. An important advantage of unstructured or hybrid grid is simplicity of generation. For this purpose a large preference was given for methods that can be applied on unstructured and hybrid grids. This method is a finite volume method. One of the advantages of this discretization method is performing of local and global conservation laws, and this is very important in solving many applied problems. In the present work the variety of grids with their advantages and disadvantages are described, also the final volume method and choice of the shape of final volume are considered, discretization of the two and three dimensional Poisson equation by finite volume method is made on the unstructured and hybrid grid, formulas of finding areas, volumes and normal are described and displayed. The aim of this work is the further application of the finite volume method, and obtaining approximation of the Poisson equation in two-dimensional and three-dimensional cases on unstructured and hybrid grid. Finally, numerical results for unstructured and hybrid grids, as well as the data that obtained are compared with the analytical results, which shows good agreement. The numerical values are illustrated in the work in the form of plots.

Key words: two and three dimensional Poisson equation, unstructured mesh, hybrid mesh, finite volume method, Jacobi method.

Introduction

When we solve the fluid dynamics applications tasks one of the main problems is the computational domain. Various types of computational grids are used to describe the computational domain. Two main classes can be identified among the types of computational grids:

1. Structured mesh (regular grid).
2. Unstructured mesh (irregular grid).

Structured mesh, that shown in the Figure 1, are widely used in the field of computational fluid dynamics. When you create a regular grid, the grid nodes are an ordered structure, that have clearly defined grid direction. The main advantage of using a structured mesh is to maintain the canonical structure of the neighbors to mesh nodes. In the case of two-dimensional computational grid, cells are rectangles, and in three-dimensional case – hexagons. This type of mesh has two forms: grids with fixed (constant) step and meshes with a variable step, and the step may be constant for one of the axes and variable on other. Regular mesh allows you to use different discretization methods, in particular the finite difference method and finite volume method.Usually when you create regular grids in complex geometric areas, you need to use the coordinate transformation to build a uniform computational grid, as well as you have to write its mathematical model in curvilinear coordinates.

The main feature of unstructured grids, that shown in Figure 2, is a chaotic arrangement of mesh points in the computational domain, and as a consequence there are no areas of the grids' directions and it is impossible to arrange mesh nodes. In the three dimensional case the grid cells are used by polyhedrons and in the two dimensional case polygons with any shape. Generally, in the two dimensional case we use triangles, in the three dimensional case - tetrahedrons. The use of more complex geometric shapes is irrational in the process of meshing. Irregular mesh allows you to use different discretization methods, such as finite volume method and finite element method.

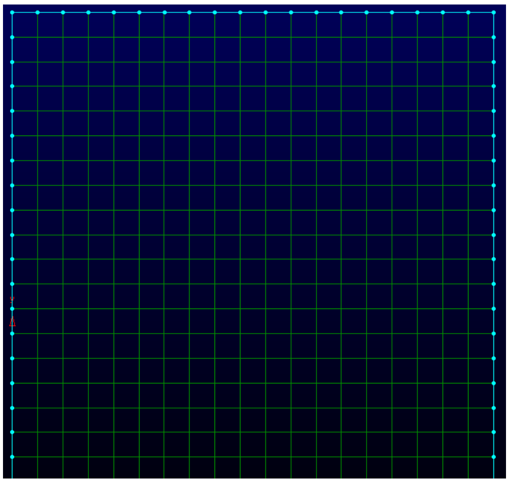

Figure 1 – Structured mesh

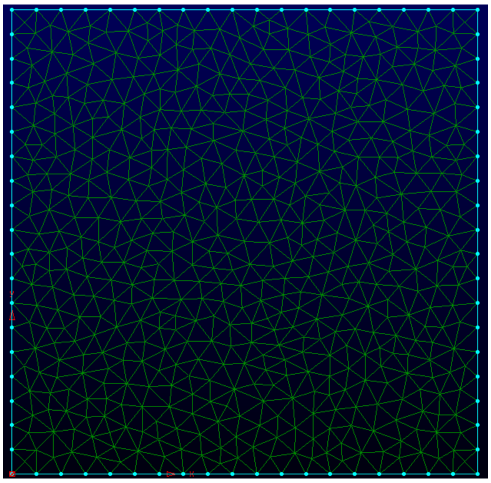

Figure 2 – Unstructured mesh

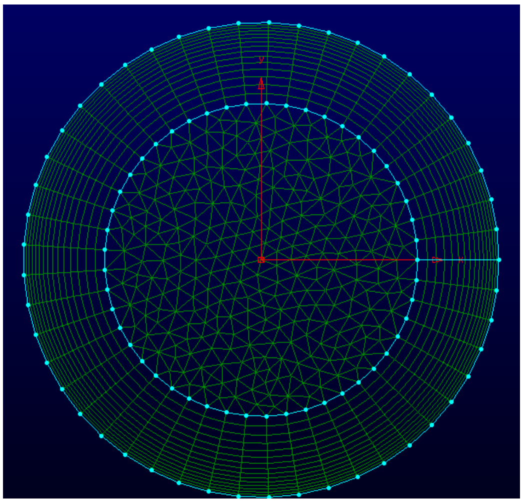

Figure 3 – Hybrid mesh

There are many ways of triangulation of calculation domain through the given points, but with any methods of triangulation we get the same number of triangles. Triangulation of the computational domain is produced according to certain criteria. One of the criterions of triangulation sounds like that – triangles, which are obtained, should be more like equilateral triangles, in other word the angles must not be too sharp. Another criterion of triangulation is triangles, that we created, shouldn't be much different in size from the neighboring triangles (mesh uniformity criterion).

The main disadvantage is the lack of data about irregular mesh structure, which leads to high costs of computing resources (computational memory). The positive features of unstructured grids are:

a) the application of this computational grids to a large number of applicable tasks;

b) minimum time in the construction of unstructured mesh as opposed to regular grids for complex geometries;

c) implementation of thickening mesh in certain areas of computational mesh by natural way.

The combination of structured and unstructured grids forms a so-called hybrid mesh (Figure 3), which allows you to take advantage from certain nets and reduce the disadvantages of a particular type of nets. Hybrid mesh often used for solving applied problems of fluid mechanics and gas mechanics.

Mathematical model

For the two variants of problems numerical solutions are compared with analytical solutions. To verify the numerical algorithm on unstructured and hybrid meshes we used Poisson equation, which has an analytical solution. In this paper we consider two problems. In the first problem we considered a two-dimensional Poisson equation, which was solved on unstructured grids. In the second problem we considered a three-dimensional Poisson equation, which was solved on unstructured and hybrid computing meshes.

The first problem (two-dimensional equation):

$$\frac{\partial^2 u}{\partial x^2}+\frac{\partial^2 u}{\partial y^2}+3u=$$
$$=-2\sin(x+2y)+16e^{2x+3y}$$

$$u\big|_{x=0}=\sin(x+2y)+e^{2x+3y}$$
$$u\big|_{x=0.25}=\sin(x+2y)+e^{2x+3y}$$
$$u\big|_{y=0.5}=\sin(x+2y)+e^{2x+3y}$$
$$\left.\frac{\partial u}{\partial y}\right|_{y=0}=2\cos(x+2y)+3e^{2x+3y}$$

This equation has an analytic solution of this type:

$$u=\sin(x+2y)+e^{2x+3y}$$

The second problem (three-dimensional equation):

$$\frac{\partial^2 u}{\partial x^2}+\frac{\partial^2 u}{\partial y^2}+\frac{\partial^2 u}{\partial z^2}+10u=$$
$$=-4\cos(3x+y-2z)+12e^{x-z}+10$$

$$u\big|_{x=0}=\cos(3x+y-2z)+e^{x-z}+1$$
$$u\big|_{x=0.25}=\cos(3x+y-2z)+e^{x-z}+1$$
$$u\big|_{y=0}=\cos(3x+y-2z)+e^{x-z}+1$$
$$u\big|_{y=0.5}=\cos(3x+y-2z)+e^{x-z}+1$$
$$u\big|_{z=0}=\cos(3x+y-2z)+e^{x-z}+1$$
$$\left.\frac{\partial u}{\partial z}\right|_{z=0.5}=2\sin(3x+y-2z)-e^{x-z}$$

This equation has an analytic solution of this type:

$$u=\cos(3x+y-2z)+e^{(x-z)}+1$$

Approximation of the equations

Poisson's equation was approximated by using the control volume method and it was solved numerically by Jacobi method. For the application of the approximation by method of control volume we used Gauss's theorem with further replacement of the surface integral to a finite sum, that has the form:

$$\int_{V_0}\nabla\cdot(k\nabla\phi)dV=\int_{S}k\nabla\phi\cdot\bar{n}\,dA$$

Since the number of faces is limited, we can replace the surface integral sum with:

$$\int_{S}k\nabla\phi\cdot\bar{n}\,dA\approx\sum_{f}k_f\left(\nabla\phi\right)_f\cdot\bar{n}_f A_f=S_{\phi,0}V_0$$

The next task is to express $\left(\nabla\phi\right)_f\cdot\bar{n}_f$ through the values of the center of the cell. For this we consider the operator Nabla.

$$\nabla\phi=\left(\frac{\partial\phi}{\partial x}\bar{i}+\frac{\partial\phi}{\partial y}\bar{j}+\frac{\partial\phi}{\partial z}\bar{k}\right)$$

The above Nabla operator can be written by another basis vectors. That is for the unit normal vector, two unit tangent and to the normal vector that perpendicular to the plane.

$$\nabla\phi=\left(\frac{\partial\phi}{\partial n}\bar{n}+\frac{\partial\phi}{\partial t_1}\bar{t}_1+\frac{\partial\phi}{\partial t_2}\bar{t}_2\right)$$

Similarly, for the new base:

$$\nabla\phi=\left[\left(\nabla\phi\right)\cdot\bar{n}\right]\bar{n}+\left[\left(\nabla\phi\right)\cdot\bar{t}_1\right]\bar{t}_1+\left[\left(\nabla\phi\right)\cdot\bar{t}_2\right]\bar{t}_2$$

The two-dimensional case on the unstructured grid (Figure 4).

$$\nabla\phi=\left[\left(\nabla\phi\right)\cdot\bar{n}_f\right]\bar{n}_f+\left[\left(\nabla\phi\right)\cdot\bar{t}_f\right]\bar{t}_f$$

Lets consider the vector $\bar{l}$, that connects the two centers of the neighboring cells. Then lets perform scalar multiplication of vector $\bar{l}$ with Nabla operator.

$$(\nabla\phi)_f\cdot\bar{l} = [(\nabla\phi)_f\cdot\bar{n}_f]\delta_f + [(\nabla\phi)_f\cdot\bar{t}_f]\bar{t}_f\cdot\bar{l}$$

For approximation of $(\nabla\phi)_f\cdot\bar{l}$ to the cell centers, lets expand it in a Taylor series,and with the non-trivial action we get:

$$(\nabla\varphi)_f\cdot\bar{n}_f = \frac{\varphi_1-\varphi_0}{\delta_f} - \frac{[(\nabla\varphi)_f\cdot\bar{t}_f]\bar{t}_f\cdot\bar{l}}{\delta_f}$$

$$J_f = [(\nabla\varphi)_f\cdot\bar{t}_f]\bar{t}\cdot\bar{l}$$

Letsconsiderseparately J_f.

$$(\nabla\phi)_f\cdot\bar{t}_f = \frac{\phi_a-\phi_b}{|\bar{t}_f|}$$

$$J_{f=}\left(\frac{\phi_a-\phi_b}{|\bar{t}_f|}\right)\bar{t}_f\cdot\bar{l}_f$$

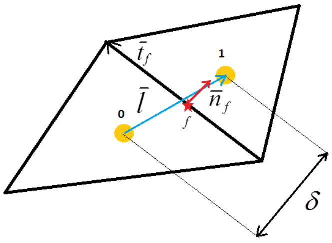

Figure 4 – Two adjacent cells of unstructured mesh

Eventually the approximation of the two-dimensional case can be written like following formula:

$$\sum_f k_f(\nabla\phi)_f\cdot\bar{n}_f A_f = \sum_f k_f\left(\frac{\phi_1-\phi_0}{\delta_f} - \left[\frac{\phi_a-\phi_b}{\delta_f|\bar{t}_f|}\right]\bar{t}_f\cdot\bar{l}_f\right)A_f = S_{\phi,0}V_0$$

And for the three-dimensional case lets go back to the main final volume equation.

$$\sum_f k_f(\nabla\phi)_f\cdot\bar{n}_f A_f = S_{\phi,0}V_0$$

We take Nabla operator for normal and for his two orthogonal tangent vectors.

$$\nabla\phi = [(\nabla\phi)\cdot\bar{n}]\bar{n} + [(\nabla\phi)\cdot\bar{t}_1]\bar{t}_1 + [(\nabla\phi)\cdot\bar{t}_2]\bar{t}_2$$

Consider a gradient, that is shown below.

$$(\nabla\varphi)_f\cdot\bar{l} = [(\nabla\varphi)_f\cdot\bar{n}_f]\bar{n}_f\cdot\bar{l} + \\ +\{[\bar{n}_f\times(\nabla\varphi)_f]\times\bar{n}_f\}\cdot\bar{l}$$

As well as the two-dimensional case $(\nabla\phi)_f\cdot\bar{l}\approx\phi_1-\phi_0$ and $\delta=\bar{n}\cdot\bar{l}$

$$(\nabla\varphi)_f\cdot\bar{n}_f = \frac{\varphi_1-\varphi_0}{\delta} - \\ -\frac{\{[\bar{n}_f\times(\nabla\varphi)_f]\times\bar{n}_f\}\cdot\bar{l}}{\delta} = \frac{\varphi_1-\varphi_0}{\delta} - \frac{J_T}{\delta}$$

where J_T – tangential flow. Let us consider now a triangular face (Figure 6), in which we try to extract J_T.

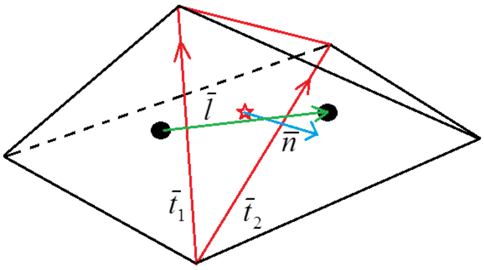

Figure 5 – Two neighboring tetrahedron

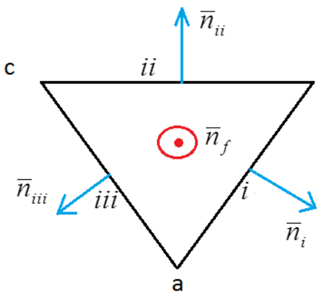

Figure 6 - The face of a tetrahedron

$$(\nabla \phi)_f = \frac{1}{A_f} \sum_{e=1}^{3} \overline{n}_e \phi_e L_e$$

Substitute it in tangential flow equation:

$$J_T = \left\{ \left[\overline{n}_f \times \frac{1}{A_f} \sum_{e=1}^{3} \overline{n}_e \varphi_e L_e \right] \times \overline{n}_f \right\} \cdot \overline{l} =$$

$$= \left\{ \left[\frac{1}{A_f} \sum_{e=1}^{3} \left[\left(\overline{n}_f \times \overline{n}_e \right) \times \overline{n}_f \right] \varphi_e L_e \right] \right\} \cdot \overline{l}$$

Let us use the properties of the mixed multiplication of vectors:

$$\left(\overline{b} \times \overline{c} \right) \times \overline{d} = \left(\overline{d} \cdot \overline{b} \right) \cdot \overline{c} - \left(\overline{d} \cdot \overline{c} \right) \cdot \overline{b}$$

Consequently:

$$J_T = \left\{ \left[\frac{1}{A_f} \sum_{e=1}^{3} \left[\left(\overline{n}_f \cdot \overline{n}_f \right) \overline{n}_e - \left(\overline{n}_f \cdot \overline{n}_e \right) \overline{n}_f \right] \varphi_e L_e \right] \right\} \cdot \overline{l} =$$

$$= \left\{ \left[\frac{1}{A_f} \sum_{e=1}^{3} \overline{n}_e \varphi_e L_e \right] \right\} \cdot \overline{l}$$

One of the problems when we calculate J_T is the normal $(\overline{n}_e)$ to the side of faces of the finite volume element.

$$\overline{n}_e = \overline{t}_e \times \overline{n}_f$$

Substitute $\overline{n}_e$ in J_T, weget:

$$J_T = \frac{1}{A_f} \sum_{e=1}^{3} \phi_e \left(\left[L_e \overline{t}_e \times \overline{n}_f \right] \cdot \overline{l} \right)$$

When we multiply the length of the side L_e to the unit vector $\overline{t}_e$ that will become equal to the vector $\overline{T}_e$, which describes the whole side faces.

$$\overline{T}_e = L_e \overline{t}_e$$

Then we use properties of the mixed multiplication of vectors and apply it for the above mentioned equation.

$$J_T = \frac{1}{A_f} \sum_{e=1}^{3} \phi_e \left(\overline{T}_e \cdot \left[\overline{n}_f \times \overline{l} \right] \right)$$

Returning to the expression $(\nabla \varphi)_f \cdot \overline{n}_f$ lets substitute, that we found in J_T:

$$(\nabla \phi)_f \cdot \overline{n}_f = \frac{\phi_1 - \phi_0}{\delta} - \frac{1}{\delta A_f} \left(\sum_{e=1}^{3} \phi_e T_e \right) \cdot \left[\overline{n}_f \times \overline{l} \right]$$

$$\sum_f k_f \left\{ \frac{\phi_{nb(f)} - \phi_0}{\delta_f} - \frac{1}{\delta_f A_f} \sum_{e=1}^{n_{e(f)}} \phi_e \left(\overline{T}_e \cdot \left[\overline{n}_f \times \overline{l}_f \right] \right) \right\} A_f = S_{\phi,0} V_0$$

During non-trivial transformations we obtain our final approximation of the Helmholtz equation for two-dimensional and three-dimensional case. The problem is solved iteratively by using the Jacobi method.

Final form of discrete Jacobi method by using unstructured mesh for two-dimensional Poisson equation will look like this equation:

$$u_i^{n+1} = \frac{\left(\sum_f \left(\frac{u_{i,nb(f)}^n}{\delta_{i,f}} - \left[\frac{u_{i,a(f)}^n - u_{i,b(f)}^n}{\delta_{i,f} \left| \overline{t}_{i,f} \right|} \right] \overline{t}_{i,f} \cdot \overline{l}_{i,f} \right) A_{i,f} \right)}{\left(\sum_f \frac{A_{i,f}}{\delta_{i,f}} - 3V_i \right)} -$$

$$- \frac{\left(-2\sin(x+2y) + 16e^{2x+3y} \right) V_i}{\left(\sum_f \frac{A_{i,f}}{\delta_{i,f}} - 3V_i \right)}$$

Final discrete form of Jacobi method by using unstructured mesh for two-dimensional Poisson equation will look like this:

$$u_i^{n+1} = \frac{\left(\sum_f \left(\frac{u_{i,nb(f)}^n}{\delta_{i,f}} - \frac{1}{\delta_{i,f} A_{i,f}} \left(\sum_{e=1}^{3} u_{i,f,e}^n \overline{t}_{i,f,e}\right) \cdot \left[\overline{n}_{i,f} \times \overline{l}_{i,f}\right]\right) A_{i,f}\right)}{\left(\sum_f \frac{A_{i,f}}{\delta_{i,f}} - 10V_i\right)} -$$

$$- \frac{\left(-4\cos(3x + y - 2z) + 12e^{x-z} + 10\right) V_i}{\left(\sum_f \frac{A_{i,f}}{\delta_{i,f}} - 10V_i\right)}$$

Results of numerical calculations

In the first problem for the two-dimensional Poisson equation physical area is used with the sizes Lx = 0.25 and Ly = 0.5, which is approximated by using triangles. The number of physical computing points 1471, number of cells 2764. As shown in Figure 7, computational grid is stressed at the point (0.25, 0.5), because in this area the Neumann boundary condition is used and to minimize the numerical errors we had to stress the computational grid at the given point. For the second problem for the three-dimensional Poisson equation physical area is used with the sizes Lx = 0.25, Ly = 0.5, Lz = 0.5, which is approximated by using tetrahedrons for the unstructured mesh. Number of nodes 4687, number of cells 23084. (Figure 8).

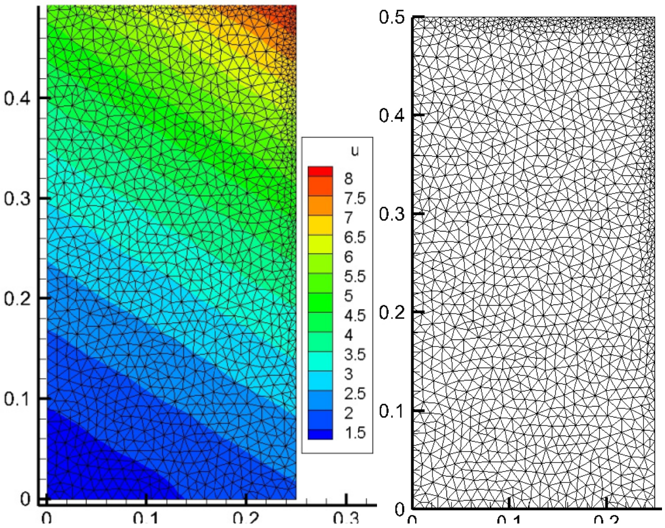

Figure 7 – A two-dimensional grid with numerical solution.
The maximum error is equal to 0.0654(0.7%).

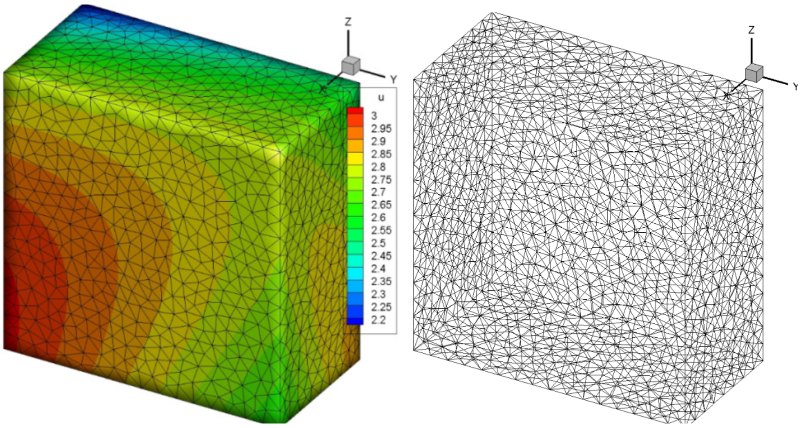

Figure 8 – Three-dimensional mesh with the numerical solution.
The maximum error is equal to 0.026(0.9%).

To reduce the numerical errors for unstructured meshes the hybrid mesh was used. For a hybrid three-dimensional problem the conditions of the second problem are used (three-dimensional Puassson equation). For this purpose computing region is divided into two blocks: unstructured and structured meshes, which will consist of tetrahedrons, hexagons and pyramids. Number of points 1812, number of cells 4380. Grid stressed along Z axis to the face, where the Neumann boundary condition is defined (fig.9). The following figures show benefits of unstructured and hybrid meshes on objects with various shapes.

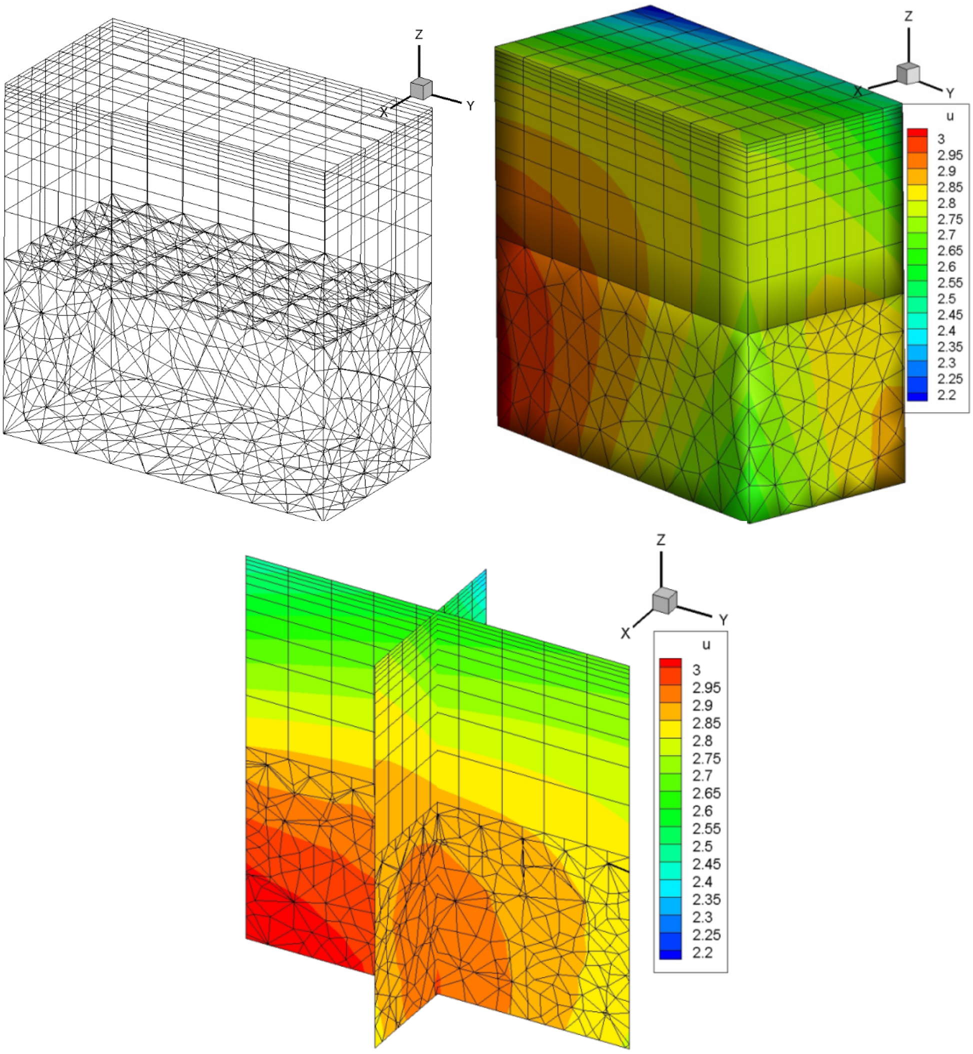

Figure 9 - The hybrid mesh with the numerical solution.
The maximum error is equal to 0.0114(0.4%).

Conclusion

During implementation of this work on the basis of numerical solution of two-dimensional and three-dimensional Poisson equations, test computations of finite volume method on unstructured grids were made. And also an analysis of solutions was performed for the three-dimensional Poisson equation using a hybrid mesh.

When we compared the results of numerical results of three-dimensional Poisson equation for unstructured and hybrid meshes, it may be noted that the numerical error is reduced when we use the hybrid mesh, and also computing resources used much less.

As a result of our investigation, according to the data that obtained, it can be said that the regular computational grid has the advantage in the accuracy of the solution, but by adapting unstructured computational mesh to complex geometry wa can create hybrid mesh, which will compensate the pros and cons of structured and unstructured grids..

In the paper it is shown that by using unstructured mesh numerical error equal 0.9%, and using a hybrid grid numerical error does not exceed 0.4%. From this we can conclude that it is necessary to use a structured grid in the area where it is possible and necessary to use unstructured grid where we can not use a structured grid.

References

1. Mazumder S. -Numerical methods for partial differential equation: Finite Difference and Finite Volume Methods. – Academic Press, 2015. – 484 p.

2. Versteeg H.K. Malalasek Introduction to computational fluid dynamics The finite volume method. – Pearson, 2007. – 520p.

3. F.Moukalled L.Mangani M.Darwish - The finite volume method in computational fluid dynamics. – Springer, 2015. –791p.

4. Fletcher K. Vychislitel'nye metody v dinamike zhidkostej. – Moscow: Mir, 1991. –Vol.2. – 552 p.

5. Chung T.J. Computational fluid dynamics. – Cambridge University Press, 2002. –1012 p.

6. Anderson D., Tannehil Dzh., Fletcher R. - Vychislitel'naja gidromehanika i teploobmen. Moskva, Mir, 1990. –Vol. 2. – 392 p.

7. Issakhov A., Mathematical modeling of the discharged heat water effect on the aquatic environment from thermal power plant // International Journal of Nonlinear Science and Numerical Simulation, – 2015. – Vol.16, No 5. – P. 229–238, doi:10.1515/ijnsns-2015-0047.

8. Issakhov A., Mathematical modeling of the discharged heat water effect on the aquatic environment from thermal power plant under various operational capacities // Applied Mathematical Modelling. – 2016. – Vol. 40, No 2. – P. 1082–1096

9. Issakhov A. Large eddy simulation of turbulent mixing by using 3D decomposition method // J. Phys.: Conf. Ser. – 2011. –Vol.318, No 4. –P. 1282-1288.

10. Ferziger J.H., M. Peric - Computational Methods for Fluid Dynamics. – Springer, 2013. – 440 p.

11. Firsov D.K. Metod kontrol'nogo ob'ema na nestrukturirovannoj setke v vychislitel'noj matematike. – Tomsk, 2007. – 72 p.

UDC 519.63; 519.684

*Issakhov A.A., Baitureyeva A.R.

Faculty of Mechanics and Mathematics,
al-Farabi Kazakh National University, Almaty, Kazakhstan
*e-mail: alibek.issakhov@gmail.com

Numerical simulation of wind flow around the architectural buildings

Abstract. Taking into account the high rate of construction in the modern big cities, it is very important to save the natural aerodynamics between the buildings. It is necessary to explore the ventilation of space between architectural structures, making a preliminary prediction before construction starting. The most optimal way of evaluating is to build a mathematical model of air flow. In this paper considered the aerodynamics between two high-rise buildings. A mathematical model of the wind flow around obstacles was carried out. In this paper were studied existing criteria about the distance between architectural objects and obtained graphics. There were considered elements of program realization of a numerical method and the cases of non-stationary two-dimensional flow calculation algorithms. The results of test calculations and plot are presented. This mathematical model allows to precisely calculate the optimal distance between the two buildings, which will take into account the climatic features, and will preserve the natural ventilation.

Key words: Navier-Stokes equation, large eddy simulation method, splitting method, aerodynamics.

Introduction

The high rate of construction in modern cities (including the Almaty) leads to the increasing of the architectural buildings amount. Due to the increase in population and in order to save space, mostly are currently constructed high-rise buildings. This leads to disruption of the natural aerodynamics of the city. Because of this, there is an increase of gas contamination of the city, the accumulation of heavy metals in the lower atmosphere and disruption of the local climate.

Building norms and rules now used in the construction and design of buildings, do not include the aerodynamic criteria and coefficients for indicating the optimum distance between buildings of different heights. The distance between buildings is considered to be the clear distance between the outer walls and other structures. The distances, which are specified between the objects while designing the buildings, can not ensure the free movement of wind vortex. This leads to disruption of the natural air flow.

Mathematical Model

The Navier-Stokes equations, obtained from the mass conservation law and Newton's second law, are the basis for the construction of mathematical model for wind flow around technogenic obstacles.

$$\nabla \cdot \vec{\upsilon} = 0$$

$$\frac{\partial \vec{\upsilon}}{\partial t} + \vec{\upsilon} \cdot \nabla \vec{\upsilon} = -\frac{1}{\rho} \nabla p + \nu \Delta \vec{\upsilon} \qquad (1)$$

Here $\vec{\upsilon}$ – the velocity vector, t – time, ρ – the density, p – the hydrodynamic pressure fluid, $\nu = \mu / \rho$ - molecular kinematical viscosity.

To minimize the number of calculations and experimental tests and to get the optimal flow pattern, it is necessary to convert all the parameters (flow rate, length, etc.) in the dimensionless parameters [1, 3-6]. The two streams are dynamically similar if dimensionless number, which determine flows, are equal.

Dimensionless variables are described as follows: [11-13]:

$$x_i^* = \frac{x_i}{L_0}, \quad t^* = \frac{\upsilon_0 t}{L_0},$$

$$\upsilon_i^* = \frac{\upsilon_i}{\upsilon_0}, \quad p^* = \frac{p - p_0}{\rho \upsilon_0^2},$$

Hence the equation of fluid motion and the continuity equation (1) in dimensionless form:

$$\frac{\partial \upsilon_i^*}{\partial t^*} + \upsilon_j^* \frac{\partial \upsilon_i^*}{\partial x_j^*} = \frac{1}{\mathrm{Re}} \frac{\partial^2 \upsilon_i^*}{\partial x_j^{*2}} - \frac{\partial p^*}{\partial x_i^*}$$

$$\frac{\partial \upsilon_i^*}{\partial x_i^*} = 0$$

Numerical Algorithm

Consider the Navier - Stokes equation in the form of integral conservation laws for an arbitrary fixed volume Ω with boundary $d\Omega$ [5, 10]:

$$\int_\Omega \left(\frac{\partial Q}{\partial t} \right) d\Omega + \oint_{\partial\Omega} (F_i + G_i) n_i \, d\Gamma = 0 \qquad (2)$$

Grid functions will be defined in the center of the cell and the values of flows across the border in divided cells. The volume of the cell is denoted by grid functions.

Now we perform discretization of the equation (2) by the control volume (CV) and the control surface (the CS)

$$\sum_{CV} \left(\frac{\Delta Q}{\Delta t} \right) \Delta\Omega + \sum_{CS} (F_i + G_i) n_i \Delta\Gamma = 0 \qquad (3)$$

A similar representation:

$$\sum_{CV} \Delta Q \Delta\Omega + \sum_{CS} \Delta t (F_i + G_i) n_i \Delta\Gamma = 0 \qquad (4)$$

For the numerical solution of equation (4) splitting scheme by physical parameters is used [2, 7-9, 12, 13]. At the first stage it is assumed that the transfer of momentum carried out only by convection and diffusion. The intermediate velocity field is found by 5-step Runge - Kutta method. At the second stage the pressure field is found based on the intermediate velocity field. Poisson equation for the pressure field is solved by Jacobi method. In a third step it is assumed that the transfer is carried out only by the pressure gradient.

I. $$\int_\Omega \frac{\vec{u}^{\,*} - \vec{u}^{\,n}}{\tau} d\Omega = -\oint_{\partial\Omega} (\nabla \vec{u}^{\,n} \vec{u}^{\,*} - \upsilon \Delta \vec{u}^{\,*}) n_i \, d\Gamma$$

II. $$\oint_{\partial\Omega} (\Delta p) d\Gamma = \int_\Omega \frac{\nabla \vec{u}^{\,*}}{\tau} d\Omega$$

III. $$\frac{\vec{u}^{\,n+1} - \vec{u}^{\,*}}{\tau} = -\nabla p.$$

Boundary Conditions

Two types of boundary conditions are used: Dirichlet and Neumann. For the pressure P on all borders except the output is used Neumann boundary condition. To the velocity components is used Dirichlet boundary condition. Here u_0 - the input velocity profile.

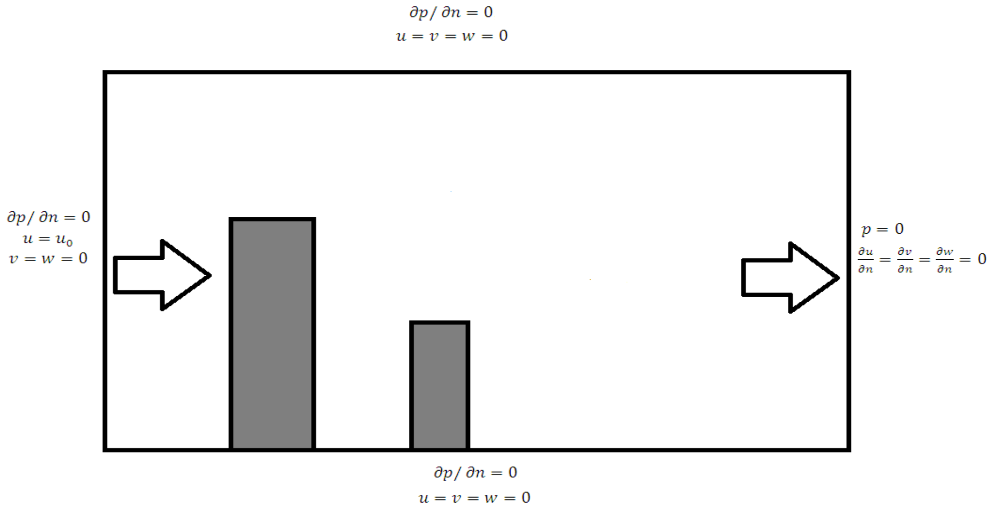

Figure 1 – Scheme of boundary and initial conditions.

Computational grid

Computational area was divided into 12 of subdomains of different sizes. Each subdomain is a grid unit, which contains a portion of a curved, irregular, unstructured grid. The number of grid points is selected in such way that oscillations wouldn't arise while solving the problem and the results would be correct at high Reynolds numbers. Thus, the computational grid contains over 100,000 control volumes. The mesh condensed between the buildings and near the streamlined surfaces of buildings. This allows to carry out more accurate calculation. Further away from the vortex zone, size control volumes increases.

Results

For the experiment, 9 floor (27 meters) and 5 floor (15 m) buildings have been considered as technogenic obstacles. Wind flow conditionally moves from high to low buildings. The following model examines “calm”, according to the Beaufort wind velocities scale. This wind velocity is in the range from 0 to 0.2 m/s. Various parameters were used to find the optimum distance. They are described in Building norms and rules of RK 3.01-01-2002 [14] and other normative documents. [15]

Figures 2 - 10 illustrate the results of wind flow around the technogenic obstacles for various distances between buildings (l = 20; 25; 31; 35 m) and for different wind speeds (= 0.1; 0.2 m / s).

According to the fire protection requirements, which are set out in the document [14], the minimum distance between the buildings of 4-floor height or higher must be not less than 20 meters. However, implementation of this model showed that at such distance a wind vortex didn't appeared between the buildings. Consequently, there is no air circulation in this diapason.

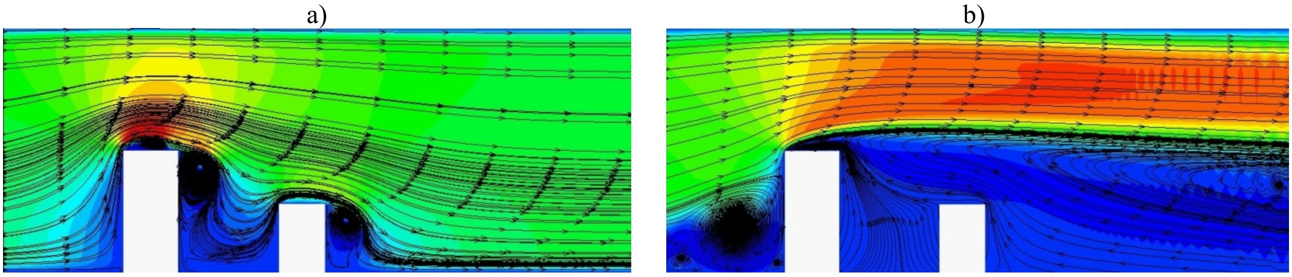
a) b)

Figure 2 - The horizontal velocity components of (v= 0.1 m/s) of flow around the technogenic obstacles with streamlines, which are calculated by using the DNS for the distance l = 20 (m) at different times (at t=0.001, t=2).

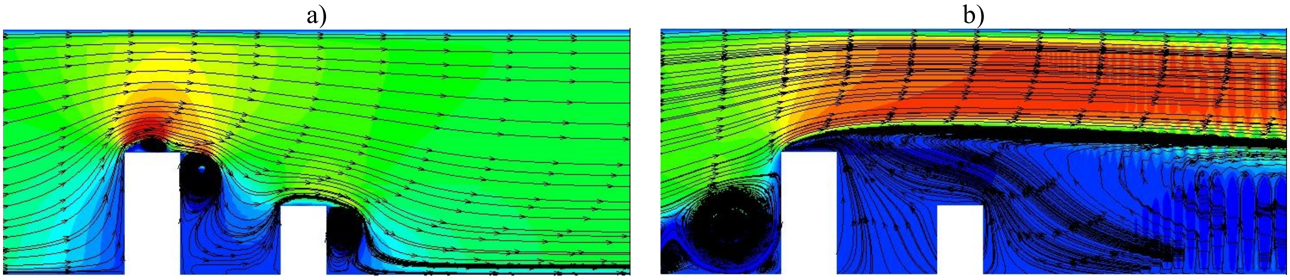
a) b)

Figure 3 - The horizontal velocity components of (v=0.2 m/s) of flow around the technogenic obstacles with streamlines, which are calculated by using the DNS for the distance l = 20 (m) at different times (at t=0.001, t=2).

In the following case the length of outbuildings (balconies, porch, etc.) has been added to the previous value and the distance of 25 m was obtained. The results showed that the vortex occurs at the initial moment, but over time it disappears, that is, wind circulation is intermittent.

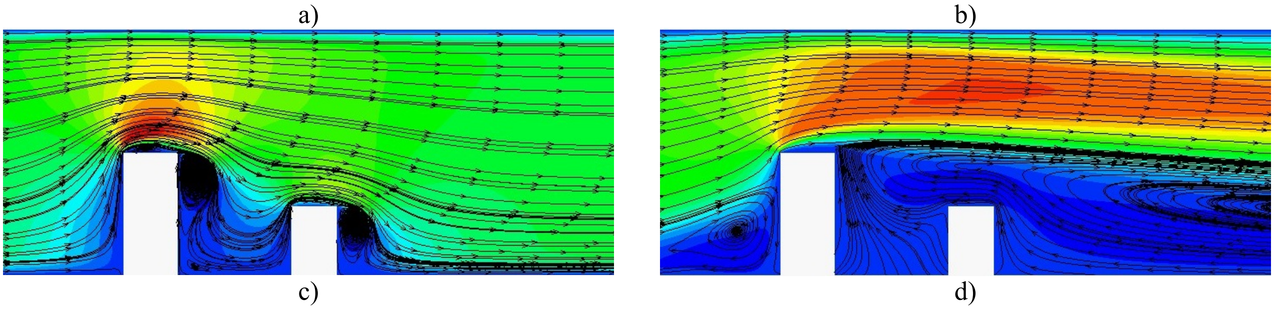

Figure 4 - The horizontal velocity components of (v=0.1 m/s) of flow around the technogenic obstacles with streamlines, which are calculated by using the DNS for the distance l = 25 (m) at different times (at t=0.001, t=2).

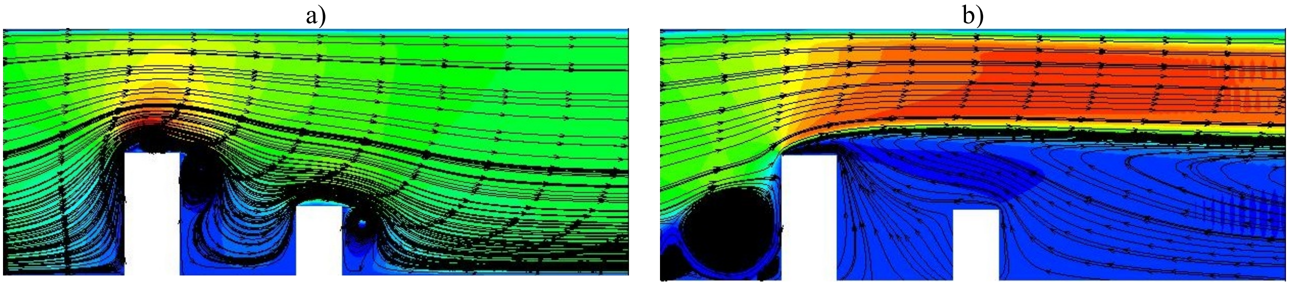

Figure 5 - The horizontal velocity components of (v=0.2 m/s) of flow around the technogenic obstacles with streamlines, which are calculated by using the DNS for the distance l = 25 (m) at different times (at t=0.001, t=2).

After that, the standard IBC (International Building Code), which is used in the United States, was considered. Here, the distance between the two buildings is calculated according to the following formula [15]:

$$\delta_{MT} = \sqrt{(\delta_{M1})^2 + (\delta_{M2})^2}$$

where δ_{MT} - the required distance, δ_{M1}, δ_{M2} - the height of the first and second buildings respectively.

The resulting distance between buildings was equal to 31 m, and satisfies all the standards specified in the national standards. The model also showed that the vortex at a given distance wouldn't arise.

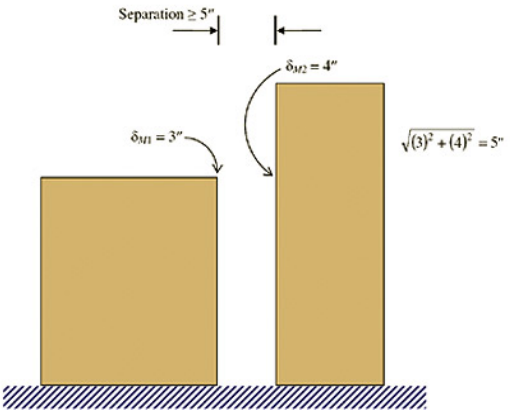

Figure 6 - The scheme of calculating the distance between the two high-rise buildings according to IBC 2009 1613.6.7 [15]

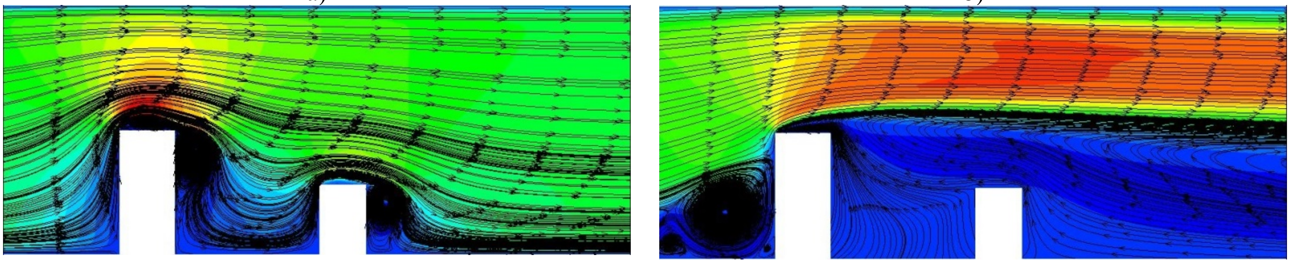
a) b)

Figure 7 – The horizontal velocity components of (ν=0.1 m/s) of flow around the technogenic obstacles with streamlines, which are calculated by using the DNS for the distance l = 31 (m) at different times (at t=0.001, t=2).

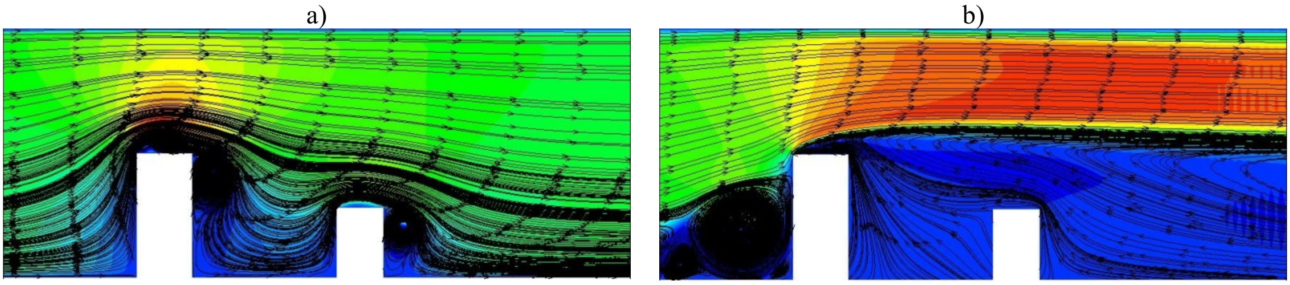
a) b)

c) d)

Figure 8 – The horizontal velocity components of (ν=0.2 m/s) of flow around the technogenic obstacles with streamlines, which are calculated by using the DNS for the distance l = 31 (m) at different times (at t=0.001, t=2).

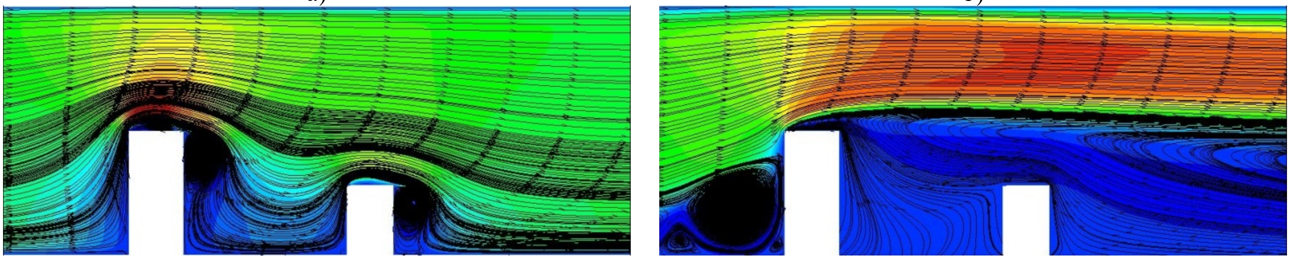
a) b)

Figure 9 – The horizontal velocity components of (ν=0.1 m/s) of flow around the technogenic obstacles with streamlines, which are calculated by using the DNS for the distance l = 35 (m) at different times (at t=0.001, t=2).

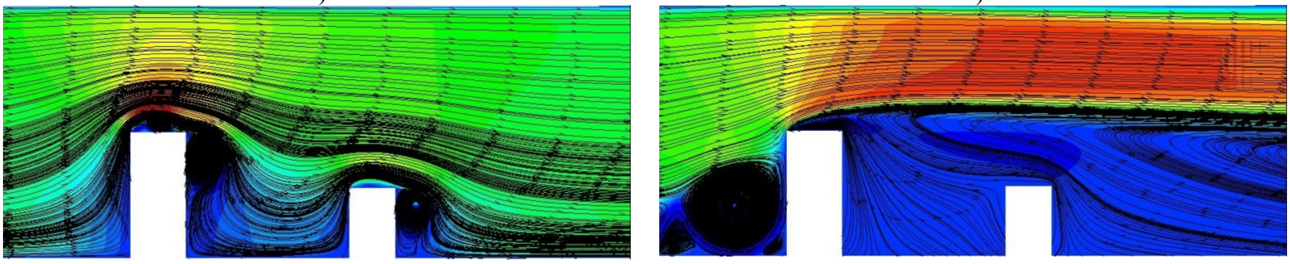
a) b)

Figure 10 – The horizontal velocity components of (ν=0.2 m/s) of flow around the technogenic obstacles with streamlines, which are calculated by using the DNS for the distance l = 35 (m) at different times (at t=0.001, t=0.5, t=1, t=2).

Here the length of outbuildings (balconies, porch, etc.) has been added to the previous value and obtained an approximate distance of 35 m. The model showed that the vortex produced between buildings, and therefore the natural aerodynamics between buildings is not broken.

Conclusion

In this paper, a mathematical model of wind flow around technogenic obstacles was built. It was based on full two-dimensional Navier - Stokes equations.

According to data, obtained as a result of the study, can be said, that the current standards and regulations for construction does not guarantee the necessary aerodynamics of the local areas. It should be noted that the advantages of this approach is the ability to create a model of wind flow around buildings as close as possible to reality. Thus, it is possible to assess in advance the optimality of the selected distance. This prevents the probability of choosing the wrong distance between close standing buildings, which will lead to a breach of natural circulation of air.

References

1. Anderson D., Tannehil Dzh., Pletcher R. Vychislitelnaya gidromehanika i teploobmen. M.: Mir. – 1990. – T. 1. – P. 337.
2. Belov I.A., Isaev S.A. Modelirovanie turbulentnyh techeniy: Uchebnoe posobie. // SPb: BGTU. – 2001. – P. 105.
3. Anderson J.D. Computational Fluid Dynamics. The Basics with Applications. – 1995. – P. 547.
4. Fletcher K. Vychislitelnye metody v dinamike zhidkostei. – Moskva: Mir. - 1991. – T.2. – P. 552.
5. Samarskiy A.A., Nikolaev E.S. Metody resheniya setochnyh uravneniy. – Moskva: Nauka, – 1978. – P. 592.
6. Rouch P. Vychislitelnaya gidrodinamika. – M.: Mi. – 1972. – P. 612.
7. Issakhov A. Large eddy simulation of turbulent mixing by using 3D decomposition method. // J. Phys.: Conf. Ser. – 2011. – Vol. 318. . – P. 042051.
8. Issakhov A.A. Pryamoe chislennoe modelirovanie (DNS) turbulentnyh techeniy s ispolzovaniem parallelnyh tehnologiy. Vestnik KazNU. – 2012. – № 2(73). – P .81-91.
9. Loicyanskiy L.G. Mehanika zhidkosti i gaza. // M.: GITTL. – 2003.
10. Chung T.J. Computational fluid dynamics. // CUP. – 2002.
11. Sedov L. I. Mehanika sploshnoi sredy.— M.: Nauka. – 1970. – T. 2. – P. 568.
12. Issakhov A. A., Abdibekov U.S., Zhumagulov B.T. Osnovy matematicheskogo i kompyuternogo modelirovaniya estestvenno-fizicheskih processov // "Qazaq universitety". – 2014. – P. 208.
13. Issakhov A.A. Matematicheskaya model teplovoi nagruzki na vodnuyu sredu pri razlichnyh ekspluatacionnyh moshchnostyah, Vestnik KazNU. – 2014. – Vol. 81. – No 2. – P.52-61.
14. SNiP RK 3.01-01-2002. 2.12* Gradostroitelstvo. Planirovka i zastroika gorodskih i selskih naselennyh punktov. P.7. Parametry zastroiki zhilyh i obshchestvenno-delovyh zon.
15. The International Building Code (IBC), Section 1613.6.7. – 2009.

UDC 519.63;.519.684

*Issakhov A.A., Mussakulova G.M.

Faculty of Mechanics and Mathematics,
al-Farabi Kazakh National University, Almaty, Kazakhstan
*e-mail: alibek.issakhov@gmail.com

Numerical simulation of the water flow in the case of an emergency at the protective hydraulic engineering constructions

Abstract. This paper presents numerical simulations of the water flow in the case of an emergency at the protective hydraulic engineering constructions. A mathematical modelfor simulation of water flow is based on Navier-Stokes equations derived from the conservation mass law and with phase equation. Numerical discretization of system of equations is done by finite volume method. System of water flow is solved by projection method. The phase and momentum equations are solved by Runge-Kutta method, and for the solution of Poisson equation the Jacobi method is applied. A program code was developed in C++ for numerical realization of water flow at emergency at the protective hydraulic engineering constructions.Numerical results are illustrated by figures.

Key words: Navier-Stokes equations, phase equation, mathematical model, hydraulic constructions, dam break.

Introduction

Dams are the structures designed to partition a watercourse or water for the lifting of the water level, in order to concentrate a water pressure at the site of construction and to createa reservoir. Typically, damsareparts of the hydroelectric complex, i.e., hydraulic structures, which are built in a particular location for the use of water resources for specific purposes: irrigation, hydropower, irrigation of pastures and so on.

The type and design of the dam are determined by its size, purpose, and the natural conditions and the main building material. Dams differ in type of the basic material from which they are erected, purpose and water passing conditions.

By the purpose of use dams are divided into storage reservoir and water level pumping types. Water pumping dams are built to improve the conditions of water intake from the river, the use of water power and so on. Therefore,affluent of the waterlevel of this type of dams is low. Storage dams differ markedly greater height, as a result, a large volume of the created reservoir. A distinctive feature of large storage dams is the ability to regulate the flow, small dams, by which, for example, ponds are created, don’t regulate the flow.

As an alternative to division of dams by theirs purposes acts division of dams by the height of water rise: low-pressure (depth of the water before the dam to 15 m), middle-pressure (15-50 m), high-pressure (over 50 m).

By the type of the material dams are divided into ground, tabby, metal, fabric, wood, iron-tabby, gabion types. By the way of perception of the main loads: gravity, arch, buttress, arch-gravity. By the conditions of the water flow passing: deaf, which do not allow overflow of the water through the crest spillway, filter, overflow.

Nowadays, potential catastrophic floods, resulting as an outcome of dam destructions, make great concern, since they bring big damage. The proof of this is seen in already occurred accidents. In 2010, a dam burst due to heavy rains took place on the Fuhe River in Jiangxi province in eastern China. One way or another, the disaster affected 29 million people. In the same year, there was a dam break on the Indus River in southern Pakistan. Over 895 thousand houses were destroyed, more than 2 million hectares of agricultural land were flooded. More than 1,700 people died. A year later, there was also a dam break, but this time, it took place on the Qiantang River near the city of Hangzhou in Zhejiang province in eastern China.Tidal wave of height up to 9 meters burst the dam and washed away a lot of people. Catastrophe at the dams, unfortunately, also took place in Kazakhstan too. On the 11th of March2010 due to a dam break in Kyzylagash several villages were flooded. 43 people died, 300 people were injured varying degrees of severity, and about 1,000 people were evacuated. Later the same year, there was another dam burst, but this time on the Usek River. 2187 inhabitants were evacuated. After 4 years a dam break took place in the village Kokpekty in the Karaganda region. As a result, five people died, 300 houses were flooded, 125 people were rescued, 300 were evacuated. And in 2015, as a result of a breakthrough the moraine lake Nameless, 40000 m^3 water was spewed. The mudflow came to the dam on the river Kargalinka. Three districts of the city were partially flooded, the Nauryzbaysky region was badly damaged.

As can be seen, dam accidents bring great damage, lead to the loss of human and financial resources. In order to minimize possibilities of such accidents a mathematical modeling is used, which allows to make small financial cost experiments, which results are very close to reality.

With the help of mathematical modeling, as well as the information about the area in which an artificial dam is planned to be built, an appropriate type of dam can be selected, the desired specifications of the dam, such as length, height and width of the walls, and so on, also can be selected. Mathematical modeling is also used in cases of accidents at the dams, to maximize the "softening" of aftermath. Selection of the most appropriate model and methods for simulating floods, caused by breakout, are very important steps. Also one should take into account to account that one-dimensional and two-dimensional models, compared tothree-dimensional model, have limitations, such as the failure of the first to embrace the spatial extent of the flood, from the standpoint of flow depth, velocity, time of arrival and flood recession, etc. These shortcomings are well studied in [1], which compares two-dimensional (Shallow water approach) and a full three-dimensional model. The latest model is composed by RANS equations, coupled with the method of volume of fluid. Comparisons of experimental and numerical data are also provided in the paper [1]. The results also show the superiority of the full three-dimensional model compared to the Shallow water approach.

Nowadays, as a result of development of technologies, parallel computation is also developed, which, as it is known, allows to spend less time for calculations. Thus, in [2], a mathematical model of a dam break problem is also provided and developed an improved method for correction of the pressure, in conjunction with the methods of volume of the liquid and the immersed boundary, to improve calculations of multiphase flow. TFQMR method is used to reduce the processing time in the solution of the Poisson equation.

In addition to the methods described in the papers mentioned above, there are also many other numerical methods for the dam break problems. So the method of integral boundaries are described in [3-5], method front track [6-8], the method of volume fluid [1, 2, 9, 10],the lattice Boltzmann method [11-13], the method the specified level [14-16], the phase-field methods [17-19].

Statement of the problem

The Navier-Stokes equations, derived from the law of conservation of mass, as well as the phase equation compose a mathematical model for the numerical simulation of water flow.

$$\nabla\vec{u} = 0$$

$$\frac{\partial\rho\vec{u}}{\partial t} + \nabla\cdot(\rho\vec{u}\vec{u}) - \nabla(\mu\nabla\vec{u}) = -\nabla p + \rho\vec{g} \qquad (1)$$

$$\phi_t + \vec{u}\nabla\phi = 0$$

where $\vec{u}$ – the velocity vector, t – time, p – the pressure, μ – the dynamic viscosity, ρ -the density.

Nondimensionalization of the system of equations (1) will be held as follows:

$$\vec{u}'=\frac{\vec{u}}{u},\ t'=\frac{t}{T},\ x'=\frac{x}{L},\ p'=\frac{p}{P},\ \vec{g}'=\frac{\vec{g}}{g},$$

$$\rho'=\frac{\rho}{\rho_\infty},\ \mu'=\frac{\mu}{\mu_\infty},\ \nabla'=\frac{1}{L}\nabla,\ \phi'=\frac{\phi}{\phi_\infty} \qquad (2)$$

By substituting dimensionless quantities (2) into the initial system of equations (1) and discarding the strokes,we get a mathematical model for the two-phase flow:

$$\nabla\vec{u}=0$$

$$\frac{\partial\vec{u}}{\partial t}+\vec{u}\cdot(\nabla\vec{u})=$$

$$=-\frac{1}{\rho}\nabla p+\frac{1}{\rho\,\mathrm{Re}}\nabla(\mu\nabla\vec{u})+\frac{1}{Fr^{2}}\vec{g} \qquad (3)$$

$$\phi_{t}+\vec{u}\nabla\phi=0$$

$$\rho=\phi\rho_{1}+(1-\phi)\rho_{2}$$

$$\mu=\phi\mu_{1}+(1-\phi)\mu$$

where μ – the dynamic viscosity, ρ – the density, μ_1 – the dynamic viscosity of the air, μ_2 – the dynamic viscosity of the water, ρ_1 – the density of the air, ρ_2 – the density of the water, $Fr^2=\frac{U^2}{gL}$ – the Froude number, $\mathrm{Re}=\frac{UL}{\nu}=\frac{UL\rho}{\mu}$ – the Reynolds number

Numerical algorithm

The splitting scheme of physical parameters is used for the numerical solution of the system (3) [20, 21]. In the first step, it is assumed that the transfer of momentum carried out only by convection and diffusion. The intermediate velocity field is computed using the Runge-Kutta method. In the second stage, the pressure field is calculated via the found intermediate velocity field. The Poisson equation for the pressure field is solved by the Jacobi method. In the third step, it is assumed that the transfer is carried out only by the pressure gradient. In the fourth phase, the phase equation is solved numerically by the Runge-Kutta method.

I. $\int_{\Omega}\frac{\vec{u}^{*}-\vec{u}^{n}}{\tau}d\Omega=-\oint_{\partial\Omega}(\nabla\vec{u}^{n}\vec{u}^{*}-\upsilon\Delta\vec{u}^{*})n_{i}d\Gamma$

II. $\oint_{\partial\Omega}(\Delta p)d\Gamma=\int_{\Omega}\frac{\nabla\vec{u}^{*}}{\tau}d\Omega$

III. $\frac{\vec{u}^{n+1}-\vec{u}^{*}}{\tau}=-\nabla p.$

IV. $\int_{\Omega}\frac{\phi^{n+1}-\phi^{n}}{\tau}d\Omega=-\oint_{\partial\Omega}(\vec{u}^{n}\nabla\phi^{n+1})n_{i}d\Gamma$

After all these four steps the density and the viscosity are calculated by formulas given the mathematical model.

Results of the numerical simulation

A domain with size of 3 to 1 is used for the numerical simulation of the two-dimensional system of equations. The number of cells is more than 50000. The height of the water level at the beginning is 0.6, the length is 1.1, the height of the dam is 0.1, Fr = 2, Re = 1000.

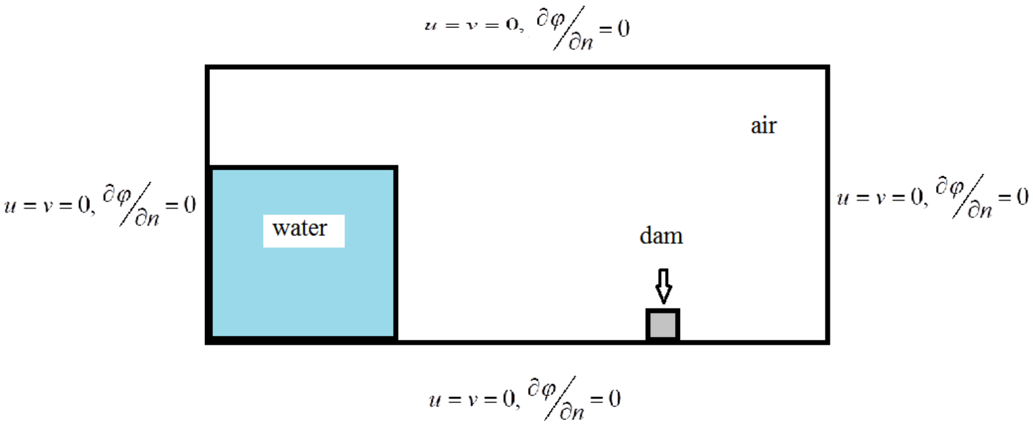

Figure 1 – The diagram of the boundary and initial conditions.

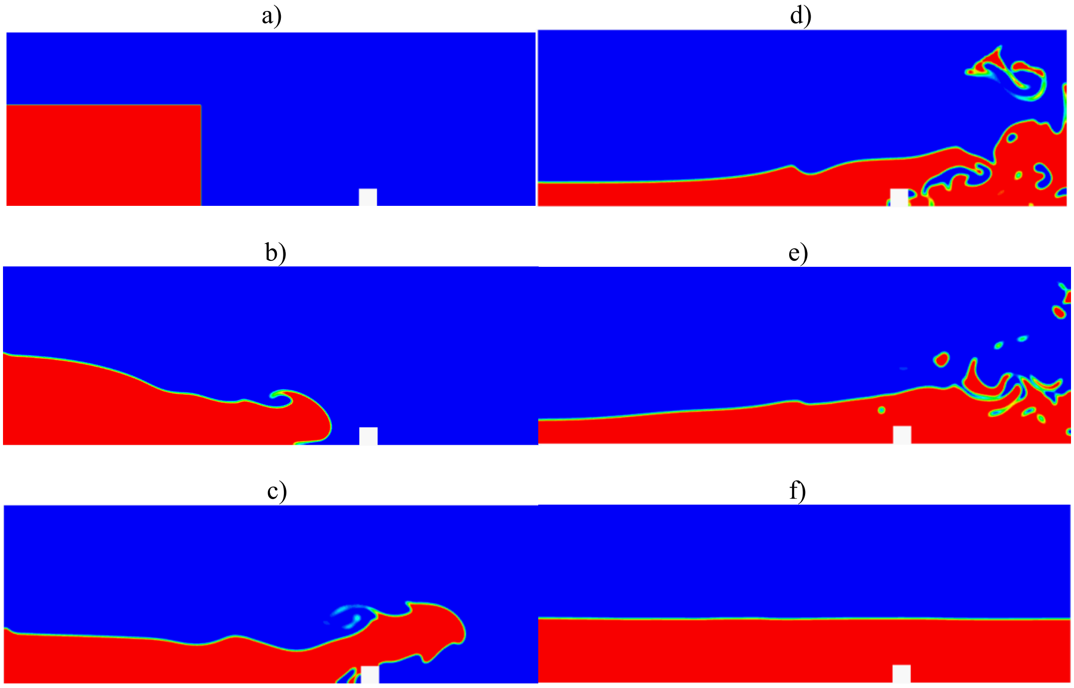

Figure 2 – Movement of the fluid flow with an obstacle in the form of a dam.

The boundary and initial conditions are set as shown in Figure 1 for the physical variables: the phase and velocity components. Figure 2 shows the stages of water motion pictures. Thus, at the initial time (t = 0), there is some water, which occupies the area of a rectangle with a height of 0.6 and 1.1 in length, enclosed by a glass wall on the right side. Further, the enclosure is removed, and the water movement begins in the direction of the dam. So at the picture b) at t = 0.1 water has not yet reached the dam.Further, after reaching the dam, provided that the water does not come in a stationary position, its movement is continued, and it starts to bend around an obstacle, in this case, the dam, as illustrated in Figures b) -f). Initially in this experiment a large amount of water is taken, that covers an area larger than the area of the reservoir, causing the reason why water goes around and bends the dam, which indicates that the height of the protective hydraulic engineering construction is not high enough to stop the water flow.

Conclusion

In carrying out this work, a two-phase mathematical model of fluid movement, based on the full two-dimensional Navier-Stokes equations and Kahn-Hilliard equation was numerically implemented. This mathematical model can be applied in the construction of new hydraulic structures, as well as in predicting of emergencies at already existing dams.

According to the obtained via the numerical studies data, one can say that in the construction of hydraulic structures one needs to take into account inadvance many factors such as the characteristics of the area and the characteristics of the dam in order to minimize the possibility of accidents in the future.

References

1. Biscarini C., Di Francesco S., Manciola P. CFD modeling approach for dam break flow studies // Hydrology and Earth System Sciences. – 2010. – Vol. 14. – P. 705-718.

2. LinaS.-Y., Yang F.-L., Chen C.-S., Hsieh S.-H. A parallel VOF IB pressure-correction method for simulation of multiphase flows // Applied Mathematical Modeling. – 2016. – Vol. 40. – P. 1800-1815.

3. Baker G.R., Meiron D.I., Orzsag S.A. Vortex simulations of the Rayleigh-Taylor instability // Physics of Fluids, – 1980. –Vol. 23. – P. 1485-1490.

4. Duchemin L., Josserand C., Calvin P. Asymptotic behavior of the Rayleigh-Taylor instability // Physical Review Letters. – 2005. – Vol. 94. – P. 224501-1 – 224501-4.

5. Verdon C.P., McCrory R.L., Morse R.L., Baker G.R., Meiron D.I., Orszag S.A. Nonlinear effects of multifrequency hydrodynamic instabilities on ablatively accelerated thin shells // Physics of Fluids. – 1982. – Vol. 25. – P. 1653-1674.

6. Popinet S., Zaleski S. A front-tracking algorithm for accurate representation of surface tension // International Journal for Numerical Methods in Fluids. – 1999. – Vol. 30. – P. 775-793.

7. Tryggvason G., Bunner B., Esmaeeli A., Juric D., Al-Rawahi N., Tauber W., Han J., Nas S., Jan Y.-J. A front-tracking method for the computations of multiphase flow // Journal of Computational Physics. – 2001. – Vol. 169. – P. 708-759.

8. Univerdi S.O., Tryggvason G. A front-tracking method for viscous, incompressible, multi-fluid flows // Journal of Computational Physics. – 1992. – Vol. 100. – P. 25-37.

9.Gerlach D., Tomar G., Biswas G., Durst F. Comparison of volume-of-fluid methods for surface-tension dominant two-phase flows // International Journal of Heat and Mass Transfer – 2006. – Vol. 49. – P. 740-754.

10. Hirt C.W., Nichols B.D. Volume of fluid (VOF) method for the dynamics of free boundaries // Journal of Computational Physics. – 1981. – Vol. 39. – P. 201-225.

11. He X., Chen S., Zhang R. A lattice Boltzmann scheme for incompressible multiphase flow and its application in simulation of Rayleigh-Taylor instability // Journal of Computational Physics. – 1999. – Vol. 152. – P. 642-663.

12.He X., Zhang R., Chen S., Doolen G.D. On the three-dimensional Rayleigh-Taylor instability // Physics of Fluids. – 1999. – Vol. 11. – P. 1143-1152.

13. Nie X., Qian Y.-H., Doolen G.D., Chen S. Lattice Boltzmann simulation of the two-dimensional Rayleigh-Taylor instability // Physical Review E 1998. – Vol. 58. – P. 6861-6864.

14. Chang Y.C., Hou T.Y., Merriman B., Osher S. Eulerian capturing methods based on a level set formulation for incompressible fluid interfaces // Journal of Computational Physics. – 1996. – Vol. 124. – P. 449-464.

15. Gomez P., Hernandez J., Lopez J. On the reinitialization procedure in a narrow-band locally refined level set method for interfacial flows // International Journal for Numerical Methods in Engineering. – 2005.– Vol. 63. – P. 1478-1512.

16. Sussman M., Smereka P., Osher S. A level set approach for computing solutions to incompressible two-phase flow // Journal of Computational Physics. – 1994. –Vol. 114. – P. 146-159.

17. Celani A., Mazzino A., Muratore-Ginanneschi P., Vozella L. Phase-field model for the Rayleigh-Taylor instability of immiscible fluids // Journal of Fluid Mechanics. – 2009. – Vol. 622. – P. 115-134.

18. Ding H., Spelt P.D.M., Shu C. Diffuse interface model for incompressible two-phase flows with large density ratios // Journal of Computational Physics. 2007.– Vol. 226. – P. 2078-2095.

19. Jacqmin D. Calculation of two-phase Navier-Stokes flows using phase-field modeling // Journal of Computational Physics. – 1999. – Vol. 155. – P. 96-127.

20. Anderson J.D. // Computational Fluid Dynamics the Basics with Applications. – 1995. – 547 p.

21. Chung T.J. Computational fluid dynamics. // CUP. – 2002.

UDC 517.9:004.9; 519.711.3

Karzhaubayev K.K.

Faculty of Mechanics and Mathematics,
al-Farabi Kazakh National University, Almaty, Kazakhstan
e-mail: kairzhan.k@gmail.com

Modeling oil pollution of the Caspian Sea resulting from the Ural and Volga rivers input

Abstract. A 2D transport model has been developed to predict the oil pollution resulting from river discharges. The transport module of the model computes two-dimensional Reynolds averaged Navier-Stokes equations (RANS) and uses scalar transport equation to predict the motion of the oil slick. The basic processes affecting the fate of the oil spill are taken into account and parameterized in the transport model. The model is used to simulate a continuous oil release from the Volga and Ural rivers into the coastal waters of the north part of the Caspian Sea. Oil slick movement and risk of contamination of the coastline by beaching oil spills are illustrated for different wind conditions.

Key words: Caspian Sea, oil spill, river discharge, mathematical modeling.

Introduction

The Caspian Sea is the largest inland sea on the planet and located at the Caspian lowland (fig. 1). Sea surface area is about 384 thousands km2., volume is 78 thousand km3. and coastline is more than 7 thousands km. Five countries share the Caspian sea coastline. They are – Kazakhstan, Russia, Azerbaydzhan, Turkmenistan and Iran [1]. The Caspian is divided into three distinct physical regions: the Northern, Middle, and Southern Caspian. The Northern Caspian only includes the Caspian shelf, and is very shallow, it accounts for less than 1% of the total water volume with an average depth of only 5–6 meters. The sea noticeably drops off towards the Middle Caspian, where the average depth is 190 meters. The Southern Caspian is the deepest, with oceanic depths of over 1000 meters. Hydro-dynamical conditions on the Caspian Sea are defined by large longitudinal extension of the sea, high depth difference between northern and southern parts and irregular coastline geometry. The Caspian Sea is fed by numerous rivers, but the Volga and Ural rivers contributes about 85 % of the annual input [2, 3].

Development of the oil production and transportation industry led to the increase of the sea pollution. The Volga and Ural are major conduits of pollutants to the Caspian Sea including oil pollution. The estimated amount of the pollution input is given in Table 1 [4]. Most part of the river input pollution comes from the Volga and Ural.

Oil discharged to the sea surface is transported by convection and influenced by various processes, such as evaporation, emulsification, dissolution, photolysis, biodegradation, etc. These processes are characterized by different time scales at which they interact with the environment. Winds and surface currents are the main sources of energy for the oil slick movement. Several authors summarized such dynamics for water-oil interaction [5-7].

At the moment two most popular universal frameworks for ocean and sea water flow modeling are POM and FVCOM. POM – Princeton Ocean Model [8] computes hybrid 2D-3D dynamics of the sea on a structured grid. FVCOM mostly deals with the same model as POM, but numerical method uses finite volume method with coastline following triangular mesh [9].

This paper is structured as follows: In Section 2 mathematical model and boundary conditions for oil spill transportation and its implementation for the Caspian Sea are described. Numerical method is described in Section 3. Results of simulations of oil slick resulting from the Volga river discharge for different wind conditions are analyzed in Section 4. A short summary is given in Section 5.

Mathematical model

Transport model is based on numerical solution of the RANS equations (1-3) [10]. The model is used to simulate a continuous oil release from the Volga and Ural rivers into the coastal waters of the north part of the Caspian Sea.

$$\frac{\partial u}{\partial t} + u\frac{\partial u}{\partial x} + v\frac{\partial u}{\partial y} - fv = -\frac{1}{\rho_0}\frac{\partial(p)}{dx} + \nu_{eff}\left(\frac{\partial^2 u}{\partial x^2} + \frac{\partial^2 u}{\partial y^2}\right) + F_u \tag{1}$$

$$\frac{\partial v}{\partial t} + u\frac{\partial v}{\partial x} + v\frac{\partial v}{\partial y} + fu = -\frac{1}{\rho_0}\frac{\partial(p)}{dy} + \nu_{eff}\left(\frac{\partial^2 v}{\partial x^2} + \frac{\partial^2 v}{\partial y^2}\right) + F_v \tag{2}$$

$$\frac{\partial u}{\partial x} + \frac{\partial v}{\partial y} + \frac{\partial w}{\partial z} = E \tag{3}$$

$$\frac{\partial C}{\partial t} + u\frac{\partial C}{\partial x} + v\frac{\partial C}{\partial y} = \alpha_{eff}\left(\frac{\partial^2 C}{\partial x^2} + \frac{\partial^2 C}{\partial y^2}\right) + F_C \tag{4}$$

$$\frac{\partial S}{\partial z} = 0,\ \text{at}\ z = \zeta(x, y, t) \tag{5}$$

Table 1 – Oil pollution load to the Caspian sea

Source	Amount (tons/year)
Rivers	75000
Municipalities	19000
Industries	28000
Atmosphere	350
Total	122350

Figure 1 – The Caspian Sea (source: https://commons.wikimedia.org)

Numerical method

Coastline following unstructured finite volume mesh was generated from the free access World coastline vector map layer [11] with the Gmsh[12] mesh generator (fig. 2). Sharp borders of the mesh were smoothed by several Jacobi relaxation procedures. The equation set is solved numerically with a finite volume Navier–Stokes solver using unstructured two-dimensional non-orthogonal grid, with Cartesian vector and tensor components and collocated variable arrangement [13]. The second order accurate central difference scheme (CDS) is applied for discretization of diffusive terms. For the convective terms, the second-order accurate linear upwind (LUDS) is applied by using a deferred correction.

The SIMPLE algorithm is used for the treatment of the pressure fields. Underrelaxation parameters (w) were used for the velocity (w=0.8) and pressure (w=0.2). For unsteady simulations, a fully implicit second order three-time-level marching scheme is used.

Results

According to the main question: will pollution from the Ural and Volga reach Kazakhstan part of the Caspian, and how much time it will take ?, following case was considered. Constant 5m/s east directed wind. Constant sea surface temperature was 20 C. Total oil pollution release intensity was 8.5 tons per hour. It is obvious that such case is most dangerous meteorological condition for Kazakhstan. Simulation results are depicted in fig. 2-6. The Volga and Ural rivers starts to introduce continuous pollution at the initial time (fig. 3a). Oil slick movement affected by wind and surface stress leads to the pollution of the middle sea part and the coastal region. Numerical simulations show that low speed wind (<2-3 m/s) does not affect marine flow much. On the other hand large longitudinal extend of the Caspian makes Coriolis force more significant. According to the simulation data continuous pollution sources from the Ural and Volga may reach Kazakhstan part of the coastline in about 20-25 days.

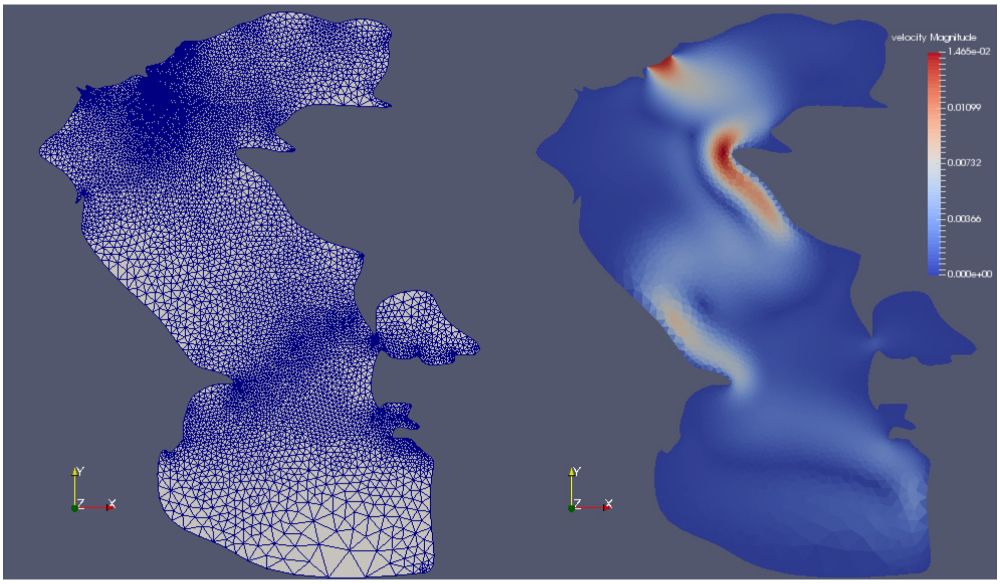

a b

Figure 2 – a) Computational mesh, b) Flow pattern on the Caspian Sea.

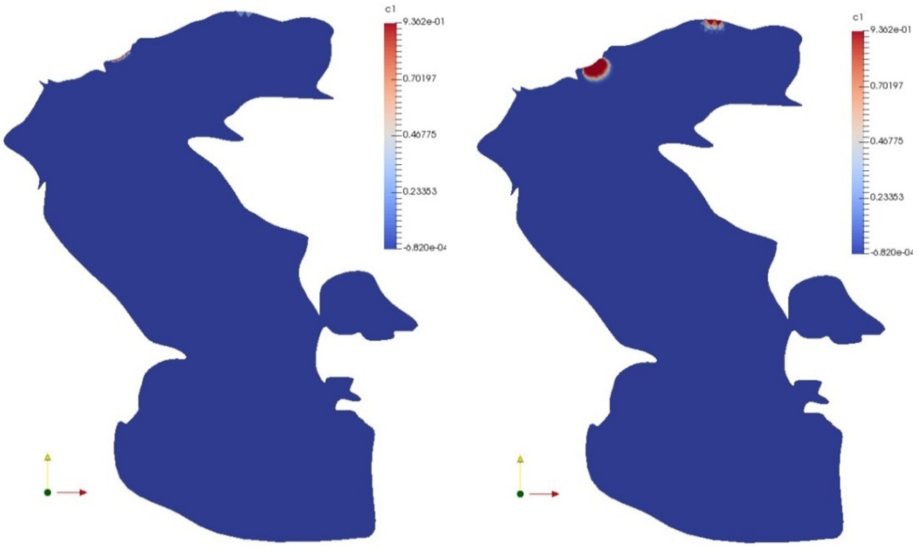

a b

Figure 3 – Pollution transport on the Caspian Sea, a) –t=0 min, b) –t=1728 min.

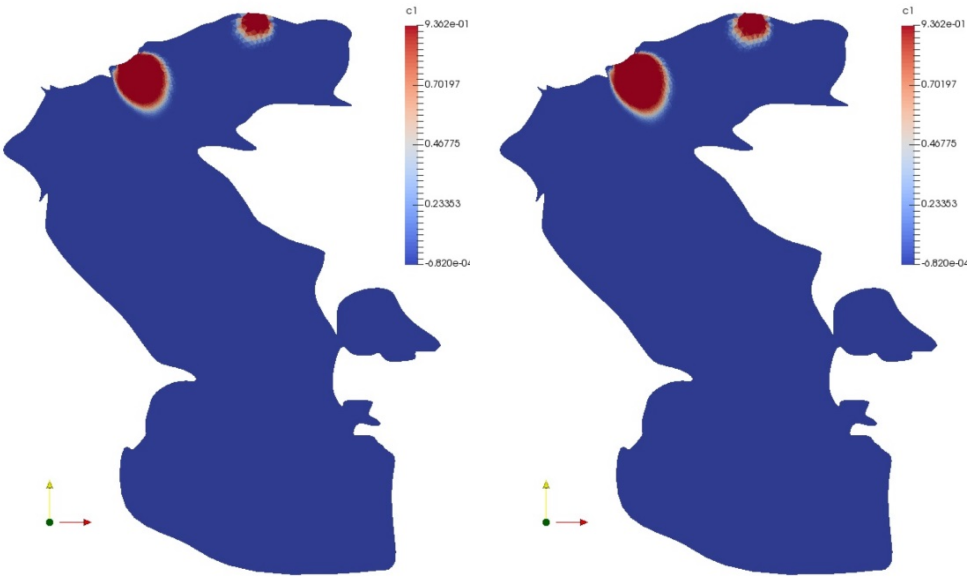

a b

Figure 4 – Pollution transport on the Caspian Sea, a) –t=10368 min, b) –t=12096 min.

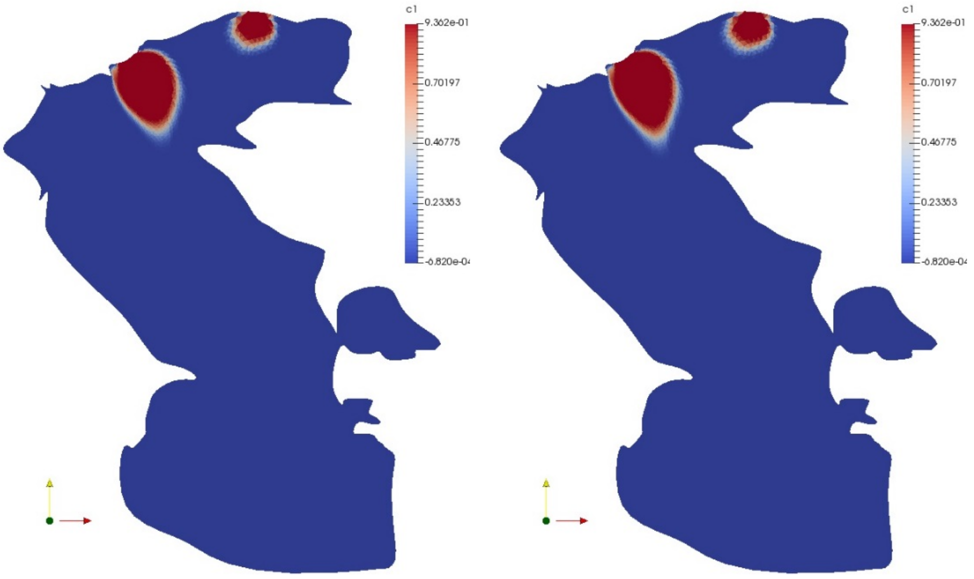

a b

Figure 5 – Pollution transport on the Caspian Sea, a) –t=17280 min, b) –t=19008 min.

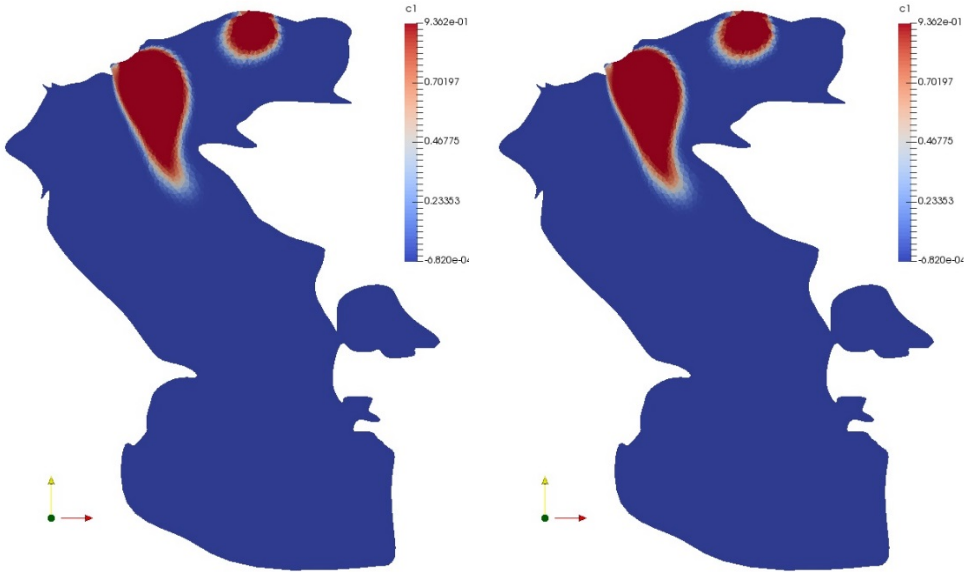

a b

Figure 6 – Pollution transport on the Caspian Sea, a) –t=31104 min, b) –t=32832 min.

Conclusion

A 2D transport model has been developed to predict the oil pollution resulting from river discharges in an in-house CFD code CFVM. The transport module of the model computes two-dimensional Reynolds averaged Navier-Stokes equations (RANS) using k-epsilon turbulence model. Oil slick movement is governed by scalar transport equation. Among the processes affecting the fate of oil, advection, turbulent diffusion, evaporation, and decay are included; the decay is modeled as the combined effect of all the biochemical and physical mechanisms that decompose oil.

The transport model has been implemented for the Caspian Sea to predict oil slick movement and the area covered by the oil. Coastline pollution by the oil slick illustrated on artificial meteorological case. Numerical experiments with 25-day scenarios of the possible oil input resulting from the Volga and Ural rivers discharge show the potential threat caused by beaching and cross-boundary transport of the oil pollution in the northern part of the Caspian Sea.

Further modifications to the model and its implementation are related to the introduction of the bathymetry (sea depth), wave-oil slick interaction and usage of finer grids on high performance computing systems. First two modifications have to be supported by significant model modification, third is highly related to efficient domain decomposition and parallel computations.

References

1. Kireev M.A. Reshenie gidrometeorologicheskih problem v ramkah Kaspijskojj ekologicheskoj programmy. // Problemy gidrometeorologii i ekologii: Materialy Mezhdunar. nauch.-prakt. konf., posvjashhennoj 50-letiju KazNIIMOSK. – Almaty: KazNIIMOSK, – 2001. – P. 114-115.
2. Sydykov Zh.S., Golubcov V.V., Kuandykov B.M. Kaspijskoe more i ego pribrezhnaja zona (prirodnye uslovija i ekologicheskoe sostojanie). Almaty, – 1995. – P. 211.
3. Budyko M.I. Izmenenie klimata. // L. Gidrometeo izdat. – 1974. – P. 280.
4. Korotenko K. A. et al. Particle tracking method in the approach for prediction of oil slick transport in the sea: modelling oil pollution resulting from river input // Journal of Marine Systems. – 2004. – Vol. 48. – No 1. – P. 159-170.
5. Mackay D., McAuliffe C. D. Fate of hydrocarbons discharged at sea // Oil and Chemical Pollution. – 1989. – Vol. 5. – No 1. – P. 1-20.
6. Spaulding M. L. A state-of-the-art review of oil spill trajectory and fate modeling // Oil and

Chemical Pollution. – 1988. – Vol. 4. – No 1. – P. 39-55.

7. Korotenko K.A., Mamedov R.M., Mooers C. N. K. Prediction of the transport and dispersal of oil in the south Caspian Sea resulting from blowouts // Environmental Fluid Mechanics. – 2001. – Vol. 1. No 4. – P. 383-414.

8. Giunta G. et al. pPOM: A nested, scalable, parallel and Fortran 90 implementation of the Princeton Ocean Model //Environmental Modelling & Software. – 2007. – Vol. 22. – No 1. – P. 117-122.

9. Cowles G.W. Parallelization of the FVCOM coastal ocean model //International Journal of High Performance Computing Applications. – 2008. – Vol. 22. – No 2. – P. 177-193.

10. Razrabotka geoinformatsionnoy sistemy modelirovaniya avariynykh razlivov nefti na kaspiyskom more dlya planirovaniya deystviy v usloviyakh chrezvychaynykh situatsiy // Projectreport / DGPSSIMM, proj. leader. A.K. Khikmetov. Almaty. – 2015.

11. http://www.naturalearthdata.com/downloads/10m-physical-vectors/10m-coastline/

12. Geuzaine C., Remacle J. F. Gmsh: A 3-D finite element mesh generator with built-in pre-and post-processing facilities // International Journal for Numerical Methods in Engineering. – 2009. – Vol. 79. – No 11. – P. 1309-1331.

13. Hanjalić K., Kenjeres S., Jonker H.J.J. Analysis and modelling of physical transport phenomena. – 2007.

International Journal of Mathematics and Physics 7, №2, 36 (2016)

UDC 532.1

*Maussumbekova S.D., Polyakova I.

Faculty of Mechanics and Mathematics,
al-Farabi Kazakh National University, Almaty, Kazakhstan
*e-mail:saulemaussumbekova@gmail.com

Numerical modeling of pollutant transport in the atmospheric boundary layer using ANSYS

Abstract. The purpose of research is to simulate the dynamics of wind velocity distribution, impurities in the atmospheric boundary layer using ANSYS software system. Computational modeling is a basis for successful environmental problems researches, in particularly, to predict the spread of polluting substances, hazardous gas clouds and impurities in the air from man-made sources and optimization the financial costs of environmental measures. The solution of such problems requires the achievement of the following objectives: the mathematical model creation of the atmospheric boundary layer dynamics,design scheme description, setting the boundary and initial conditions, the process of problem solving, convergence solution control,the results processing and analyzing, what was done in this paper.

Key words: atmospheric boundary layer, numerical modeling, ANSYS software system, spread of polluting substances

Introduction

Pollution increases due to increasing anthropogenic stresses environmental, particularly in the atmosphere. Therefore, monitoring and forecasting of air pollution have always been and remain an important issue. The essence of the study is to model the dynamics of inhomogeneous turbulent flows of different substances occurring on the non-uniform earth's surface in the atmospheric boundary layer due to increased air contamination with dust and condensation products. The atmospheric boundary layer is the layer of air between 300-400 m. to 1-2 km. adjacent to theearth's surface.Turbulence is important in the boundary layer. In this regard, the properties of the boundary layer are mainly determined by thermal and dynamic effects of the underlying surface.

Examination of physical processes and phenomena in the layer of the atmosphere at 200-2000 meters thick, concerning the earth's surface has an essential scientific and practical significance. The structure of the layer affects on flora and fauna of the planet, on the populations life conditions greatly.

The regularity of physical processes occurring in the boundary layer and other atmospheric layers different in many ways. Status of the boundary layer is very closely linked to the state of the Earth surface. Meteorological values are subjected to sudden changes in the atmospheric boundary layer with altitude and time. The vertical gradients of meteorological components are higher in the given layer than in the other layers [1].

Main body

To calculate the immense amount of researches and applications weneed to find vertical profiles of meteorological elements and characteristics of the atmospheric boundary layer (ABL), characterizing the meteorological phenomena that occur in it, and even the processes of pollutants and aerosols transport. Solving horizontally inhomogeneous ABL problems is the most difficult process [2].

The most famous modern product is ANSYS software system, which is a multi-purpose software package for physical processes and phenomena numerical modeling.

ANSYS Workbench is software platformwith extensive capabilities for integrating different applications into a single workspace and exchanging data between them. Workbench project is a virtual spacewhichform the calculating pattern using various combinations of modules [3].

Five tasks were solved in order to create a model of the atmospheric boundary layer dynamics in ANSYS Workbench:

- geometric model creation / import;

- computational domain spatial discretization (geometric area covering with finite element / finite volume grid);
- physics-mathematical model selection, design scheme description, setting the boundary and initial conditions;
- the process of problem solving, convergence solution control;
- the results processing and analyzing.

The first step in solving the problem was the creation of geometrical model in the Design Modeler module. The area of 6000 m (horizontal size)to 1500 m (vertical size) werechosen to set the atmospheric boundary layer geometry.Spatial sampling computational domain wasmade at the second stage, which corresponds initial geometric model obtained in the first step.Construction of gridswas made by using Meshing module. Computational grid (dimensionis 200×80) was built for the task. Grid built with pressed boundary layers near the solid boundary (land) using Sizing component. Mesh generation performed with Mapped Face Meshing method.

The third step of solving the problem is the right choice of necessary design module. ANSYS FLUENT module was used to obtain the solution of the nonstationary problem.

The ANSYS software complex pays special attention to the advanced turbulence models development for efficient and accurate calculation of turbulent processes. The calculation of the problem occurred on two-parameter k-ε turbulence model. Two differential equations for the turbulent kinetic energy transfer and the transfer of turbulence dissipation are solved in presented model. Enhanced Wall Functions was used in this model of turbulence. This method is obtained by combining linear (laminar) and logarithmic (turbulent) laws of the wall, using the function proposed by Kader [4].

An important step in calculation model preparation is the materials selection with specifying their physical properties in the Materials section of the project tree. Four materials were selected for the problem: air, nitrogen, oxygen, water-vapor. The percentage of each component in the air was found according to meteorological data in the boundary conditions of the problem.

In the paper the following boundary conditions were set at the entrance to the computational domain:Velocity Inlet condition. It is useful for specifying velocity and scalar parameters.Since wind speed varies with height, the input condition was for velocity was:

$$U(z) = U_0 \cdot \left(\frac{y}{H} \right)^{\beta} \tag{1}$$

where, U_0 is the wind flow average speed at height H, β is the coefficient depending on the terrain type.The temperature was set by temperature distribution according to the height.The temperature is lowered by1°C for every 100 m.Such plot is described by the equation:

$$T(z) = T_0 - \gamma y \tag{2}$$

where T_0 is the temperature at the earth's surface; $\gamma$is the vertical gradient of temperature [5].

The boundary conditions on the wall:

- On-slip condition at the wall.
- The temperature of the wall is15°C.

Pressure-Based solver setups were selected at the fourth stage. Pressure-Based solver connects the calculating algorithm for the Navier-Stokes equations, based on the pressure correction method. Initialization is performed using Solution Initialization window. By default, there is the hybrid method of initialization, in which the pressure and velocity fields are determined by solving the Laplace equation.

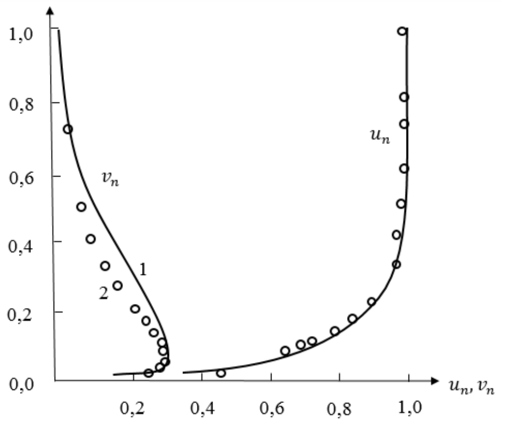

Figure 1 – Vertical profiles of wind speed with U = 6.6 m/s
1 – calculated profile, 2 – experimental points

The results of the atmospheric boundary layer dynamics calculations

Comparison of the numerical solutionresults with field profiles of the wind in the atmospheric boundary layer from measure were presented by Vager B.G. and Nadezhina E.D. [5]. Results of the study are presented in Figure 1, which shows that for different values of the geostrophic wind u_n-componentprofile of the wind speed is almost the same as the experimental. However, between the calculated and experimental v_n-component profile there are differences in the middle part of the boundary layer.

Below there are the results of wind speed u, v – components numerical calculations in the PC ANSYS

The dynamics of the velocity components (u, v) (Fig. 2) is qualitatively consistent with the results from [5], (Fig. 1), which allows us to conclude that the assembled model in ANSYS is adequate.

Modern studies of large urban environment, as well as theoretical and applied environmental problems associated with them, have a considerable interest, as the city became a leading place of human habitation. Modeling of carbon dioxidesdynamics will help to better understanding how CO_2 can accumulate and affect the Earth's atmosphere, and what methods can be taken for the planet conservation.

Figures 3, 4 show the distribution of CO_2 in the air from the emission source at different times, when the wind speed is 3 m/s (Figures 3) and 12 m/s (Figures 4).

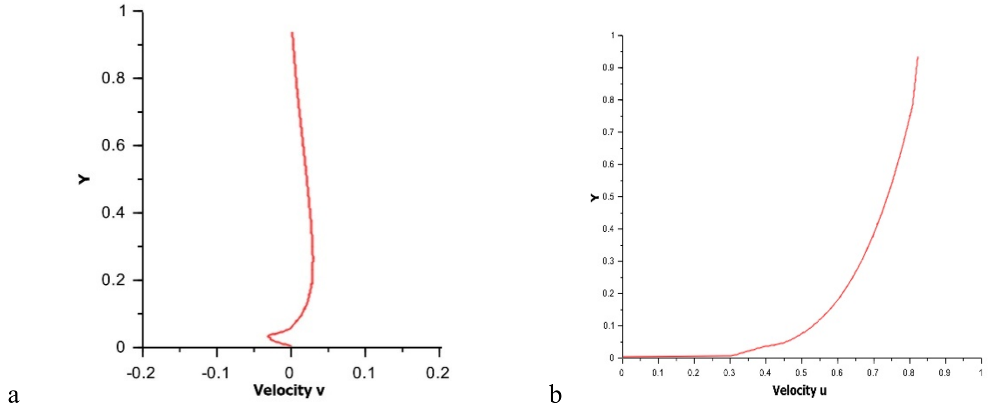

Figure 2 – Wind speed profile with U_0=6.6 m/s
a) u-component; b) v-component

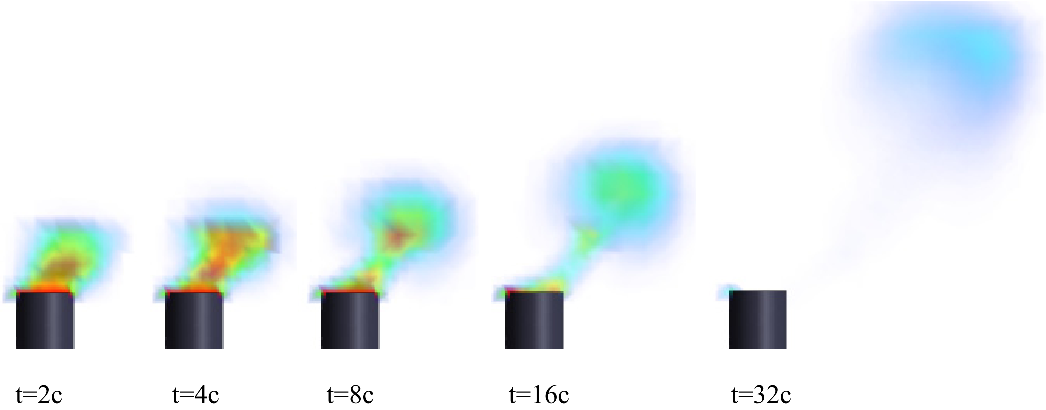

Figure 3 – Distribution of CO_2 in the air from the emission source
at different times with wind speed 3 m/s

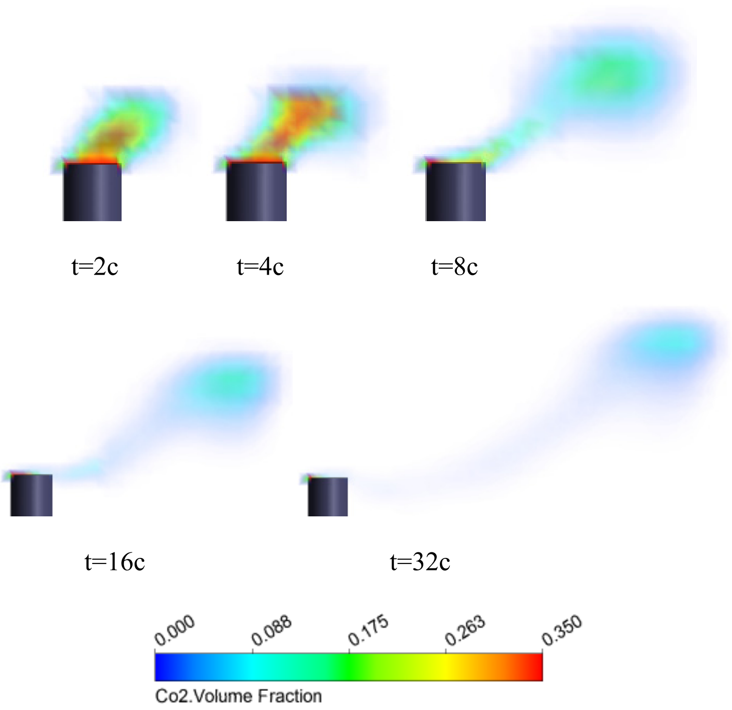
t=2c t=4c t=8c

t=16c t=32c

Figure 4 – Distribution of CO_2 in the air from the emission source at different times with wind speed 12 m/s

The initial condition was indication of CO_2volume fraction – 0.350. According to Figure 3CO_2 spread differs slightly (only at 230-250 m) after four seconds from the emissionstart with wind speed of 3 m/s and 12 m/s. The maximum concentration of CO_2 is observed near the source of emission. After 8 seconds there is the emergence of two foci with the highest concentrations: near the source of emission and less pronounced at the distance of 200 m with wind speed of 3 m/s and 250 m with 12 m/s horizontally.The emissions extend to a height of about 300 m in the vertical direction. Horizontal compiling increases with rising transfer duration of impurities, so by 32 seconds the highest concentration observed at a distance of 600 meters from the source at a wind speed of 3 m/s and 1200 m at 12 m/s. While the greatest concentration of the cloud is located at an altitude of 1000 m. Concentration becomes less with more impurities transfer.

Conclusion

Numerical experiments allow to solve problems environmental impact assessment of pollution spreading from man-made sources in the project stage with sufficient accuracy. Modern computational models for analyze and forecast the state of the surrounding environment will help to minimize the environmental hazard degree, improve the comfort level of population accommodation and recreation and optimize the financial costs of environmental measures.

References

1. Matveev L.T. Atmospheric Physics. – SPb.: Gidrometeoizdat, 2000. – 777 p.
2. Bezuglova N.N., Sukovatov Yu.A., Sukovatov K. Yu. The use of turbulence equations for calculating the horizontal-inhomogeneity atmospheric boundary layer // Polzunovsky Herald. – 2004. – No 2. – P. 103-105.
3. Valger S.A., Danilov M.N., Zakharova Yu.V., Fedorova N.N. Basics of PC ANSYS 16.0: tutorial. – Novosibirsk: NSABU, 2015. – 240 p.
4. Kader B. Temperature and Concentration Profiles // Journal of Heat and Mass Transfer. – 1981. – Vol. 9, No24. – P. 1541-1544.
5. Vager B.G., Nadezhina E.D. The Atmospheric Boundary Layer under Condition of Horizontal Inhomogeneity. – L.: Gidrometeoizdat, 1979. – 136 p.
6. Belotserkovsky O.M. Numerical modeling in continuum mechanics. – M.: Fizmatlit, 1994.– 442p.

UDC 531.391

Bismildin I.R.

Faculty of Mechanics and Mathematics,
al-Farabi Kazakh National University, Almaty, Kazakhstan
e-mail: mech.math360@gmail.com

On the study of Rigid Body Inertia

Abstract. In the classical finite element literature beams and plates are not considered as isoparametric elements since infinitesimal rotations are used as nodal coordinates. As a consequence, exact modeling of an arbitrary rigid body displacement cannot be obtained, and rigid body motion does not lead to zero strain. In order to circumvent this problem in flexible multibody simulations, an intermediate element coordinate system, which has an origin rigidly attached to the origin of the deformable body coordinate system and has axes which are parallel to the axes of the element coordinate system in the undeformed configuration was introduced. The correct equations of motion, however, can be obtained if the coordinates are defined in terms of global slopes. Using this new definition of the element coordinates, an absolute nodal coordinate formulation that leads to a constant mass matrix for the element can be developed. Using this formulation, in which no infinitesimal or finite rotations are used as nodal coordinates, beam and plate elements can be treated as isoparametric elements.

Key words: rigid body, inertia, finite, element method, multibody systems, dynamics.

Introduction

With regard to the dynamics of constrained deformable bodies that undergo large rigid body rotations, there are three well known solution procedures which are briefly summarized below:

(1) Floating Frame of Reference. In this approach, a coordinate system is assigned to each deformable body in the multibody system. The configuration of the deformable body is identified using two sets of coordinates that define the location and orientation of the deformable body coordinate system, as well as the deformation of the body with respect to its coordinate system. Cartesian Coordinate formulations as well as recursive methods are often used with the floating frame of reference approach.

(2) Incremental Finite Element Approach. In this approach, the nodal coordinates of the finite elements are used to describe incrementaly the large rigid body rotations of the elements. The equations of motion are formulated in terms of the nodal coordinates only and a convected element coordinate system is used to define the current element configuration.

(3) Large Rotation Vector. This approach was introduced recently in order to avoid the linearization that results from the use of the incremental finite element approach. In this approach, the element rotations are described using a finite rotation vector defined at the element nodal.

In the large deformation analysis, rate constitutive equations must correctly represent the relationship between the stress rate and the arbitrary rigid body translation and rotation. The displacement increment over the step was defined and the gradient of this displacement was used to define the strain and rotation tensors, which are, in turn, used to define the algorithm for integrating the constitutive equations. Flanagan and Taylor presented a numerical algorithm for the integration of constitutive equations under both large deformations and/or large rotations. The examples showed the relative efficiency of the unrotated configuration, and the computational efficiency and accuracy of the numerical algorithms in dealing with large rotation problems and its insensitivity to orientation.

Several numerical integration algorithms were proposed in order to improve the computational efficiency and accuracy of the solution for dynamic structural systems. In some of these numerical algorithms, criteria were introduced in order to preserve some basic rigid body quantities such as the linear and angular moment and the kinetic energy. These criteria ensure that these basic quantities are not compromised during the process of the numerical integration provided that the exact rigid body equations of motion including the exact mass moments and products of inertia are used. Using this hypothesis, it is assumed that the error in the solution is mainly the result of the numerical integration. As demonstrated in this paper and in previous publications, some of the commonly used shape functions and the associated nodal coordinates can not be used to define the exact rigid body equations of motion, and therefore, it becomes necessary to quantify the errors in the basic dynamic equations prior to investigating the accuracy of the numerical integration methods.

In this formulation, no infinitesimal or finite rotations are used as nodal coordinates, instead, absolute displacements and slopes are used to define the element configuration in the global coordinate system. The absolute slopes can be determined in the undeformed reference configuration using spatial rigid body kinematic equations.

Finite Element and Rigid Body Inertia

In the classical finite element literature, beams and plates are not considered as isoparametric elements. The use of the infinitesimal rotations as nodal coordinates leads to linearized kinematic equations which do not describe exact rigid body motion. In order to utilize existing finite element methodologies and computer programs, the concept of the intermediate element coordinate system was introduced in order to obtain an exact modeling of the rigid body inertia using the conventional finite element shape functions.

Since the conventional element shape functions contain rigid body modes that describe arbitrary translations, the exact location of an arbitrary point on the beam, in an intermediate coordinate system which differs from the element coordinate system by a translation in the undeformed configuration, can be defined using this element shape function. As a consequence, the exact rigid body mass moments and products of inertia as well as the moments of mass can be evaluated using the element shape function and the vector of element nodal coordinates.

Rigid Body Inertia. In the three dimensional analysis, the inertia forces of the rigid body are defined in terms of the inertia tensor and the moments of mass. The rigid body inertia tensor for a spatial system is defined as

$$\overline{I}_{\theta\theta} = \int_V \rho \tilde{\bar{u}}^T \tilde{\bar{u}} dV \tag{1}$$

where the superscript T indicates a transpose of a vector or a matrix, is the inertia tensor defined in the body coordinate system, $\boldsymbol{\rho}$ is the mass density, $\boldsymbol{V}$ is the volume and $\tilde{\bar{u}}$ is the skew symmetric matrix associated with the vector $\bar{u}$ that defines the local position of an arbitrary point on the body. The skew symmetric matrix $\tilde{\bar{u}}$ can be written as

$$\tilde{\bar{u}} = \begin{bmatrix} 0 & -\bar{u}_3 & \bar{u}_2 \\ \bar{u}_3 & 0 & -\bar{u}_1 \\ -\bar{u}_2 & \bar{u}_1 & 0 \end{bmatrix} \tag{2}$$

where $\bar{u}_1$, $\bar{u}_2$ and $\bar{u}_3$ are the components of the vector $\bar{u}$, that is

$$\bar{u} = [\bar{u}_1 \quad \bar{u}_2 \quad \bar{u}_3]^T$$

The inertia tensor for the rigid body can be written more explicitly as

$$\bar{I}_{\theta\theta} = \begin{bmatrix} i_{11} & i_{12} & i_{13} \\ & i_{22} & i_{23} \\ symmetric & & i_{33} \end{bmatrix} = \int_V \rho \begin{bmatrix} \bar{u}_2^{\,2} + \bar{u}_3^{\,2} & -\bar{u}_2\bar{u}_1 & -\bar{u}_3\bar{u}_1 \\ & \bar{u}_1^{\,2} + \bar{u}_3^{\,2} & -\bar{u}_3\bar{u}_2 \\ symmetric & & \bar{u}_1^{\,2} + \bar{u}_2^{\,2} \end{bmatrix} dV \tag{3}$$

In the case of a slender beam element, the vector u can be written as

$$\bar{u} = [x \quad 0 \quad 0]^T$$

where $\boldsymbol{x}$ is the position of the arbitrary point from the endpoint which defines the origin of the beam coordinate system .

Using the vector $\bar{u}$ the inertia tensor of the slender beam element can be obtained

as $$\bar{I}_{\theta\theta} = \begin{bmatrix} 0 & 0 & 0 \\ 0 & \frac{ml^2}{3} & 0 \\ 0 & 0 & \frac{ml^2}{3} \end{bmatrix}$$

where m is the mass of the beam element and l is its length.

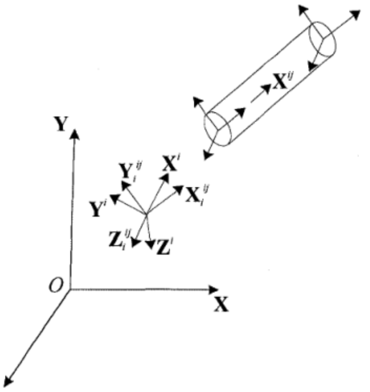

Figure – Three dimensional beam element

The moment of mass of the beam is defined as

$$M_0 = \int_V \rho \bar{u}\, dV$$

Using the vector u of the slender beam, one can show that the moment of mass is defined as

$$M_0 = \begin{bmatrix} \frac{ml}{2} \\ 0 \\ 0 \end{bmatrix}$$

Shape Function. If the shape function can be used to describe an arbitrary rigid body translation, the element nodal coordinates and the shape function can be used to define the location of an arbitrary point on the element with respect to the element coordinate system. In this case, the vector $\bar{u}$ can be written as

$$\bar{u} = Se$$

where $\boldsymbol{S}$ is the shape function matrix of the element and $\boldsymbol{e}$ is the vector of the element nodal coordinates. If the effect of rotary inertia is neglected, the shape function $\boldsymbol{S}$ can be defined in the case of three dimensional beam element as

$$S^T = \begin{bmatrix} 1-\xi & 0 & 0 \\ 0 & 1-3\xi^2+2\xi^3 & 0 \\ 0 & 0 & 1-3\xi^2+2\xi^3 \\ 0 & 0 & 0 \\ 0 & 0 & l\left(-\xi+2\xi^2-\xi^3\right) \\ 0 & l\left(\xi-2\xi^2+\xi^3\right) & 0 \\ \xi & 0 & 0 \\ 0 & 3\xi^2-2\xi^3 & 0 \\ 0 & 0 & 3\xi^2-2\xi^3 \\ 0 & 0 & 0 \\ 0 & 0 & l\left(\xi^2-\xi^3\right) \\ 0 & l\left(\xi^3-\xi^2\right) & 0 \end{bmatrix} \qquad (4)$$

where ξ = x/l, and l is the length of the beam element. If the beam element is considered as a rigid body, then the vector of nodal coordinates defined in the element coordinate system is given by

$$e = \begin{bmatrix} 0 & 0 & 0 & 0 & 0 & 0 & l & 0 & 0 & 0 & 0 & 0 \end{bmatrix}^T$$

In this case one has

$$\bar{u} = Se = \begin{bmatrix} x \\ 0 \\ 0 \end{bmatrix}$$

and as a consequence, the mass moments of inertia of the rigid beam are defined in terms of the element shape function as

$$\left.\begin{aligned} i_{11} &= e^T\left(S_{22}+S_{33}\right)e = 0 \\ i_{22} &= e^T\left(S_{11}+S_{33}\right)e = \frac{ml^2}{3} \\ i_{33} &= e^T\left(S_{11}+S_{22}\right)e = \frac{ml^2}{3} \end{aligned}\right\} \qquad (5)$$

and the products of inertia are

$$i_{jk} = -e^T S_{jk} e = 0$$

$$j,k = 1,2,3 \qquad j \neq k$$

where

$$S_{jk} = \int_V \rho S_j^T S_k dV$$

and S_k is the kth row in the element shape function. Further-more, the moment of mass is defined as

$$M_0 = \int_V \rho Se dV = \bar{S}e = \begin{bmatrix} \frac{ml}{2} \\ 0 \\ 0 \end{bmatrix}$$

where

$$\bar{S} = \int_V \rho S dV$$

In the case of the beam element shape function, the matrix S is given by

$$\bar{S} = \begin{bmatrix} \frac{m}{2} & 0 & 0 & 0 & 0 & 0 & \frac{m}{2} & 0 & 0 & 0 & 0 & 0 \\ 0 & \frac{m}{2} & 0 & 0 & 0 & \frac{ml}{12} & 0 & \frac{m}{2} & 0 & 0 & 0 & -\frac{ml}{12} \\ 0 & 0 & \frac{m}{2} & 0 & -\frac{ml}{12} & 0 & 0 & 0 & \frac{m}{2} & 0 & \frac{ml}{12} & 0 \end{bmatrix}^T \tag{6}$$

It is clear from the analysis presented in this section that all the rigid body inertia quantities can be evaluated using the element shape integrals $\bar{S}$, and S_{jk}.

Intermediate Element Coordinate System

The intermediate element coordinate system shown in Fig. 1 is introduced in flexible multibody simulation in order to obtain exact modeling of the rigid body inertia when the structures undergo arbitrary large rotations. In the initial undeformed configuration, this intermediate coordinate system differs from the element coordinate system by a rigid body translation. The results of the parallel axis theorem, often used in rigid body dynamics, can be obtained, using the element shape function and the intermediate element coordinate system, by utilizing the fact that the position coordinates of an arbitrary point on the finite element can be defined in the intermediate coordinate system using the element nodal coordinates. Before we demonstrate this fact in the general case of three dimensional displacement, we consider the case in which the. origin of the intermediate element coordinate system is located at the center of mass C of the element. In this case, the vector of coordinates defined in the intermediate element coordinate system is

$$e_C = \begin{bmatrix} -\frac{l}{2} & 0 & 0 & 0 & 0 & 0 & \frac{l}{2} & 0 & 0 & 0 & 0 & 0 \end{bmatrix}^T$$

Using this vector of nodal coordinates, the mass moments of inertia can be calculated as

$$\left.\begin{aligned} i_{11} &= e_C^T (S_{22} + S_{33}) e_C = 0 \\ i_{22} &= e_C^T (S_{11} + S_{33}) e_C = \frac{ml^2}{12} \\ i_{33} &= e_C^T (S_{11} + S_{22}) e_C = \frac{ml^2}{12} \end{aligned}\right\} \tag{7}$$

and the products of inertia are

$$i_{jk} = -e_C^T S_{jk} e = 0 \quad j,k = 1,2,3 \quad j \neq k$$

where the matrices S_{jk} are defined in the previous section. The use of equations shows that the moment of mass about the center of mass is

$$M_C = \bar{S} e_C = 0$$

where the matrix $\bar{S}$ in the case of the three dimensional beam element is defined.

General Translations. If the element coordinate system differs from the intermediate element coordinate system by a general three dimensional displacement defined by the vector

$$D = \begin{bmatrix} d_x & d_y & d_z \end{bmatrix}^T \tag{8}$$

the vector of nodal coordinates defined in the intermediate element coordinate system is given by

$$e_I = \begin{bmatrix} d_x & d_y & d_z & 0 & 0 & 0 & d_x + l & d_y & d_z & 0 & 0 & 0 \end{bmatrix}^T$$

In this case, the mass moments and products of inertia can be evaluated using the element shape function **S** and the vector of nodal coordinates as

$$\left.\begin{aligned} i_{11} &= e_I^T \left(S_{22} + S_{33}\right) e_I = m\left(d_y^2 + d_z^2\right) \\ i_{22} &= e_I^T \left(S_{11} + S_{33}\right) e_I = \frac{ml^2}{3} + m\left(d_x(d_x + l) + d_z^2\right) \\ i_{33} &= e_I^T \left(S_{11} + S_{22}\right) e_I = \frac{ml^2}{3} + m\left(d_x(d_x + l) + d_y^2\right) \\ i_{12} &= -e_I^T S_{12} e_I = -d_y\left(md_x + \frac{1}{2}ml\right) \\ i_{13} &= -e_I^T S_{13} e_I = -d_z\left(md_x + \frac{1}{2}ml\right) \\ i_{23} &= -e_I^T S_{23} e_I = -md_y d_z \end{aligned}\right\} \tag{9}$$

which are the exact expressions for the mass moments and products of inertia that can be obtained using the parallel axis theorem used in rigid body dynamics.

The moment of mass is defined in the intermediate element coordinate system as

$$M_I = \overline{S} e_I = \begin{bmatrix} m\left(\frac{l}{2} + d_x\right) \\ md_y \\ md_z \end{bmatrix}$$

The analysis presented in this section demonstrates that exact modeling of the basic inertia quantities can be obtained by using the intermediate element coordinate system, and as a consequence, the use of this coordinate system in the nonlinear flexible multibody formulation does lead to the exact equations of motion of the spatial rigid body.

Examples

In this section, we present three different forms of the equations of motion of the beam obtained using the three different approaches discussed in the preceding sections. The first form represents the exact equations of motion of the beam, the second form is obtained using the convected system approach, while the third form is obtained using the early linearization scheme. In the three cases, for simplicity, we consider a beam which has an arbitrary rigid body translation, and it is allowed to rotate about its **Z** axis.

Exact Equations. The exact equations of motion of the system are

$$\begin{bmatrix} m & 0 & 0 & -\frac{1}{2}ml\sin\theta \\ 0 & m & 0 & \frac{1}{2}ml\cos\theta \\ 0 & 0 & m & 0 \\ -\frac{1}{2}ml\sin\theta & \frac{1}{2}ml\cos\theta & 0 & \frac{1}{3}ml^2 \end{bmatrix} \cdot \begin{bmatrix} \ddot{R}_x \\ \ddot{R}_y \\ \ddot{R}_z \\ \ddot{\theta} \end{bmatrix} = \begin{bmatrix} Q_{ex} \\ Q_{ey} \\ Q_{ez} \\ Q_{e\theta} \end{bmatrix} + \begin{bmatrix} Q_{vx} \\ Q_{vy} \\ Q_{vz} \\ Q_{v\theta} \end{bmatrix} \tag{10}$$

where R_x, R_y, R_z, are the translational coordinates of the reference point of the beam, в is the angle that defines the beam orientation, Q_{ex}, Q_{ey}, Q_{ez}, and $Q_{e\theta}$ are the components of the vector of generalized external forces and Q_{vx}, Q_{vy}, Q_{vz} and $Q_{v\theta}$ are the components of the vector of centrifugal forces. The components of the vector of centrifugal forces are

$$Q_v = \begin{bmatrix} \frac{1}{2} ml\dot{\theta}^2 \cos\theta \\ \frac{1}{2} ml\dot{\theta}^2 \sin\theta \\ 0 \\ 0 \end{bmatrix} \tag{11}$$

Convective System. For the beam model used in this section, we define the system generalized coordinate vector as

$$q = \begin{bmatrix} R_x & R_y & R_z & \theta \end{bmatrix}^T \tag{12}$$

In terms of the components of this vector, the vector of nodal coordinates, in the case of the convective system, can be written as

$$e = \begin{bmatrix} R_x & R_y & R_z & 0 & 0 & 0 & R_x + l\cos\theta & R_x + l\cos\theta & R_z & 0 & 0 & 0 \end{bmatrix}^T$$

and the velocity vector is

$$\dot{e} = B\dot{q} \tag{13}$$

where B is the velocity influence coefficient matrix defined as

$$B = \begin{bmatrix} 1 & 0 & 0 & 0 & 0 & 0 & 1 & 0 & 0 & 0 & 0 & 0 \\ 0 & 1 & 0 & 0 & 0 & 0 & 0 & 1 & 0 & 0 & 0 & 0 \\ 0 & 0 & 1 & 0 & 0 & 0 & 0 & 0 & 1 & 0 & 0 & 0 \\ 0 & 0 & 0 & 0 & 0 & 0 & -l\sin\theta & l\cos\theta & 0 & 0 & 0 & 0 \end{bmatrix}^T \tag{14}$$

The kinetic energy of the beam is

$$T = \frac{1}{2}\int_V \rho \dot{\bar{u}}^T \dot{\bar{u}} dV = \frac{1}{2}\dot{q}^T \mathrm{M} \dot{q} \tag{15}$$

where

$$\bar{u} = Se, \quad \mathrm{M} = \mathrm{B}^T \mathrm{M}_{ff} \mathrm{B},$$

$$\mathrm{M}_{ff} = \int_V \rho S^T S dV \tag{16}$$

Using Lagrange's equation, the equations of motion of the beam are

$$\begin{bmatrix} m & 0 & 0 & -\frac{1}{2} ml\sin\theta \\ 0 & m & 0 & \frac{1}{2} ml\cos\theta \\ 0 & 0 & m & 0 \\ -\frac{1}{2} ml\sin\theta & \frac{1}{2} ml\cos\theta & 0 & \frac{1}{3} ml^2 \left(1 + \frac{4}{35}\cos^2\theta\right) \end{bmatrix} \cdot \begin{bmatrix} \ddot{R}_x \\ \ddot{R}_y \\ \ddot{R}_z \\ \ddot{\theta} \end{bmatrix} = \begin{bmatrix} Q_{ex} \\ Q_{ey} \\ Q_{ez} \\ Q_{e\theta} \end{bmatrix} + \begin{bmatrix} Q_{vx} \\ Q_{vy} \\ Q_{vz} \\ Q_{v\theta} \end{bmatrix} \tag{17}$$

and in the case of connected coordinates, the vector of centrifugal forces is written as

$$Q_v = \begin{bmatrix} \frac{1}{2} ml\dot{\theta}^2 \cos\theta \\ \frac{1}{2} ml\dot{\theta}^2 \sin\theta \\ 0 \\ -\frac{1}{2} m\dot{\theta}^2 \left(\frac{4l^2}{105} \sin 2\theta \right) \end{bmatrix} \qquad (18)$$

The errors in these equations are readily seen by comparing with the exact equations previously presented in this section.

Early Linearization. In the case of a simple rotation в about the Z axis, the global position vector of an arbitrary point on the beam element can be written as

$$u = \begin{bmatrix} u_1 \\ u_2 \\ u_3 \end{bmatrix} = \begin{bmatrix} x\cos\theta \\ x\sin\theta \\ 0 \end{bmatrix} \qquad (19)$$

The slope in this case is defined as

$$\frac{\partial u_2}{\partial x} = \sin\theta$$

Using this as definition of the slope in the vector of nodal coordinates, one has

$$e = \begin{bmatrix} 0 & 0 & 0 & 0 & 0 & \sin\theta & l\cos\theta & l\sin\theta & 0 & 0 & 0 & \sin\theta \end{bmatrix}^T$$

It can be demonstrated that the use of this vector and the element shape function leads to the exact rigid body inertia quantities and the exact equations of motion presented previously in this section. If the vector e, on the other hand, is linearized, one has

$$e = \begin{bmatrix} 0 & 0 & 0 & 0 & 0 & \theta & l & l\theta & 0 & 0 & 0 & \theta \end{bmatrix}^T$$

In order to see the error that might result in the equations of motion from the use of such an early linearization, we consider the case of a more general displacement as defined by the vector of generalized coordinates ***q***. In this case, the vector e is given by

$$e = \begin{bmatrix} R_x & R_y & R_z & 0 & 0 & \theta & R_x + l & R_y + l\theta & R_z & 0 & 0 & \theta \end{bmatrix}^T$$

and the time derivative of this vector is

$$\dot{e} = \mathrm{B}\dot{q}$$

where the vector ***q*** is defined , and the matrix B in this case of early linearization is

$$\mathrm{B} = \begin{bmatrix} 1 & 0 & 0 & 0 & 0 & 0 & 1 & 0 & 0 & 0 & 0 & 0 \\ 0 & 1 & 0 & 0 & 0 & 0 & 0 & 1 & 0 & 0 & 0 & 0 \\ 0 & 0 & 1 & 0 & 0 & 0 & 0 & 0 & 1 & 0 & 0 & 0 \\ 0 & 0 & 0 & 0 & 0 & 0 & 0 & l & 0 & 0 & 0 & 1 \end{bmatrix}^T \qquad (20)$$

The kinetic energy of the beam is

$$T = \frac{1}{2} \int_V \rho \dot{\bar{u}}^T \dot{\bar{u}} dV = \frac{1}{2} \dot{q}^T \mathrm{M} \dot{q} \qquad (21)$$

where M is the mass matrix of the rigid beam defined as

$$\mathrm{M} = \mathrm{B}^T \mathrm{M}_{ff} \mathrm{B} \qquad (22)$$

and M_{ff} is as defined in equation. The use of Lagrange’s Equation leads to the following matrix equation of motion in the case of early linearization.

$$\begin{bmatrix} m & 0 & 0 & 0 \\ 0 & m & 0 & \frac{1}{2} ml \\ 0 & 0 & m & 0 \\ 0 & \frac{1}{2} ml & 0 & \frac{1}{3} ml^2 \end{bmatrix} \cdot \begin{bmatrix} \ddot{R}_x \\ \ddot{R}_y \\ \ddot{R}_z \\ \ddot{\theta} \end{bmatrix} = \begin{bmatrix} Q_{ex} \\ Q_{ey} \\ Q_{ez} \\ Q_{e\theta} \end{bmatrix} + \begin{bmatrix} Q_{vx} \\ Q_{vy} \\ Q_{vz} \\ Q_{v\theta} \end{bmatrix} \qquad (23)$$

where the vector Q_v is defined as

$$Q_v = \begin{bmatrix} Q_{vx} \\ Q_{vy} \\ Q_{vz} \\ Q_{v\theta} \end{bmatrix} = \begin{bmatrix} 0 \\ 0 \\ 0 \\ 0 \end{bmatrix} \qquad (24)$$

Note that in the case of early linearization, the vector Q of centrifugal forces is identically equal to zero. Observe also the error in the definition of the moments of mass in the mass matrix.

Conclusion

In this paper, two conceptually different finite element methods that lead to exact modeling of the spatial rigid body inertia of beams are discussed. The first method is used when infinitesimal rotations are used as nodal coordinates for the finite element. This method allows the use of the classical finite element formulations in the flexible multibody simulations. In the second method, absolute displacements and slopes are used as nodal coordinates, instead of using infinitesimal rotations. This method has a potential in solving large deformation problems in varieties of flexible multibody applications.

In the flexible multibody formulations of elements that have infinitesimal rotations as coordinates, an intermediate element coordinate system is introduced. This coordinate system does not follow the element deformation, and is used only to define the locations of the nodes in the undeformed state, thus preserving the exactness of the rigid body inertia. This coordinate system is rigidly attached to the structure (not the element) coordinate system. The position of an arbitrary point on the element can be defined in the element coordinate system as $u = S(e_0 + e_f)$, where S is the element shape function, e_0 is the vector of nodal locations in the undeformed state (This is not the vector of rigid body displacements), and e_f the vector of nodal displacements defined in the intermediate element coordinate system. The preceding equation can be used to develop a nonlinear formulation that leads to an exact model for the spatial rigid body inertia.

The concept of the intermediate element coordinate system has been successfully used in the analysis of small deformations in many flexible multibody applications. The limitations of this approach in the analysis of large deformations stem from the fact that infinitesimal rotations are used as nodal coordinates. In this case beam elements are not considered as isoparametric elements. It is demonstrated in this paper that beam elements can be considered as isoparametric elements if absolute slopes instead of infinitesimal rotations, are used as nodal coordinates.

References

1. Agrawal, O. P. Dynamic Analysis of Multibody System Using Component Modes // Computers and Structures.– 2015. – Vol. 121. No 6. – P. 1303-1310.
2. Bayliss, A., and Isaacson, E. How to Make Your Algorithm Conservative // Not. Amer. Math. Soc. – 2015. – P. 594-.595.
3. Belytshchko, T., and Hsieh, B. J. Nonlinear Transient Finite Element Analysis with Convected Coordinates // International Journal for Numerical Methods in Engineering. –2003. – Vol. 47. – P. 255-271.
4. Belytshchko, T., and Schoerberle, D. F. On the Unconditional Stability of an Implicit algorithm for Nonlinear Structural Dynamics // ASME Journal of Applied Mechanics. – 2010. – Vol. 142, No 4. – P. 865-869.
5. Cardona, A., and Geradin, M. A Beam Finite Element Non-linear Theory with Finite Rotations // International Journal for Numerical Methods in Engineering. – 2008. – Vol. 126. – P. 2403-2438.
6. Flanagan, D. P., and Taylor, L. M. An Accurate Numerical Algorithm for Stress Integration with Finite Rotations // Computer Methods in Applied Mechanics and Engineering. – 2007. – Vol. 62. – P. 305-320.
7. Hughes, T. J., and Winget, J. Finite Rotation Effects in Numerical Integration of Rate Constitutive Equations Arising in Large-Deformation Analysis // International Journal for Numerical Methods in Engineering.– 2006. – Vol. 15. – No 12. – P. 1862-1867.
8. LaBudde, R. A., and Greenspan, D. Energy and Momentum Conserving Methods of Arbitrary Order for the Numerical Integration of Equations of Motion, Part I // Numer. Math. – 2006. – Vol. 25. – P. 323-346.

International Journal of Mathematics and Physics 7, №2, 48 (2016)

UDC 66.045.54

*Salimhanova S.A., Makashev P.E., Omarova T.P., Kalmenova B.G.

Faculty of Mechanics and Mathematics,
al-Farabi Kazakh National University, Almaty, Kazakhstan
*e-mail: asemsalimhanova@gmail.com

Calculation of performance of ventilatory cooling towers

Abstract. This article provides aerodynamic and thermal calculation of ventilatory cooling towers depending on atmospheric conditions (temperature, humidity, pressure) of an area. The features of modern water circulation systems of cooling the equipment via ventilatory coolers are considered. The factors that influence the stability, reliability and efficiency of the cooling towers are analyzed. The formulas for determining the properties of moist air are presented, and methods of engineering calculations of a ventilatory cooling tower based on the experimental data in the field of parameters of atmospheric calculations for aerodynamic and climatic conditions are presented. Based on thesecalculations the software complex with the usable interface developed.

Key words: cooling tower, calculated dependencies, relative humidity, water catchers.

Introduction

The ventilatory cooling tower is the device intended for dispersion in atmospheric air of a flow of heat received by the cooling water in cooling devices. In the cooling tower there is a direct contact of the cooled water with atmospheric air.

Warm water gets to the main collector of a water distributor. Further there is transport through system of pipes to nozzles. Nozzles spray water streams on a sprinkler, creating the water screen with the big surface of contact. The water which is coming off bottom edges of elements of a drain of a sprinkler falls down in the form of a rain in the pallet which is under the cooling tower from where it is forced back in the cooling device.

Process of chilling of water takes place, in the main measure, due to evaporation by the proceeding current of air of a small part of a stream of the cooled water (weight transport), with use of heat of phase transition (warmth of evaporation) received from a water stream and also – in a smaller measure – due to convective heat exchange between water and air (heat transport).

The counterflow current of air in cooling towers, is caused by exhaust influence of the axial ventilator which productivity is picked up to the required cooling parameters. The fan is installed in the case, on overlapping of a compartment of the cooling tower. Air is involvedin a compartment through the entrance windows equipped with blinds which protect from hit of solid bodies from the environment, for example leaves, and also from spraying of the cooled water out of the cooling tower. Further the involved air passes through the rain zone under sprinklers, through irrigative filling, in the zone of spraying of water over a sprinkler, and further there is a capture of drops by the water catcher which minimizes loss of water due to stealing of drops. The warmed-up and watered air proceeds via the fan, then, through the top section of the cage of the fan it is blown outside to the environment.

Extent of cooling of water in the wet cooling tower depends on temperature of the thermometer of the damp air involved outside, the air volume (fan productivity) and technical solutions of the cooling tower. Cooling towers are designed for obtaining the expected effect of cooling in the most adverse conditions (high temperature and humidity of air) and taking into account need of a conclusion of the maximum quantity of heat from water.

Features of process of chilling of water in cooling towers

Chilling of water in cooling towers is performed by transfer of heat to atmospheric air due to superficial evaporation of water and hat transfer contact (heat conductivity and convection). Heat can be taken away from water and due to the radiation. However the amount of heat transferred by radiation so isn't enough that in case of creation of thermal balance of the cooling tower neglect it.

During the most part of year the prevailing role is played by superficial evaporation. In the summer during a heat about 90% and more heat, given by water are the share of evaporation. In the winter heat transfer with contact increases up to 50%, and in the coldest time up to 70%, against 10-20% and less during the summer period. "Driving force" of process of evaporation of water in the cooling tower is the difference of partial vapor pressure at a water surface and in a kernel of an air flow. In case of heat transfer contact by such driving force is the difference of water temperatures and air. In the cooling tower the atmospheric air, which is damp, is arrived as it always contains a certain amount of the vapors of water which are usually in a superheated condition. For thermal calculations of cooling towers with sufficient degree of accuracy is accepted that damp air, which can be considered as mix of dry air and water vapor, submits to laws of mix of ideal gases. Dry air and steam occupy the same amount as all mix.

The key parameters characterizing a condition of damp air are pressure, temperature, density, moisture content, relative humidity, an enthalpy.

Under Dalton's law pressure of damp air corresponding to the barometric pressure P_b is equal to the amount of partial pressure of dry air of$P_{a,d}$ and water vapor of P_v:

$$P_b = P_{a.d} + P_v \quad (1)$$

Partial pressure of water vapor in the cooling tower isn't enough compared with very slightly changing barometric pressure, therefore in further conclusions of estimated dependences it is accepted

$$P_{a.d} = P_b - P_v = Const \quad (2)$$

Partial pressure of dry air and steam are defined from Mendeleyev-Clapeyron's equation:

$$P_{a.d}/\gamma_{a.d} = R_{a.d} T \cdot 10^{-4}\,; \quad P_v/\gamma_v = R_v T \cdot 10^{-4} \quad (3)$$

where T – temperature, K; $\gamma_{a.d}$- density of dry air, kg/m3; γ_v – density of vapors of water, kg/m3.

Density of damp air is equal to the sum of density of dry air and steam:

$$\gamma_{damp} = \gamma_{a.d} + \gamma_v = \frac{P_b - \phi P_v''}{R_{a.d}(\vartheta + 273{,}2)} + \phi \gamma_v'' \quad (4)$$

It is useful to note that density of damp air goes down with reduction of pressure, with temperature increase and relative humidity.

Communication between key parameters of damp air for convenience of practical calculations and presentation can be presented in a graphic form. Thei-d-charts, representing graphic functional dependences of enthalpies on moisture contents with the put lines of constant values of temperatures and relative humidity, have the widest extension. For improvement of expansion of lines φ = Const the corner between axes of coordinates is accepted equal 135°. Charts are constructed for certain barometric pressure 500, 740, 1000 mm of mercuryetc. A theoretical limit of cooling of water by air is air temperature on the watered thermometer ф. It is reached by moistening of air without additional removal or supply of heat to saturation condition (φ = 100%), i.e. at adiabatic evaporation. Oni-d-chart value ф is defined by a point of intersection line i = Const passing through the point characterizing a condition of damp air with the line φ = 100%.Consequently by value ф unambiguously it is possible to determine values of an enthalpy and moisture content of air.

Calculation of ventilatory cooling tower

The cooling tower represents the heatexchange device in which the heat carrier – water transfers warmly to coolant – air by direct contact. For ensuring necessary surface area of contact the cooling tower is equipped with a special element – the irrigating device (sprinkler). The significant contribution to development of methods of calculation of cooling towers is made by F. Merkel, B. V. Proskuryakov, L. D. Berman, I. Liechtenstein and other authors. L. D. Berman's monograph till today is the reference book of the engineering employees who are engaged in designing, operation and a research of cooling agents of turnover water. The widest extension and general recognition in the world gained Merkel's method. The detailed statement and discussion of a method of Merkel is published in a number of books and numerous articles. The modern option of a conclusion of the equations describing process of a heat mass exchange in counterflow cooling towers, in relation to practical calculations of these constructions taking into account the assumptions accepted by Merkel, is given in this handbook in summary form.

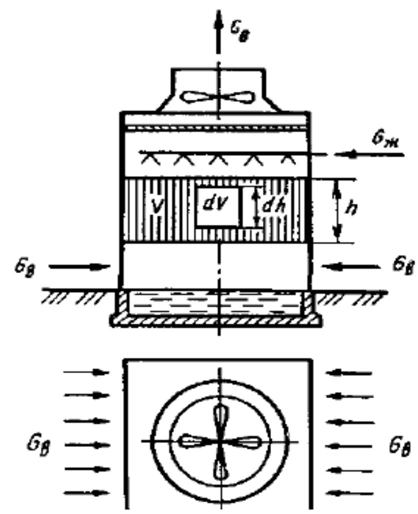

Figure 1 – Scheme of the ventilator cooling tower

In the Figure1 the scheme of the ventilator cooling tower is shown. The balance of the heat, given in the cooling tower by water and received by air,is presented in the following form:

$$Q = c_l\left[\mathrm{G}_1(\mathrm{t}_1 - \mathrm{t}_2) + G_\mathrm{e} t_2\right] = \mathrm{G}_{\mathrm{m.c}}(i_2 - i_1) \quad (5)$$

The material balance (balance of moisture) is defined by equality between amount of the evaporated liquid and an increment of moisture content of air:

$$G_e = G_{m.c}(x_2 - x_1) \quad (6)$$

In case of thermal calculation of cooling towers expenses and initial parameters of water and air are usually set, and the final parameters t2, i2, h2 remain unknown. It is obvious that two equations (5) and (6) for their determination aren't enough. Therefore it is necessary to address the equations describing process of a heatmass exchange between water and air in a cooling tower sprinkler. They can be constituted only in a differential form, as the entering parameters change on the way of movement of water in a sprinkler all the time.

For elementary amount of a sprinkler of dV with a single area and height of dh (fig. 1) we have

$$dQ = \alpha(t - \vartheta)dV + i_v'' \mathrm{dG}_1 \quad (7)$$

where $\mathrm{i}_\mathrm{v}'' = c_l \mathrm{t} + r$ - steam enthalpy at water temperature t_l.

Determination of an average difference of enthalpies of air and sizes A and m

Calculations of cooling towers and handling of results of their researches on the given formulas require big costs of time and use of iterative methods. Therefore it is reasonable to make such calculations on special computers, for handling of results of measurements in case of determination of sizes A and m. For determination of the cooling capability of a sprinkler the following parameters are measured: speed of movement of air in the free section of the cooling tower over a sprinkler with, m/s; density of irrigation of q_l, m3 / (m·h); temperature of hot water at the entrance to the cooling tower t1, °C; temperature of chilled water at the exit from the cooling tower t2, °C; barometric pressure of P_b, mm of mercury; air temperature on dry ϑ and wet-bulb thermometersτ, °C. Besides, the area of the sprinkler, $m^2$and its height *h*, m is measured.

Basic data

The estimated dependences reflecting or determining operation of the cooling tower include the following sizes: water consumption; air consumption; temperatures of the entering and coming out water; estimated atmospheric parameters (climatic conditions) determining an enthalpy and density of the entering air, and also the limit of chilling of water in the cooling tower; technical characteristics on a sprinkler; area of irrigation of a sprinkler (cooling tower).

Depending on a calculation task one of the specified sizes can be required, and the others are set. At the same time climatic conditions (calculated atmospheric parameters) shall be always set.

The water consumption (hydraulic loading G_l) is usually set by technologists of production proceeding from heattechnical calculations of the equipment cooled by water – condensers, refrigerators, compressors, various technological devices, metallurgical aggregates, etc.

The air consumption (estimated air supply by the fan) is determined by aerodynamic calculation of the cooling tower.

Temperatures of the entering t1 and the leaving water t2 are established by technologists of production based on heattechnical calculations taking into account characteristics of the cooled equipment. It must be kept in mind that temperatures of turnover water, especially t2, can have very significant effect on parameters of engineering procedure, the sizes of cooling towers, diameters of pipes, displacement of pumps and performance of other equipment, and also on electricity consumption. Therefore it is reasonable to determine t2, and also consumption of the cooled water G_l by technical and economic calculations of joint operation of all constructions of a water turnover cycle – processing equipment, cooling towers, a circulating pumping setup and installations for cleaning and water preparation. However these calculations aren't always feasible. In this case when designing it is recommended to accept the calculated value of t2 proceeding from the condition that the difference t_2-τwas at least 5 °C. The lowest values of a difference t2 – τ can be accepted only in that case when it is dictated by strict requirements of production. For economical and practical reasons in all cases the difference t_2- τ should not be less than 2 °C.

Calculated parameters of the atmospheric (entering) air are set according to data of meteoconditions. Technical characteristics of the sprinkler (A, m, $\zeta_{c.o}$ and K_{sp}) are accepted by results of its researches. The area of the sprinkler (the cooling tower, section) is determined by calculation, but can be is set (depending on purpose of calculation).

Calculation methods

Technological calculations of cooling towers need to be made in case of development of new constructions, matching and conversion of projects (standard or other ready), for a binding to conditions of the specific entity, in case of job evaluation of the operating cooling tower in use and reconstruction.

Three types of calculations are most often carried out: determination of temperature of water cooled on the cooling tower t2, density of irrigation and the area of irrigation of the cooling tower F. The specified required parameters are from the joint decision (8) and (9). Depending on purpose of calculation the structure of basic data and the applied calculation formula change.

Determination of t is made by the formula

$$t_2 = t_1 - A\lambda^m hK\Delta i_{aver} / c_l \qquad (8)$$

The area of irrigation of section or the cooling tower, climatic conditions (ϑ,τ, φ, P_b), technical and constructive characteristics on a sprinkler are set (A, m, ζ_{sp}, K_{sp}, h,q_l).

Calculation of q_l is made by the formula

$$q_l = \beta_{xv} / (A\lambda^m) \qquad (9)$$

Air parameters when calculating cooling towers

Cooling towers are calculated usually on adverse atmospheric conditions for work in summer months of year. However it is inexpedient to conduct calculation on the most high temperatures and humidity of external air as they can be observed within a year only very shortly. The higher estimated temperatures and humidity of atmospheric air, the larger sizes the cooling tower is required and respectively the higher costs for its construction. At the same time too low estimated temperatures and humidity of air can lead to the fact that the actual water temperatures at the exit from the cooling tower during the long period in hot season will exceed the estimated temperature t2. It will entail undercooling of a production product in the heatexchange equipment. Therefore, in case of the choice of calculated parameters of external air it is necessary to take into account admissible temperature increase water t2 over estimated from conditions of engineering procedure of production, but to limit the period of this increase.

When calculating cooling towers it is recommended to proceed from average daily values of temperature and humidity of atmospheric air in summer months on long-term observations. As estimated values usually are accepted such values,which exceed average daily values within no more than 5 days in a year, and in case of less strict requirements – within no more than 10 days in a year.

For determination of calculated parameters of external air it is possible to use the available tabular data or curves of duration of average daily temperatures standing and humidity of atmospheric air for the construction area of the cooling tower according to long-term observations (not less than in 5-10 years). In the absence of ready data it is possible to make previously for constructing of duration of standing of temperatures of external air tables of average daily temperatures distribution and on zones, for example, through 1 °C and average daily humidity on zones through 5%. Further, conforming requirements of technological process, it is necessary to set number of days in a year *n* during which excess of the actual values is admissible, both over settlement and by curves to determine settlement temperatures and humidity of atmospheric air.

Average daily temperatures and humidity are calculated according to evenly even measurements of these sizes during the day: in 9, 12, 15 and 18 h. For the purpose of saving of time when handling materials of long-term observations usually are built curves of duration of standing ϑ and τ (or φ) only for the summer period (~ 100 days) and proceeding from this security are determine, %. Sites of such curves in the limits, that are used for the choice of estimated parameters of air, can be considered with sufficient degree of accuracy showing the standing's duration of the corresponding temperatures during the whole year, as in the rest of the time of year these temperatures don't repeat at all or are observed very shortly.

The stated method of determination of estimated parameters of atmospheric air requires big costs of time and work. Besides, basic data aren't published and they should be received in hydrometeorological service.

Air temperature according to moistened thermometer τ is a theoretical limit of chilling of water in the cooling tower. Considering that with approach of settlement water temperature to a theoretical limit of chilling τ the larger size of the cooling tower will be required, in case of their designing it is recommended to accept the settlement temperature of t2- τ proceeding from a condition: the difference t2 – τ shall be at least 4 °C for ventilatorycooling towers and 8 °C for tower. Lower values of differences t2 - τ are accepted only when it is dictated by requirements of engineering procedure of production.

With approach of t2 to a chilling limit the required cooling agent sizes strongly grow. Quite often, however, in case of setting of basic data for specific production put too low ("with an inventory") temperature of chilled water t2, reducing at the same time the difference t2 - τ . For cooling towers this reduction from 10 to 5 °C results in need of decrease in the water of density of irrigation $q_ж$ which is required for chilling by 2-2,2 times. Performance of ventilatorycooling towers under existing conditions decreases, as requires for increase in their area in order to chill the specified amount of water. Therefore it is not recommended accept too small value t2 - τ without special need. Conditions, when t2- $\tau \approx$At, are considered as optimum conditions for operation of vaporizing cooling towers.

Influence of barometric pressure at its usual values fluctuating within about 720-760 mm of mercury, it is rather small, and it can be not taken into account at practical calculations of cooling towers. However for mountain areas where barometric pressure can go down to values of 600-650 mm of mercury, it is already necessary to consider its influence. Decrease in barometric pressure leads, under other invariable conditions, to some decrease in intensity of vaporizing cooling, but in case of ventilatorycooling towers it is compensated and is even blocked by reduction of resistance of the cooling tower and increase in speed of air owing to reduction of its density. In cooling towers the reduction of a difference of density of the arriving and leaving air involving reduction of driving force , appears more considerable than reduction of absolute values of air density , and at decrease in barometric pressure cooling effect of the cooling tower decreases a little.

Determination of air consumption in ventilatorycooling towers

The task of determination of air consumption can arise during designing and binding of cooling towers, and also during operation for work on reconstruction. For this purpose aerodynamic calculation of the cooling tower are made. For its accomplishment it is necessary to know type and design of the cooling tower, brand of the fan, the main sizes of the cooling tower (section), its entrance windows, air distributor, sprinkler, water distributor and water catcher. It is also useful to have the factory graphical characteristic of the fan representing dependence between air supply, the created pressure, capacity and efficiency of this fan.

In this section the advanced method of calculation of supply of cooling towers fan is stated. The formula for determination of complete aerodynamic resistance of the cooling tower is corrected. The sizes entering it are brought into accord with really significant and measured sizes.

Availability of zones of turbulences on the areas of cooling tower irrigation and their influence on supply of the fan is considered. Factory graphical characteristics of cooling towers fans are presented analytically in the form convenient for calculations on PC. Examples of calculations of air expenses in standard cooling towers are given.

Materials of natural and laboratory researches allow express the general resistance of section of the cooling tower as follows:

$$P_R = (P_{ECT} + P_{SP} + P_{WD} + P_{WC} + P_{AA})\Phi + P_A, \quad (10)$$

where resistance of elements of the cooling tower are designated: P_{ECT} - an entrance to the cooling tower, including the air distributor, taking into account turn of air stream in the sprinkler; P_{SP} – a sprinkler; P_{WD} – water distributor; P_{WC} – water catcher; P_{AA} – approach of air to the fan on the way from the water catcher to the feedwell; P_A – resistance added when giving on the water cooling tower. This resistance depends on hydraulic loading, type of a sprinkler, water distributor and the sizes of section; Φ – the coefficient considering influence of the section form in the plan for the general resistance of the cooling tower. Calculation of resistance of section, kg/ m^2, is made by the formula

$$P_R = \frac{\gamma\omega^2}{2g}\zeta_r, \qquad (11)$$

where ω – the speed of the movement of air in the free cooling tower section , m/s; γ – density of air, kg/m3, is accepted the same as specified in the characteristic of the fan, is usually equal to 1,2 kg/m3; ζ_r – the cooling tower section resistance coefficient determined by the formula

$$\begin{gathered}\zeta_r = \sum\zeta = (\zeta_{ECT} + \zeta_{SP}h + \zeta_{WD} + \\ +\zeta_{WC} + \zeta_{AA})\Phi + \zeta_A,\end{gathered} \qquad (12)$$

where coefficients of resistance ζ are designated by analogy with standard projects. All of them are dimensionless, except for coefficient ζ_{SP} which as it is accepted, has dimension 1/m; h – height of a sprinkler, m.

Ventilatory installations

One of necessary conditions of effective operation of cooling towers is the right choice of economic fans.

For cooling towers the special axial exhausting or delivery fans are usually used. In case of use of exhausting fans more uniform air distribution on cross section in the cooling tower bottom is provided, than when using delivery, as the input of air and its turn at right angle for movement up is performed at smaller speeds. Reduction in the rate of air movement in case of an entrance is reached due to implementation of entrance windows of big section from all or from two sides of the cooling tower. Uniformity of air distribution is an important factor in receipt of cooling effect of the cooling tower.

In case of the exhausting fans there are less opportunities to cooling tower, in its entrance exhausting fans throw out air with a speed of 6-10 m/s up, and (by observations of operation of the operating cooling towers) the vertical direction of a flow of damp air after fans remains on the site 10-12 m high that almost excludes a possibility of air recirculation. In case of delivery fans air goes out of the cooling tower with a speed about 1,7-2,5 m/s, and comparably light breeze can lead to blowing of outgoing warm damp air and to exhausting by fan that leads to sharp deterioration in cooling capability and requires increase in the sizes of the cooling tower.

In fig. 2 the scheme of the fan's arrangement in the cooling tower 77-Z-001 is provided.

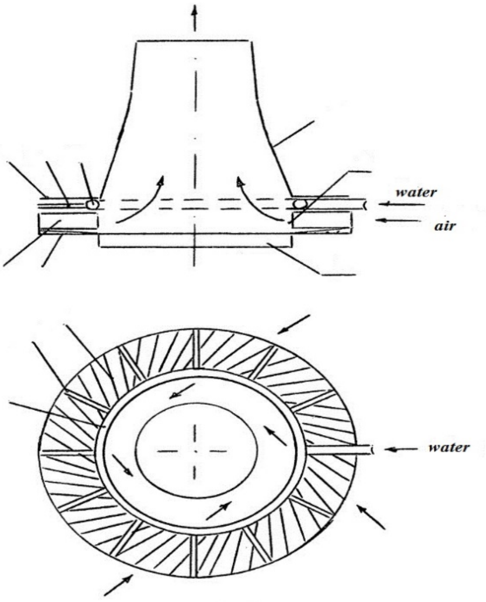

Figure 2 – Scheme of arrangement of the cooling tower fan 77-Z-001

Each section of the cooling tower 77-Z-001 is equipped with the axial fan. Its blades of an aerodynamic form are designed taking into account assurance of silent work. The step of blades is regulated manually and they are easily established in a nave by means of U-of figurative bolts and flanges depending on the chosen manufacturer. The fan has the drive from reducers with the double reduction and helical conic transfer located perpendicular to the fan axis. Reducers are established at the center in the fan case, and the nave of the fan is mounted directly on vertically located low-speed output shaft. Shaft of floating type are used. These shafts are made of composite material and established in flexible couplings from stainless steel. Electric motors are established outside of a ventilatory tower on a vertical platform.

Conclusion

Ventilatorycooling towers are the central and major link of a technological chain of heat removal in water turnover systems of the entities as by evaporation and heat exchange with atmospheric air, they allow to reduce water temperature to required values. It is also important to know that, when changing the speed of rotation of the cooling tower fan, it is possible to regulate output parameters of water recirculation depending on seasonal, meteorological and technological changes of a large number of factors.

This scientific article considers calculation of the ventilatorycooling tower and its installation, often used 3 types of calculation: determination of temperature of chilled water in the cooling tower, the irrigation density size, calculation of the area of the cooling tower sprinkler and information about 77-z-001 type of the ventilatorycooling tower. At present studying methods of determination of calculation algorithms of the ventilatorycooling tower, the program in the C# language which determines its performance is developed. In the developed program by means of the database it is possible to obtain full information on amount evaporation during water chilling, aerodynamic calculation, parameters of the air when calculating the cooling tower, air consumption, water consumption, water temperature during the delivery and pouring out, parameters of atmospheric estimation with climatic conditions, technological parameters of the sprinkler in the form of the table.

References

1. Ponomarenko, V.S. Gradirni promyshlennyh i jenergeticheskih predprijatij: spravochnoe posobie // V.S. Ponomarenko Ju.I. Aref'ev; pod red. V.S. Ponomarenko. – M. Jenergotomizdat. 1998. – P. 376.

2. Vaganov, A.A. Teplomassoobmennye ispytanija setchatoj nasadki / A.A. Vaganov, A.S. Timonin // Himicheskoe i neftegazovoe mashinostroenie. – 2010. – No 11. – P. 32-36.

3. Vaganov, A.A. Issledovanie teplomasso obmennyh harakteristik setchatoj nasadki / A.A. Vaganov, A. S. Timo-nin // Bezopasnost' v tehnosfere. – 2010. – No 2. – P. 37-42.

4. Merencov, N.A. Jeksperimental'naja ustanovka dlja issledovanija teplomassoobmennyh processov v nasadoch-nyhustroj stvahgradiren / N.A. Merencov, V.A. Balashov, A.B. Golovanchikov, Ja.A. Orljankina // Izvestija VolgGTU: mezhvuz. sb. nauch. st. № 1 / VolgGTU. – Volgograd, 2012. – (Serija «Reologija, processy i apparaty himicheskoj tehnologii»; vyp. 5). – P. 78-80.

5. Golovanchikov, A.B. Modelirovanie gidromehanicheskih i teplo- i massoobmennyh processov v ventiljatornoj gradirne s kapel'nym orosheniem i provolochnoj nasadkoj / A.B. Golovanchikov, N.A. Merencov, V.A. Balashov, Ja.A. Orljankina // Izvestija VolgGTU: mezhvuz. sb. nauch. st. № 10(97) / VolgGTU. – Volgograd, 2012. – (Serija «Aktual'nye problemy upravlenija, vychislitel'noj tehniki i informatiki v tehnicheskih sistemah»; vyp. 14). – P . 22-28.

6. P. m. 117317 RF, MPK V 01 I 19/32. Nasadka dlja massoobmennogo apparata / A.B. Golovanchikov, S.B. Vo-rotneva, N.A. Merencov, N.A. Dul'kina, O.A. Zalipaeva, A.P. Sham'janova; VolgGTU. – 2012.

7. Merencov, N.A. Avtonomnye sistemy oborotnogo vodosnabzhenija dlja malotonnazhnyh himicheskih proizvodstv / N.A. Merencov, A.B. Golovanchikov, V.A. Balashov // Izvestija VolgGTU: mezhvuz. sb. nauch. st. № 1 / VolgGTU. – Volgograd, 2011. – (Serija «Reologija, processy i apparaty himicheskoj tehnologii»; vyp. 4). – P. 102-104.

8. Merencov, N. A. Isparitel'noe ohlazhdenie kapel' zhidkosti v vozdushnompotoke / N.A. Merencov, V. A. Balashov, A. B. Golovanchikov, Ja. A. Orljankina // Izvestija VolgGTU: mezhvuz. sb. nauch. st. № 1 / VolgGTU. – Volgograd, 2012. – (Serija «Reologija, processy i apparaty himicheskoj tehnologii»; vyp. 5). – P. 62-65.

International Journal of Mathematics and Physics 7, №2, 55 (2016)

UDC 519.863

*Zhumagulova Sh.P., Turganbayeva A.R.

Faculty of Mechanics and Mathematics,
al-Farabi Kazakh National University, Almaty, Kazakhstan
*e-mail: sholpana_1993_kz@mail.ru

The models and algorithms for interaction of software agents

Abstract. In this paper software agents' communication models and algorithms in the virtual business environmenthave been proposed. They allow to reduce response time on any changes of environment imitating the innovation field due to increase of data exchange between the agents and reduction of general network load. Two mechanisms for conversion of inter-node agent communications to intra-node agent communications and dynamic agent distribution have been represented. Various implementation approaches for agent communication and interaction mechanisms have been considered. Methods for effectiveness increase of data exchange between mobile agents in the distributed system for information support of innovations have been proposed. Data exchange mechanisms between software agents in the virtual business environment based on agent address structure extension and using of middle-agents brokering and matchmaking services have been minutely described.

Key words: multi-agent system, agent communication models, data exchange algorithms, informationsupport of innovations.

Introduction

This article seems relevant to the task of creating a completely decentralized peer-to-peer systems for information support of innovations that allow flexible integration of existing and emerging information resources on innovation in a logically unified whole, thereby creating a single information space for effective interaction of subjects of innovation activities. Effective implementation technology of distributed information systems of this class is the technology of mobile program agents. Such systems shall provide not only distributed access to information, but also decentralized storage and data processing, to solve problems of technological and semantic heterogeneity of information resources a prototype of system of information support of innovative activities in the region – multi-agent system of integration of distributed information resources of innovations and appropriate information technology.

The article discusses the models and mechanisms for software agents' interaction of subjects of innovation activities in virtual business environment of innovations development, allowing reducing the agents' response time to environment changes that imitates the innovation field, by increasing the intensity of information exchange between the agents and reducing the overall load on the network. Methods of increase in efficiency of information exchange between mobile agents in distributed multi-agent system for information support of innovations are offered.

Problem definition

The technology of multi-agent systems (MAS) is a new paradigm in information technology, focused on sharing scientific and technological achievements and benefits of the ideas and methods of artificial intelligence (AI), modern local and global computer networks, distributed databases and distributed computing, hardware and software support means of the theory of distribution and openness.

Agent-oriented approach is widely used in various fields requiring the solution of complex distributed tasks, such as combined product design, reengineering of business processes and building a virtual enterprise, simulation of integrated production systems and electronic commerce, work organization of robots teams and distributed (combined) development of computer programs.

In case of internodal interaction of software agents in a virtual environment there is number of problems connected with increasing network load, decrease in intensity of information exchange between agents depending on speed and bandwidth of communication channels of the network, increase in messages delivery time and search time of required agent for interaction. As the solution for these problems the method is proposed which is based on splitting a common information space in which agents function into virtual platforms (the platform represents some separate network node) and moving intensively interacting agents to these platforms for the purpose of association of them in coalition. The proposed solution is realized in a form of two mutually complementing mechanisms (algorithms) of software agents' interaction: localization mechanism of inter-agent interactions (transformation of internodal agents' interaction into interaction in one common node) and mechanism of dynamic distribution of agents (distribution of loading between system nodes).

Mechanism of localization of inter-agent interactions

The mechanism of localization of inter-agent interactions consists of four phases: monitoring phase, phase of agents' distribution, phase of interaction (negotiation) and phase of migration of agents.

1.Monitoring phase. The Manager of Distribution of Agents (MDA) estimates intensity of internodal and intranodal communications of system agents by means of the system monitor and the manager of messages. MDA also uses information both on the agent-sender of each message, and on the node of the agent-receiver. MDA periodically calculates communication dependences $C_{ij}(t)$ in timepoint $t \in T = [t_1; t_2]$ between the agent i and the agents of j-node by the formula:

$$C_{ij} = \alpha(M_{ij}(t) / \sum_k M_{ik}(t)) + (1-\alpha)C_{ij}(t-1),$$

where:

M_{ij}(t) – number of messages sent by the agent i to the agents of j-node during period of $T=[t_1;t_2]$,

α – coefficient specifying the comparative importance of the new information in relation to outdated one and which is used for ignoring of temporary intensive interaction with the agents on a certain agent's platform. C_{ij}(t-1) is understood as value of the same communication dependence in the previous interval of time.

2. Phase of agents distribution. After a certain number of repetitions of monitoring phase MDA calculates a coefficient of communication dependence between the current node of the agent n and all the other nodes of the system. The coefficient of communication dependence R_{ij} between the agent i and the agents of j-node is determined by the formula:

$$R_{ij} = C_{ij} / C_{in}, j \neq n$$

When maximum value of coefficient of communication dependence of the agent is more than predetermined threshold θ, MDA of the current node includes the considered agent in the group of agents located in remote node of the system:

$$k = \arg_j \max(R_{ij}) \wedge (R_{ik} > \theta) \rightarrow \alpha_i \in G_k,$$

where: α_i is the agent i, $G_k k$ indicates a group of agents, and under $\arg_j$ hereinafter refers to an operation that returns the value of j, in which the ratio of communication depending R_{ij} takes the maximum value.

3. Interaction phase. Before moving the allocated group of the agents from node P1 to accepting node P2 the MDA of the node P1 interacts with MDA of the node P2. MDA of the node P2 veryfies current of the agents is carried out on the basis of communication dependences between the groups of the agents and the nodes of the system. Communication dependence D_{ij} between i-group of the agents and j-node of the system is defined on the basis of summation of communication dependences between all members of the group of the agents and the node of the system:

$$D_{ij}(t) = \sum_{k \in A_j} C_{kj}(t),$$

where:Ai is a set of indexes of all agents belonging to i-group of the agents, and C_{kj}(t) – communication dependence between k-agent and j-node in timepoint t. Group of the agents i^* which has the smallest dependence on the current node is selected by the following rule:

$$i^* = \arg_i \max(\sum_{j, j \neq n} D_{ij} / D_{in}),$$

where: n – number of the current node (agent platform).

The accepting j^* – agent platform of selected i-group of the agents is defined on the basis of communication dependence between i-group of the agents and j^* – node of the system as follows:

$$j^* = \arg_j \max(D_{ij}), j \neq n,$$

where: n – number of the current node.

Algorithms of information exchange between mobile agents

To improve the efficiency of distributed data processing by the agents and reduce the total amount of data transferred over the network, the existing algorithms of information exchange between mobile agents presented in (*Alouf et al.*, 2002), (*Stefano, Santoro*, 2002) were modified:

FMP (forwarding-based message passing – algorithm of readdressing of messages), FLAMP (forwarding and location address-based message passing – algorithm of readdressing and definition of the address of location of the agent), FLCMP (forwarding and location cache-based message passing – algorithm of readdressing and local caching for determination of location of the agent), ALMP (agent locating-based message passing – algorithm of localized exchange of messages between the agents) and ALLCMP (agent locating and location cache-based message passing – algorithm of localization and local caching for organization of exchange of messages between the agents). The proposed algorithms perform messages transfer directly from agents-senders to agents-receivers, minimizing a total quantity of hops at message transfer over the network. Results of experiments show that in case of intensive interaction of the agents FLCMP and ALLCMP mechanisms are more effective in respect of their performance than the others. However their efficiency significantly depends on extent of inter-agent interaction in the course of migrating of agents and groups of agents between the system nodes.

The mechanism of agent's communication based on use of intermediary agents

In open multi-agent systems characterized by high dynamism (new agents can appear and disappear at any moment and new nodes can be connected), each separate agent can't possess full information on all other agents in single information and communication space. In such environment of joint function the network services of intermediary agents (broker and entrepreneur services) are very effective for search of potential agents for interaction. Software agents can find other agents' names (by means of entrepreneur services) or send messages to other agents (by means of broker services), using their attributes such as methods, operating modes, characteristics or pseudonyms instead of their real names. For registration of agents' names in distributed environment the dedicated server of agents' names can be used.

Mediatorial functions of the agent are implemented in the form of separate component in his architecture, or can be realized in the form of independent customized application called the intermediary agent. Intermediary interaction between the agents includes either brokers, or entrepreneurs.

Brokers send the messages set by agents-senders to the network nodes with agents-receivers, whereas entrepreneurs only provide information on the agent-receiver's location requested by the agents intending to send messages. That is the final message is delivered by brokers to the agent-receiver, whereas entrepreneurs only help agents-senders to deliver messages to agents-receivers providing information on their location. Considering the number of hops at message transfer, we may draw a conclusion that broker services are more effective than entrepreneur ones as broker services usually require two hops at message transfer, and entrepreneur services – three.

With the use of common memory space called data fragments space which is run by the intermediary agent, the agents can register their attributes together with their names in this space, and also can communicate with each other with the help of information on agents' attributes taken from this data space. The Linda-model is the cornerstone of the most of developed intermediary agents (Carreiro, Gelernter, 1989). The structure of actor model of data fragments space (AMDF) is shown in fig.

The model allows software agents to use intermediary agents and the services they provide for search of "joint activity" agents, and it makes the basis of method of use of intermediary agents and their functions. At the same time the intermediary agent not only governs data fragments, but can also use both his own algorithms of search of "joint activity" agents, and algorithms provided by agents-initiators. This is the main difference of proposed method of use of intermediary agents and their functions in comparison with existing ways.

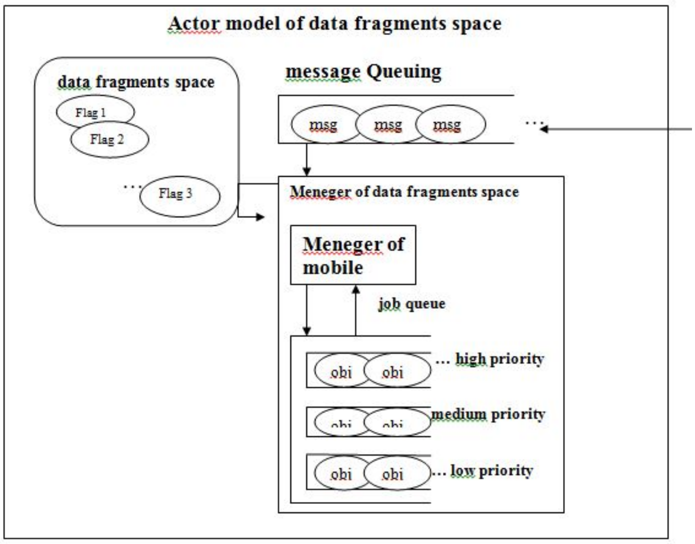

Figure –Structure of APFD

Conclusion

The article considers the separate agent-based mechanisms of functioning of the system of information support of innovations, and algorithms of organization of decentralized peer-to-peer communication between the nodes. Various approaches to implementation of mechanisms of communication of the agents are described. The existing models of communication of software agents are analyzed. Shortcomings of the considered models are revealed on which basis the approaches to increase in efficiency of interaction of mobile agents in distributed system of information support of innovations are offered.

On the basis of modification of existing models of inter-agent interaction the algorithms of information exchange between mobile agents allowing to increase efficiency of the distributed data processing by the agents and to reduce the total amount of the data transferred over the network are developed: 1) algorithm of agents communication based on the use of intermediary agents and their functions; 2) algorithms of information exchange between mobile agents based on local caching of information on the agent's location in the network and extension of address structure of the agent.

On the basis of the models developed during the researches and algorithms of interaction of software agents the method of minimization of internodal interactions in peer-to-peer problem-oriented distributed systems is offered. The method is based on clustering of software agents in semantic space presented in the form of conceptual domain model, and conversion of internodal interactions of the agents into intra-nodal ones. Implementation of the method provides reducing of load on communication infrastructure and increase in coefficient of accessibility of application services of software agents.

References

1. Alouf S., Huet F., Nain P. Forwarders vs. centralized server: An evaluation of two approaches for locatingmobile agents. – 2002. – No 49. – P. 299-319.
2. Carreiro N., Gelernter D. Linda in context.– 1989. – No 32. – P. 444-458.
3. Stefano D., Santoro C. Locating mobile agents in a wide distributed environment.–2002. – No 13. – P. 844-864.
4. Masloboev A.V. Multiagentnaya tehnologiya informasionnoi podderjki innovasionnoi deiyatelnosti regione. –2009. – P. 242-265.
5. Masloboev A.V. Multiagentnaya sistema integrasii raspredelennyh informasionnyh resursov innovasii. Programnye produkty i sistemy. – 2007. – No 4. – P. 30-32.
6. Rybina G.V. Modeli, metody I programnye sredstva podderjki vzaimodeistva intellektualnyh agentov. Informasionnye tehnologii I bychislitelnye sistemy. –2008. – No 3. – P. 22-29.

UDC 546.23:548.5

[1]Ismailov D., [2*]Chikhray Y., [1]Abdullin Kh.,[1]Gabdullin M.

[1]National Nanotechnological Laboratory, al-Farabi Kazakh National University, Almaty, Kazakhstan
[2]Institute of Experimental and Theoretical
Physics, al-Farabi Kazakh National University, Almaty, Kazakhstan
*e-mail: chikhray@physics.kz

Synthesis of CNT and CNT-Cu composites

Abstract. Nanostructured carbon materials feature unique properties and the expanding range of applications, so the research of methods for their synthesis is of high actuality. During the last years, even well-known CVD method of CNT synthesis was significantly modified and upgraded. In most of these advances, the uniformity of homogenous catalyst particles was concerned as the main goal. This paper presents results in the development of technological procedures for uniform deposition of catalysts from aqueous solutions of salts and electrodeposition with better CNT parameters.The water-soluble salts used were nickel nitrate and cobalt acetate. Degreased in organic solvents and cleaned with ultrasound the substrates were immersed in aqueous solutions of salts. Particles of metal oxides were formed while the sample was annealed in muffler at 400^{o}C in the air. Then CNT were synthesized in a quartz flow reactor in hydrogen at temperatures 650-700^{o}C in ethanol vapors. Raman spectra of so produced samples correspond to MWCNT. Ratios of I_D/I_G lines comprised 0.8-1.2. Electrodeposition of catalyst was used to improve the uniformity of CNT deposits. The deposition was from nickel nitrate solution with the addition of water-soluble polymer. One part of obtained samples was directly used for CNT synthesis. The second part was preheated at 400^{0}C in the air. CNTs were synthesized at 650^{0}C from ethanol vapor in 15 minutes. Revealed, that catalyst pre-heating in air leads to much more uniform CNT cover. At that, the quality of CNT is higher, such as ration I_D/I_G ~0.8. So the structural perfection is higher than in the case of a catalyst deposition from solution. Further electrolytic deposition of copper over CNT layer allowed obtaining CNT-Cu composite. SEM images show the morphology of so obtained composite as viewed from CNT side.

Key words: CNT, sol gel-method, electrodeposition, spin coating, ZnO, CNT-Cu composites.

Introduction

Carbon nanostructured materials such as carbon nanotubes (CNT), graphene, carbon fibers and based on them composites feature unique properties and a wide range of applications [1-3]. Therefore developments of synthesis methods for such structures are of high actuality. A good synthesis of CNT-based composites should have high uniform deposition of CNT, which demands uniform distribution of catalyst's particles, such as iron, nickel, cobalt. Given article describes improvements of sol-gel technique, methods of electrodeposition and spin coating for the production of catalyst particles and following synthesis of carbon nanomaterials and composites.

Sol-gel methods

Sol-gel method [4-6] was used for deposition of metal salts on a silicon substrate with the purpose to create catalyst particles as the points of CNT's growth. For that purpose,sol was made based on the solvent metal salts and a chelating agent. Water-ethanol mixture was used as a solvent; acetates were used as metal salts, water-soluble polymers and some amount of lactic acid were used to prevent aggregation. The sol was carefully mixed in magnetic stirrer during 3-24 hours.

For uniform deposition of thin films of metal salts over the flat silicon wafers we've used the procedure of centrifugation (spin coating), in which an excess amount of the sol solution is placed on a substrate which is then rotated at a high speed to uniformly spread the liquid across the surface of the substrate under centrifugal force. It is important to provide a uniform wetting of the substrate. The transparent sol solution was applied to the pre-degreased surface of a silicon substrate placed on the table, which was then rotated at about 2000 rpm for 2-3 minutes. Then the sample was dried in an oven at 110°C until the gel formation and then placed for binding annealing in the air in a muffle furnace at about 500°C at which oxides are formed from the gel particles.

Synthesis of CNT was carried out by placing substrates in the synthesis reactor, sealing the reactor and heating-up in a hydrogen atmosphere at a rate of 6-7 degrees per minute. During the heating, metals are reduced from oxides so forming catalyst particles. The synthesis was carried out for 10 minutes in the ethanol vapor. Fig. 1 shows the surface morphology of the samples obtained in a single experiment on substrates which were deposited by sol-gel method catalyst particles. It is seen that the metal salt concentration in the initial solution plays an important role in getting the CNT layer. CNT layer is not continuous at low concentrations of salts in initial sol; instead at a higher concentration, the bundles of multi-walled CNT are formed. The optimum concentration for obtaining high-quality multi-walled CNTs is derived.

Hydrothermal method

We used the hydrothermal method to grow arrays of zinc oxide nano-rods on silicon substrates. SEM pictures of the original ZnO bars are shown in Fig. 2a. Then, by applying dilute ferric chloride solution to the substrate surface, followed by annealing, the oxide nanoparticles were obtained dispersed over the surface of nano-rods and having a high specific surface area. Such substrates have been used for the low-temperature synthesis of CNTs in a hydrogen atmosphere with ethanol vapor. CNTs of sufficiently high quality were obtained. Thus we advanced the method of hydrothermal synthesis to substrates with a high area and coated them with the catalyst particles to produce CNTs.

Electrodeposition

To create the catalyst's nanoparticles on the substrate surface we used an electrodeposition method. Electrolyte for the deposition was the mix based on an aqueous solution of metal salt, the surfactant Triton X-100. The ferrous sulfate (II) or nickel sulfate (II) were selected as the metal salts and sodium sulfate (Na_2SO_4) was used to increase electrolyte conductivity. The typical solution had a concentration of 0.05 M of nickel or iron sulfate and 0.5M of sodium sulfate; boric acid was added as a buffer for adjusting pH. The solution was thoroughly stirred on a magnetic stirrer for 3-24 hours and filtered before use.

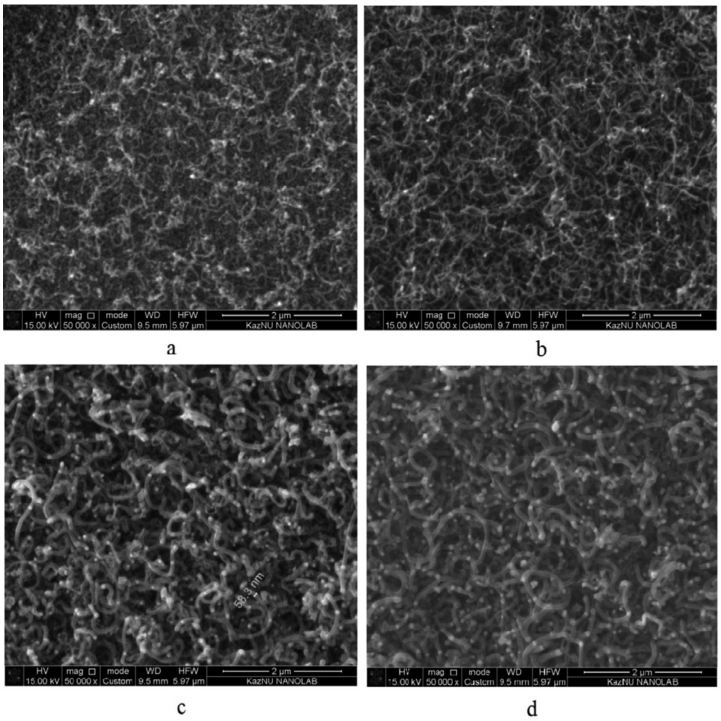

Figure 1 – CNT synthesized at 650°C on substrates with different concentration of sol: a) 0.0002 M; b) 0.0005 M; c) 0.001 M; d) 0.002 M.

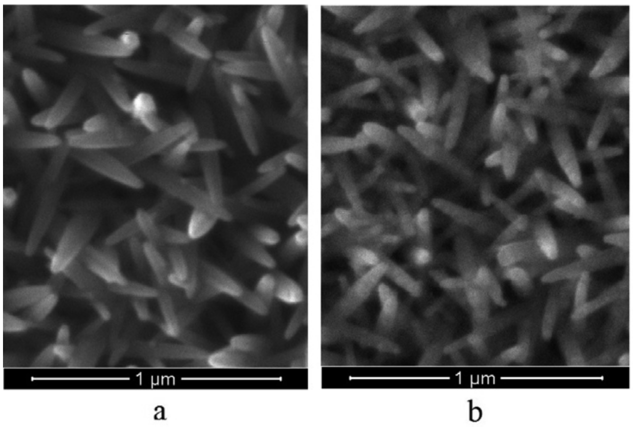

Figure 2 – Nano -rods of hydrothermally synthesized ZnO:
a) initial; b) with deposited nanoparticles of copper oxide, ready for CNT synthesis

Cathodic electrodeposition was performed using a stabilized current source-potentiostat Elins P-30J in the three-electrode configuration. As a working electrode, a counter electrode and a reference electrode were used, respectively, a silicon substrate, a platinum electrode, and a silver chloride electrode. The deposition was performed at a current of 10 mA/cm^2 and the deposition time was varied from 30 seconds to 10 minutes. Then, the substrate was pulled out and washed in water.

It has been found that an important process step is the oxidative annealing in air at 450-500°C. CNT synthesis is then carried out using substrates prepared as described above. Fig. 3 shows the morphology of the samples on the surface of CNTs substrates obtained by electrodeposition of catalysts, depending on electrodeposition process duration. It can be seen that the CNTs synthesized at certain parameters of the deposition process do not grow if electrodeposition was short (15-30 seconds), while the longer duration of electrodeposition (over 3 min) leads to catalyst particle size of 100-400 nm and to bundles of multi-walled CNT.

Electrospinning

Electrospinning method is one of the most effective methods to obtain carbon fibers and composites [7-9]. Synthesis of the catalyst nanoparticles by electrospinning is based on the use of polymer materials and mixtures of salts having carbon solubility. With electrospinning it can be easily achieved, that small amounts of metal salts will be very uniformly distributed over the length of the fibers in the polymer. During the subsequent heat treatment of fibers under specific conditions, the metal oxides can be formed with simultaneous destruction of the carrier (polymer), providing that the oxides are not aggregated into larger particles, and are formed with nano-size distribution close to monodisperse one.

The polymers we used in experiments were: polyvinyl alcohol (PVA), polyvinyl pyrrolidone, polyvinyl acetate (in some cases). Salts of metals such as nickel acetate, cobalt, copper, nickel and iron nitrates and others were used to form the catalyst nanoparticles.

Fig. 4 shows SEM image of composite fibers immediately after synthesis (a) and after annealing in air at 250°C for 2 hours, followed by reductive annealing in hydrogen (250°C, 2 hrs). As it is seen from the picture, the nanoparticles formed after annealing are of average diameter near 50 nm with a small spread. Actually, it was possible to control the nanoparticle sizes in a wide range varying the concentration of the initial solution of polymer and salt. The polymer itself collapses and evaporates during annealing in an oxidizing atmosphere.

It has been found also that is necessary to keep a low rate of heating during the fibers anneal to form oxides nanoparticles (about 1-3 degrees per minute). In this case, the polymer degradation process runs at an optimal speed, and if polymer fibers are uniformly covered with metal salts they are retaining their shape while gradually thinning, and oxide particles are formed with a small spread in size. In the case of higher heating speed (8-10°C per minute) we observed twisting and deformation of the fibers, and polymer melting, which leads to adhesion of the material and to a larger amount of coarse particles with the formation of oxides inclusions.

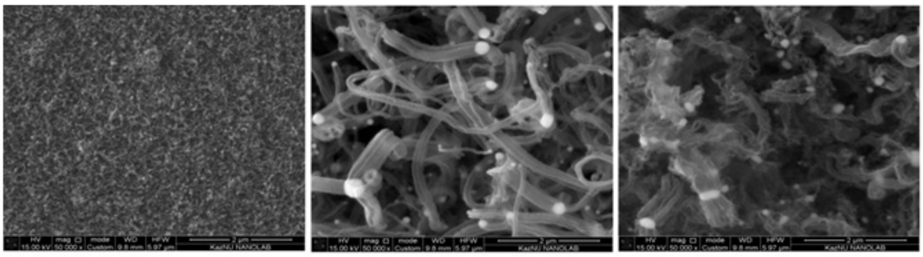

a b c

Figure 3 – CNT synthesized at 650°C on the substrates with the electrodeposited catalyst depending on electrodeposition duration: a) 15-30 seconds; b) 3 minutes; c) 10 minutes.

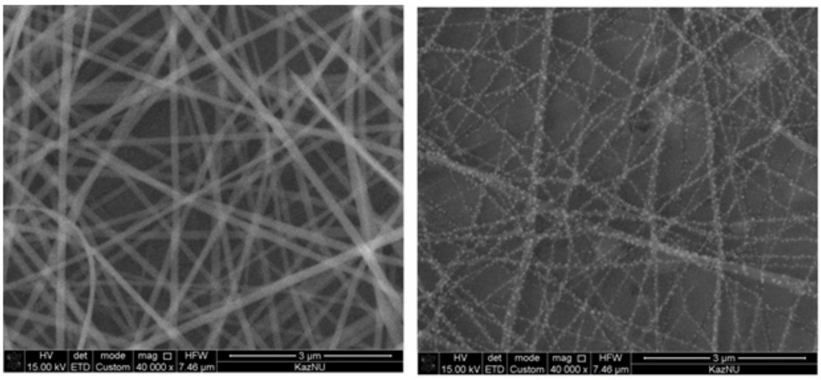

a b

Figure 4 – Composite fibers PVA+AcNi: a) after synthesis; b) after annealing in hydrogen.
The vacuum heat treatment allows producing nanoparticles with an average size of 20 nm,
as shown in Fig. 5, and the fibers do not dissolve,
as it happens during annealing in an oxidizing atmosphere, but became graphitized.

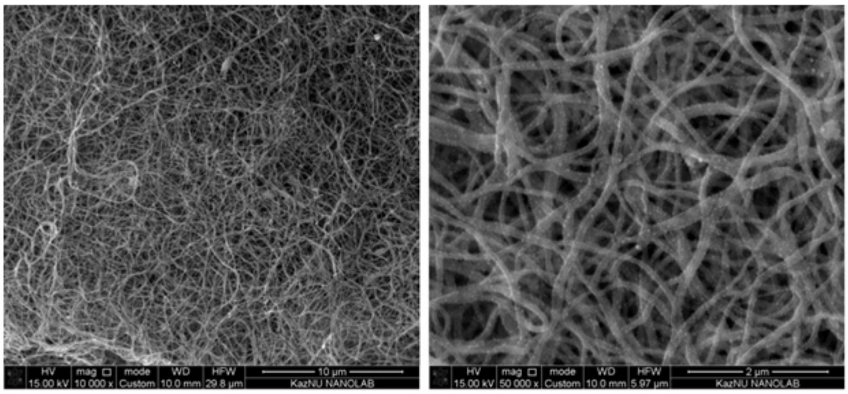

a b

Figure 5 – Composite fibers:
a) initial; b) after anneal at 500°C in vacuum.

Figure 6 shows Raman spectra of annealed fiber with catalytic nanoparticles and Raman spectra of CNTs samples obtained by using these fibers as substrates for the CNT synthesis at 650°C in a mixture of hydrogen and ethanol vapor (as the carbon source). As it can be seen from the figure, the Raman spectrum of the annealed fiber (curve 1) is close to the spectrum of amorphous carbon. Curve

2 corresponds to CNTs grown on the annealed fibers. According to the literature, the spectrum corresponds to the multi-walled CNTs. As can be seen from Fig. 6, the spectrum intensity of the D band is lower than the band G, and sufficiently high intensity of 2D peak is observed. This evidences the high quality of the nanotubes.

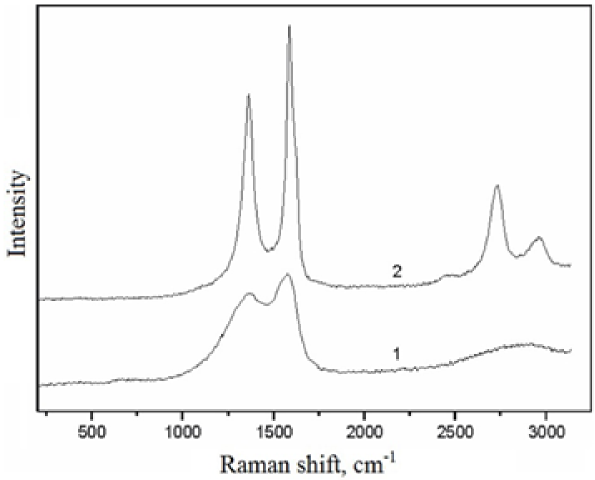

Figure 6 – Raman spectra of fibers after vacuum anneal of PVA polymer at 500°C (curve 1) and of CNT's synthesized on these fibers at 650°C in ethanol vapors (curve 2).

CNT-Cu composites

Application of CNT (for hydrogen storage, for example) requires that CNT should be not just a powder but compacted as a composite film (for instance) which can sustain higher temperatures and allows hydrogen permeation. Such a composites could be created binding CNT to metals. In our work the composite of SWCNT with copper was created using copper electrodeposition over CNT layer. Since we synthesized SWCNT over paper filter it is convenient to use it as a dielectric separator between CNT layer (cathode) and copper (anode). The copper was electrodeposited on CNT layer from electrolytic solution (0.5MCuSO4 + 0.2M H2SO4) at low density of current during about two hours. Fig. 7 shows the morphology of the composite we've prepared by deposition of copper over the layer of CNTs, a view from the CNT layer. The CNT layer was obtained from electrodeposition and appears as nonstructural, however, if the sample is bent enough to start cracking, the appeared surface cracks are filled with stretched nanotubes, which can be clearly seen in the Fig. 7. Raman spectrum of CNT-Cu composite corresponds to the spectrum of multi-walled CNT. Thus, electrolytic deposition of copper on the conductive layer of CNTs has allowed obtaining composites based on CNT and a copper.

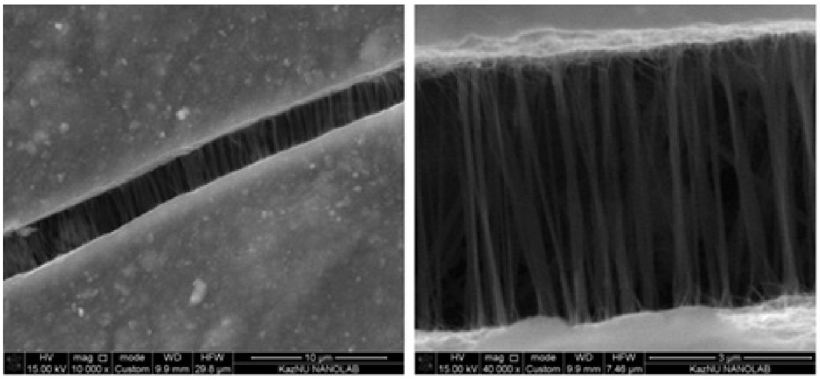

a b

Figure 7 – Front side (a) and the area of rupture (b) of CNT-Cu composite

Conclusion

The sol-gel method, hydrothermal method, electrodeposition and electrospinning were refined with the purpose to form better catalyst nanoparticles and the subsequent synthesis of carbon nanotubes and composites based on them. The structural properties and morphology of synthesized CNT samples, depending on the technological conditions of synthesis were studied. CNT-Cu composites were synthesized based on carbon nanotubes and a deposited copper layer.

Acknowledgements

The study was carried out with the support of grant #3109/GF4 of Ministry of Education and Science of Kazakhstan.

References

1.W. Gu, G. Yushin. Review of nanostructured carbon materials for electrochemical capacitor applications: advantages and limitations of activated carbon, carbide-derived carbon, zeolite-templated carbon, carbon aerogels, carbon nanotubes, onion-like carbon, and graphene // WIREs Energy Environ. – 2014. – Vol. 3. – P. 424-473.

2. Y.H. Wu, T.Yu, Z.X. Shen. Two-dimensional carbon nanostructures: Fundamental properties, synthesis, characterization, and potential applications // J. Appl. Phys. – 2010. – Vol. 108. – P. 071301.

3. O.A. Shenderova, V.V. Zhirnov, D.W. Brenner. Carbon nanostructures // Crit. Rev. Sol. St. Mat. Sci. – 2002. – Vol. 27. – P. 227-356.

4. K.A. Shah, M.A. Malik, S.M. Ali Andrabi, M.A. Shah. A Study of Catalyst Preparation Methods for Synthesis of Carbon Nanotubes // Chemical Science Transactions. – 2016. – Vol. 5. – P. 1-7.

5. V.M. Irurzun, Y. Tan, D.E. Resasco. Sol–gel synthesis and characterization of Co-Mo/silica catalysts for single-walled carbon nanotube production // Chem. Mater. – 2009. – Vol. 21. – P. 2238-2246.

6. A. Szabó, C. Perri, A. Csató, G. Giordano, D. Vuono, J.B. Nagy. Synthesis Methods of Carbon Nanotubes and Related Materials // Materials. – 2010. –Vol. 3. – P. 3092-3140.

7. X. Mao, T. Hatton, G. Rutledge. A review of electrospun carbon fibers as electrode materials for energy storage. // Cur. Org. Chem. –2013. – Vol. 17. – P. 1390-1401.

8. L. Feng, N. Xie, J. Zhong. Carbon Nanofibers and Their Composites: A Review of Synthesizing // Properties and Applications Materials. – 2014. – Vol. 7. – P. 3919-3945.

9. S. Homaeigohar, M. Elbahri. Nanocomposite Electrospun Nanofiber Membranes for Environmental Remediation // Materials. – 2014. – Vol. 7. – P. 1017-1045.

International Journal of Mathematics and Physics 7, №2, 65 (2016)

UDC 539.21; 539.12.04

[1*]Mukashev K.M., [1]Muradov A.D., [2]Umarov F.F., [3]Michalenkov V.S.

[1]Faculty of Physics and Technology, al-Farabi Kazakh National University, Almaty, Kazakhstan
[2*]Kazakh-British Technical University, Almaty, Kazakhstan
[3*]Institute of Metal Physics Academy of Sciences, Kiev, Ukraine
[*]e-mail: kanat-kms@mail.ru

Possibility of separation of elastic and inelastic channels radiation damage metals

Abstract. In this work we have performed a systematical investigation of energy dependence of the radiation defects distribution profile in three different materials – tantalum, molybdenum and stainless steel of type 10X18H10T–VD irradiated by high energy protons. It has been shown that in the stainless steel and tantalum, regardless of proton energy, the vacancy complexes similar by configuration appear which are described by the slightly expressed elastic channel. The defects recover in one annealing stage with different migration activation energy. At the same time the molybdenum radiation damageability consists of two components in each of which exists its own mechanism of defects formation. For high energy protons what's important is the inelastic channel of interaction and formation of sub cascades, which are created by primarily knocked-on atoms of considerable energies. However, for low energy protons, the processes of elastic interaction with lattice atoms and emergence of atomic hydrogen in the end of run important.

Key words: positron annihilation, tantalum, molybdenum, proton irradiation, point defects, vacancy complex.

Introduction

It is known that the effects of nuclear radiation on a matter is accompanied by a number of new phenomena [1-4]. The most important among them are nuclear reactions and a change associated with them in the elemental composition, formation and the emergence of clusters of point defects, damage to the matrix caused by cascade atom – atom collisions, etc., and as a result, disturbance in the integrity of the crystal. In order to learn the phenomena related to the changes in the material's crystal structure in the active zone of the reactor, it often suffices to conduct simulation experiments at the accelerators of charged particles. At the same time a quite important task is to study the profile of the defect distribution along the depth of the damaged layer. In the past, a computer program was developed for this purpose on the basis of theoretical research in order to calculate the profile of the displaced atoms by the depth of passing of heavy ions in the material [5]. But any computer program, regardless of how universal it is, yet cannot take into account all aspects of the complex process of interaction of charged particles with the real crystal lattice, furthermore, it cannot be acceptable in situations when the object of study is multicomponent alloys.

Charged particles lose energy when moving in the matter. Energy losses of the incident particle can occur by various ways, including ionization and excitation of the electron shells, the atoms' polarization of the medium, the radiation losses and nuclear stopping, whose role in the formation of structural defects may be different. Consequently, the profile of the defect distribution in the depth may also be different, the location of which depends on the type and parameters of the bombarding particles of the target material, and the irradiation temperature. In this regard, experimentally obtained parameters of the defect structure may differ considerably from those calculated theoretically.

The average path traveled by a charged particle in matter to a full stop is called its range R. The latter depends on the particle energy and the properties of the target's material. The range of the particle is usually expressed through the length of the path, d and density of the material, ρ:

$$R = d \cdot \rho \; [g \cdot cm^{-2}] \qquad (1)$$

To estimate the interaction of particles with the matter in the reference books we can find the following: particles energy – E in the lab coordinates and expressed in MeV’s; particle ranges $R(E)$, expressed in $g \times cm^{-2}$; stopping power $S(E)$in $MeV \times cm^{-2} \times g^{-2}$; derivatives of stopping power by energy $D(E)$, used as a correction factor [6,7]. In order to calculate the range of a particle whose energy lies between the tabular data, one has to use the formula:

$$R(E)\Delta E) = R(E) + \frac{\Delta E}{S(E)} - \frac{1}{2}\left|\frac{\Delta E}{S(E)}\right|^2 \cdot D(E), \quad (2)$$

where E is the nearest table value of energy. On the contrary, for the calculation of energy corresponding to range, the value of which lies between the values in the table, you can use the formula:

$$\begin{gathered} E(R+\Delta R) = E(R) + S(E)\cdot\Delta R - \\ -\frac{1}{2}S^3(E)\cdot D(E)\cdot(\Delta R)^2 \end{gathered} \quad (3)$$

To find intermediate values of $S(E)$, which are absent in the table, a linear interpolation relationship is used:

$$S(E+\Delta E) = S(E) + D(E)\cdot\Delta E, \quad (4)$$

where $S(E)$ is the closest value of the stopping power. Similarly, an intermediate value $D(E+\Delta E)$, which is not listed in the table, can be found by the relation:

$$D(E+\Delta E) = D(E) + \frac{\delta D}{\delta E}\cdot\Delta E, \quad (5)$$

Under these conditions, the accuracy of calculation of the tabulated data is ~ 1%.

Experimental

Because the passage of charged particles in the matter is accompanied by its successive energy losses, the study of the defect distribution profile by depth is, in principle, a task of studying the energy dependence of metal radiation damageability. One way to solve this problem is to study metal defect structure by sequential etching of the surface. From the other hand, you can solve it on the basis of variable thickness of the absorber method. Obviously the most acceptable way to solve it is the latter, non-destructive method of research, the essence of which is to irradiate by the charged particles of high energy and studying the stack of foils, the total thickness of which is greater than the mean free path of the particles in the material. By using such a technique, each foil is irradiated by particles of different energy and contains the respective structural damages typical for a given depth of the material. As the test objects we used polycrystalline Mo and Ta, and stainless steel-VD 10H18N10T as a foil with a thickness of 100 μm and a diameter of 17 mm each. The initial state of the metals achieved by annealing at T = 1200°C and for steel the temperature was at 1050°C for 1.5 hours in a vacuum of 10^{-5} Pa. The thickness of each foil Δd defines a path element $\Delta x_i = \Delta d_i \rho$, on which there happens a loss of energy of protons $\Delta E_i = s_i(E)\Delta x_i$; the mean energy of the protons on the other side of each foil will be $E_{xi} = E_i - \Delta E_i$. Consequently, each successive foil is irradiated with protons of different energies. If one studies the degree of damage, its energy dependence can be established. Irradiation was carried out by protons flow $1.2 \times 10^{13}\ cm^{-2}c^{-1}$ up to $2 \times 10^{17} cm^{-2}$fluence.

The main research tool in this case is the electron-positron annihilation (EPA) method. Being one of the major nuclear-physical methods of studying the state of the condensed medium, the method of electron-positron annihilation is a very sensitive tool to various kinds of damages of crystal structure. Spectrum shape of the angular distribution of annihilation photons (ADAP), caused by annihilation of positrons with electrons of the material, changes significantly at localization of positrons near the defects in the crystal lattice, as well as from the atomic environment of defective regions. Slow positrons also react to the change of the structure’s order. Therefore positron probe is an ideal tool for studying electronic states of the metallic materials local microregions [8-10].

The study of structural defects of materials was performed by the spectrometer with a linear-slit geometry with an angular resolution of 0.5 mrad. As a positrons source we used the isotope ^{22}Na with 10 mCi activity. The measurement of ADAP spectrum allows to determine the relative contribution to the annihilation of positrons process with the conduction electrons and ion core electrons. To this effect, we experimentally measure~~s~~ the intensity of the annihilation gamma rays as the dependence of counting rate of pulses that are coincident in time of 2 photons, which are detected by opposing detectors on the displacement angle of the movable detector θ. ADAP spectra measured for different states of the material, are normalized to a single space. It is not difficult to establish that the spectrum for the defective material has a higher intensity at the maximum and the narrow width at half maximum (Fig. 1).

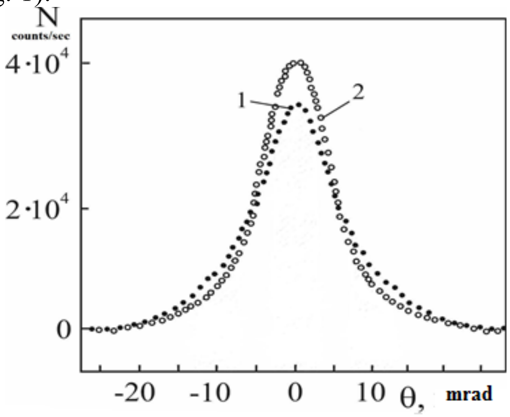

Figure 1 – Experimental ADAP spectra: 1 - for annealed materials; 2- for irradiated materials

Results and discussion

To interpret the results of studies used the following structure-sensitive annihilation parameters: F – positron annihilation probability redistribution between the conduction electrons and bound electrons, as well as its corresponding increment ΔF relative to values for the initial state, that are recovered by processing the spectrum of the angular correlation of annihilation radiation [8]. The results of studying stainless steel according to these conditions by the annihilation parameters change data are summarized in Table 1.

High energy protons irradiation change 3 considerably the spectrum's shape of annihilation photons angular distribution. The spectrum becomes narrower in half-width and maximal intensity raises caused by the redistribution of positrons annihilation probability with conduction and ion core electrons. These factors are visible in annihilation parameters change. If for annealed sample the value $F = 0.15$, then after irradiation it increases almost as twice as much. The spectrum half-width (FWHM) for the initial state is equal to 6.1 mrad. The protons irradiation reduces it in average down to 5.6 mrad. In spite of the considerable changes in the parameters, the evident regularity between them and protons' energy in this case is not visible. Though, the certain tendency in the annihilation parameters behavior yet can be established. Thus, for example, the average value of the positrons annihilation relative probability F with particles energy increase steadily decreases. This can testify that the main contribution in the steel radiation damageability is carried in the low energy protons, which experience the elastic collisions with steel components atoms.

Table 1 – Parameters of steel annihilation by the depth of protons passage

$E_{initial} = 30\,MeV$ (Q= $2\times10^{17}cm^{-2}$ − $protons\ fluence; Ep$ − $current\ value\ of\ proton\ energy$)

Sample number	$E_{P,}$ MeV	X, μm	$F{=}S_P/S_g$	$f{=}N(0)/N(8)$	FWHM, mrad.
annealed	-	-	0.15	3.1	6.1
19	0	-	0.27	3.9	5.6
18	2.33	1750	0.24	3.9	5.6
17	6.40	1650	0.24	3.8	5.7
16	9.09	1550	0.28	3.4	6.0
15	11.29	1450	0.25	3.7	5.7
14	13.19	1350	0.31	3.6	5.8
13	14.91	1250	0.26	3.4	5.9
12	16.49	1150	0.23	3.2	5.9
11	17.97	1050	0.27	3.5	5.8
10	19.35	950	0.28	3.8	5.7
9	20.67	850	0.27	3.5	5.7
8	21.92	750	0.29	3.6	5.7
7	23.12	650	0.27	3.5	5.9
6	24.27	550	0.21	3.4	5.9
5	25.39	450	0.25	3.6	5.8
4	26.47	350	0.23	3.3	5.9
3	27.51	250	0.25	3.4	5.9
2	28.52	150	0.24	3.7	5.7
1	29.50	50	0.26	3.7	5.7
error ±	0.05	1.00	0.02	0.1	0.1

Therefore we can assume that the structural damages arising meanwhile in the steel samples are not much different between each other both by configuration and by positrons capture efficiency and correspond to the traps of one type. The latter is confirmed by the shape of isochronal annealing curves from the stack of the samples irradiated by different energy protons (Fig. 2). At EP = $29.5 \div 13.2\ MeV$ protons energy the materials basic properties recovery ends in the temperature range 350-600°C and at EP $\leq 6\ MeV$ – in the range of 250 – 550°C, that is existence of a certain relationship between protons energy and defects annealing temperature is evident.

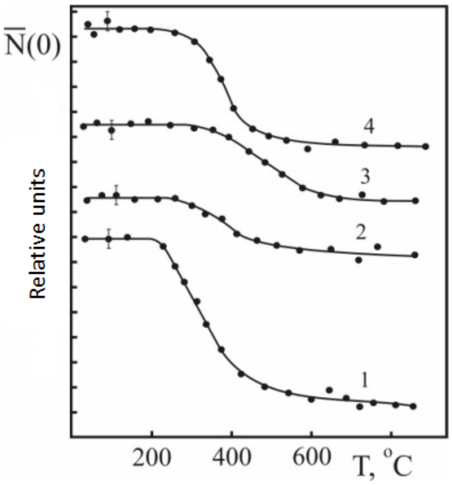

Figure 2 − The energy dependence by protons irradiated 10X18H10T – ВД steel annealing kinetics
1. E_P = 4.6 MeV; 2. E_P = 31.2 MeV;
3. E_P = 23.1 MeV; 4. E_P = 29.5 MeV

Apparently of the defects migration activation energy value, irradiation by high energy protons causes the dislocation loops with $E_a = 2.1 – 2.2\ eV$. It is evident that in the low energy protons case the vacancy complexes as a small subcascades or connected vacancy-impurity complexes with $E_a = 1.7 - 1.8\ eV$ are created. The most likely is the formation of connected vacancy-Cr atom state whose decomposition at annealing is trickier than that of others [9].

Unlike stainless steel, the polycrystalline tantalum irradiation at the same conditions leads to some characteristic changes in the annihilation parameters. It is very difficult to define a spectrum parabolic component for this metal in consequence of insignificant portion of free charge carriers. Therefore, the basic equivalent (instead of F) parameter is the ratio between the counting rate in the maximum of spectrum $N(0)$ to its value at the angle $\theta = 8$ mrad, that is $f = N(0)/N(8)$. The dependence of this parameter on protons energy is given in Fig.3a. The maximal spectrum narrowing, as well as considerable increase of the parameter $f = N(0)/N(8)$ is observed at low energies $\sim 5 - 8\ MeV$. With particles energy increase these parameters possess a steadily increasing or decreasing pattern.

Such changes in parameters, which characterize the spectrum shape, are possible only at corresponding changes of capture efficiency of positrons by defects, created by protons. As far as the effectiveness maximum corresponds to low energy protons, then we can suppose that the largest damageability tantalum is suffered consequently of elastic interactions. The nuclear reactions influence activated by inelastic interactions in the high energy region in this case is negligible. The actual picture of the structure damages in tantalum ~~is~~ can be determined as a result of isochronal annealing of individual samples from the stack irradiated by different energy protons (Fig. 3b).

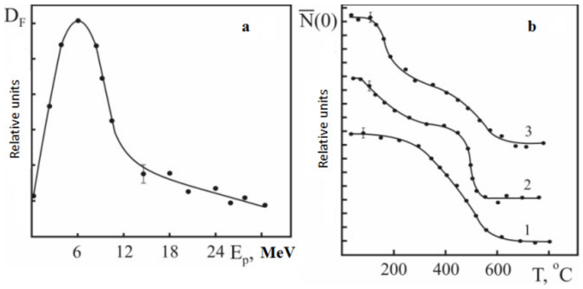

Figure 3 − The energy dependence of damageability (a) and annealing kinetics (b) of Ta, irradiated by protons with 30 MeV initial energy:
1. E_P = 6 MeV; 2. E_P = 25 MeV; 3. E_P = 30 MeV

One can see that the sample irradiated by low energy protons recovers in one stage in the temperature range of 250 – 600°C with curve amplitude ~15 % (curve 1), whereas at high energy irradiation the structure damages in Ta emerge with two recovery stages (curves 2,3). And with particles energy decreasing from 30MeV to 25MeV the beginning of the point defects migration is shifted sideways towards lower temperatures with simultaneous increase in portion of vacancy defects. This confirms the decisive contribution of elastic interactions in the process of defect formation. So, at protons irradiation with $E = 30\ MeV$ the vacancy stage portion makes up 41% from the damages common level. However, with energy decreasing to up to 25MeV it increases to up to 47%. Meanwhile the recovery second stage gets more relief appearance than in the first case. The migration activation energy's mean value for vacancy components is equal to $E_{a1} = 1.41 – 1.45\ eV$, and for dislocation and more complicated components, which are annealed during the second stage – $E_{a2} = 2.33 – 2.35\ eV$.

Still large interest in these experiments is presented by the study results of damageability distribution profiles of molybdenum, irradiated at the same conditions. For molybdenum in the annealed state, the annihilate photons angular distribution is approximated by one Gaussian, as far as the probing positrons are annihilated basically with ion core electrons. As a result, it becomes difficult to identify a parabolic component in the spectrum. But as a result of protons irradiation, the emerging structure damages enable the parabolic component responsible for positrons annihilation with free charge carriers to appear in the spectrum. Meanwhile the energy dependence of the relative annihilation probability $F = S_P/S_g$ have a more complicated and non monotonic nature (Fig.4). After certain energetic region 5 - 10 MeV in such the relative probability F is stay constant, in the sequel it is sharply decreased and achieve the minimum at about 18 - 20 MeV is increasing again up to E_P= 30 MeV. Such annihilation parameter dependence is can be activated by the appropriate defects distribution profile which is determine the defects both concentration and configuration along the trajectory of charged particles in matter.

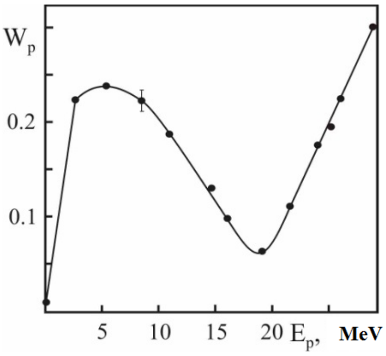

Figure 4 – The energy dependence of the Mo damageability irradiated by protons, with initial energy 30 MeV

The probable reason of such dependence can be difference in contribution in the process of radiation defects generation of the elastic interactions at $E_P < 18\,MeV$ energies and subcascade regions formation at$E_P > 20\,MeV$ on the one hand, and also the nuclear reactions specified role on the other hand. But in both cases the defects structure must be of vacancy, which is revealed by isochronal annealing results. Regardless of energy, as a result of the proton irradiation there emerge the vacancy complexes in Mo and in the annealing temperature range below 800°C only one incomplete return stage has been observed. Meanwhile, as the proton energy increases the defects migration temperature threshold ~~is~~ gradually shifts towards higher temperatures ranges – from 300 – 350°C to up to 450 – 500°C, which testifies emergence of more stable in terms of temperature defects in the metal. In [12], it is stated that the full annealing of Mo irradiated by protons is completed at approximate temperatures of 300 – 320°C. But this temperature is considerably lower than Mo recrystallization temperature, and this gives rise to a doubt in the above mentioned conclusion in [13]. However, annealing temperature that was reached in this investigation (850°C) is also not sufficient for a completion of even the first stage of recovery (III-stage), whereas according to [13] the recrystallization temperature of Mo is higher than 1000°C.

Conclusion

Thus, investigation of the defects distribution profiles by charged particles passing depth in three different materials has shown that in the stainless steel and Ta, regardless of protons energy, there appear configuration vacancy complexes similar by configuration, which are recoverable in one annealing stage with migration activation energy $E_a = 1.7 - 1.8\,eV$. The total damageability of stainless steel and Ta in the whole range of protons energy is formed basically by one low-grade elastic channel, whereas for molybdenum it is created from two components in each of which its defined mechanism of defects formation is in place. If for high energy protons, the inelastic channel of interactions and subcascades appearing are the basic, then for low energy protons the elastic interactions with lattice atoms and vacancy complexes and atomic hydrogen formation in the end of run are of high importance. The probable cause of such difference in radiation damageability of Mo and Ta polycrystals is the appreciable difference in atomic masses of these elements. Almost two timesexcess of Ta atomic mass over atomic mass of Mo is evidently the reason of implicitly expressed damageability at the expense of inelastic channel, situated below the response limit of the testing method. The basic mechanism of the radiation defects formation in stainless steel and Ta are evidently expressed elastic interactions. The role of nuclear reactions in the structure damages creation is weakly expressed in this case. The defects created by low energy protons are annealed in one stage, whereas high energy particles influence causes emergence of the radiation defects, which are of vacancy and dislocation nature and recover in two stages.

Acknowledgements

The authors would like to thank Dr. Umarov T.F. for his very useful help.

References

1. Agarvala R.P. Radiation Damage in Some Refractory Metals // Materials Science Foundations. − 2005. − Vol. 25. − P. 125-130.

2. Zinkle Steven L., Wiffen F.W. Radiation Effects in Refractory Alloys // Space Technology and ApplicationsInternational Conference Proc.− 2004. − Vol. 699. − P. 733-740.

3. Leonard K.J. 4.06-Radiation Effects in Refractory Metals and Alloys // Comprehensive Nuclear Materials. − 2012. − Vol. 4. − P. 181-213.

4. Grossbeck M.L. 1.04-Effect of Radiation on Strength and Ductility of Metals and Alloys // Comprehensive Nuclear Materials. − 2012. − Vol. 1. − P. 99-122.

5. Antonov A.G. The investigation of tritium entry in environment at liquid leady-lithium irradiation eutectic through channel wall from stainless steel // The liquid metal application in the national economy. – Obninsk. – 1993. − P. 181-183.

6. Myllyia R., Xostomaova J., A time-to amplitude converter with constant-fraction timing discriminators for short time interval measurements // Nucl. Jnstr. and Methods. – 1985. − P. 568-578.

7. Ibragimov Sh. Sh., Reutov V.F., Abdurashitov I. Yu. Radiation damageability of Mo at high temperature irradiation by protons with initial energy 30 MeV // VANT, ser. FRP and RM. − 1977. − Vol. 1. – No 21. − P. 76-79.

8. Mukashev K.M. Low positrons Physics and positron spectroscopy. – Almaty. – 2007. − P. 508.

9. Mukashev K.M., Tronin B.A. and Umarov F.F. Behavior of Structure Defects and Hydrogen in neutron-irradiated stainless steels studied by positron-annihilation method // Rad. Effects & Defects in Solids. − 2009. − Vol. 164. – No 10. − P. 611-618.

10. Mukashev K.M. and Umarov F.F. Positron annihilation in Titanium Alloy modified by proton irradiation // Rad. Effects & Defects in Solids. − Vol. 167. – No 1. − P. 1-11.

11. Berestetsky V.B., Livshits E.M., Litaevsky A.P. The relativistic quantum theory. − M. Nauka, 1968. − Vol. 1. − P. 480.

12. Dextyar I.Ya., Mukashev K.M., Rustamov Sh.A., at all. The positron annihilation in irradiated by chromium- ruthenium alloys // Ukr. Fis.Jurnal.− 1984. − Vol. 29. – No 11. − P. 1679-1681.

13. Belyaev V.N., Zemlerub P.A., Kovalev V.Yu. at all. The positrons lifetime spectrometer // Preprint ITEF – 95, − M., – 1980. − P. 26.

UDC 621.38-022.532

[1*]Muradov A.D., [1]Yar-Mukhamedova G.Sh.,
[1]Mukashev K.M., [2]Przybylski M., [1]Sandybayev Y.Y.

[1]Department of Solid State Physics and Nonlinear Physics, Faculty Of Physics And Technology, al-Farabi Kazakh National University, Almaty, Kazakhstan
[2]Academic Centre for Materials and Nanotechnology, Krakow, Poland
[*]e-mail: abyl.muradov@mail.ru

XRD analysis of nanolayered molybdenum disulfide obtained by sol-gel technology

Abstract. The deposition of molybdenum disulfide by sol-gel technology was investigated. Initial mixture for the synthesis was prepared from ultrafine powders of metals and elemental sulfur. Synthesis was performed slowly during 2 h by precipitation of the molybdenum hydroxide from aqueous 0.001M solution of $MoSO_2$ and sodium hydroxide with constant stirring. By morphology obtained layers of particles of molybdenum disulfides deposited on silicon substrate have bimodal distribution: from 0.1 to 0.2 µm with a maximum at 0.15-0.18 µm; and from 0.4 to 5.0 µm with a maximum at 3.0 µm. It was established that obtained molybdenum oxide hydroxide particles do not coagulate within 48 h, which is associated with the formation of micellar positively charged particles. According to the data of X-ray diffraction and Raman spectroscopy disulfide particles have a layered structure, and the main phase is a hexagonal disulfide with a space group of symmetry P63 / mmc. By X-ray images it was established that increasing the sulfur content in the mixture in the synthesis of nanostructured molybdenum disulfide is reflected on reducing the intensity and number of reflections phase, as well as on reducing the rate and the maximum temperature of combustion. Upon sulfur excess higher than 15% by weight, the phase of mainly hexagonal molybdenum disulfide was observed in the product. By estimation of zeta potential, the value of zeta potential was 54 mV, clearly indicating that the particles obtained in aqueous suspension are not coagulating due to the predominance of the processes of repulsion of the particles.

Key words: sol-gel technology, molybdenum disulfide, XRD-analysis, Raman spectroscopy.

Introduction

Molybdenum disulfide is used in areas such as photovoltaic cells, rechargeable batteries, and solid lubricants. This is due to their optical, electrochemical and mechanical properties. Molybdenum disulfide has a hexagonal crystal lattice in which metal layers are arranged between two layers of sulfur connected by weak van der Waals forces [1]. Because of the structural features of the crystal lattice, it is interesting in the applied aspect.

Due to the widespread in nature as molybdenite, MoS_2 has been one of the most studied layered transition metal dichalcogenides (TMDCs). Monolayer MoS_2 is a semiconductor with a direct bandgap of 1.8 eV [2]. This property of MoS_2 is inspiring, which will largely compensate the weakness of gapless graphene, thus making it possible for 2D materials to be used in the next generation switching and optoelectronic devices. Thus far, MoS_2 has achieved primary progress in the following fields, including energy conversion [3] and storage [4] and hydrogen evolution reaction (HER) [5]. Additionally, MoS_2 with odd number of layers could produce oscillating piezoelectric voltage and current outputs, indicating its potential applications in powering nanodevices and stretchable electronics [6].

At present, in the world, intensive work is aimed at the study of photoconductive materials for use in photovoltaic solar energy converters and other optoelectronic devices. In this aspect, molybdenum disulfide (MoS_2) is a promising active component of such materials, because it has a broad absorption spectrum in the range from 200 to 1000 nm, and also has a high photo – and corrosion resistance [7].

Due to the particular optical and electrical performance of TMDCs, as one of the most typical existing TMDCs, MoS_2 itself has evolved into a vast studying topic, gradually finding its applications in many related areas, such as transistors [8], photodetectors [9], solar cells [3], etc.

Therefore, the fabrication of hybrid structures based on 2D materials by taking advantages of the individual component is one of latest research trends. The ultimate goal is to synthesize more superior composites, achieving synergistic effect or structural reinforcement.

Early in 2011, Yandong Ma's group has calculated that the binding energy of per C atom binding to MoS_2 is A 23 meV and the forming interlayer spacing between graphene and by MoS_2, band structure of graphene could be largely preserved in this hybrid structure while introducing a small bandgap of 2meV which was almost negligible [10]. Further analysis indicated that this band gap was tunable by varying the interlayer spacing, highlighting the prospect in designing of devices with tunable bandgap and high electron mobility simultaneously. In 2011, A. K. Geim proposed “van der Waals heterostructures” on Nature [12], showing a landscape for future development of 2D hybrid structures. Many challenges were accomplished afterwards, pushing devices into real practical applications. J. C. Grossman and his co-workers confirmed the feasibility by studying the performance of 1 nm-thick solar cell based on MoS_2/graphene through the first principles calculations [11]. First, MoS_2 like TMDCs monolayers could absorb 5 -10% of incident sunlight within 1 nm in thickness, exceeding that of traditional semiconductors (GaAs and Si) more than one order of magnitude.

In addition, A type-II Schottky junction within 1 nm which would greatly facilitate separation and transport of carriers in the stacking interfaces was constructed, exporting a high power conversion efficiency (PCE) up to ~1%. Moreover, MoS_2/graphene solar cell demonstrated a power density of 0.25 – 2.5 mW/kg, which were higher by approximately 1 – 3 orders of magnitude than the best existing ultrathin solar cells [11]. Further experimental observation proved the ultrafast interfacial charge transfer in TMDCs stacking structures, ensuring the effective charge collection and utilization in later circuits [12], opening up the development for light detection and harvesting in atomically thin devices.

Band engineering of MoS_2, achieving composite constructions with superior electrical performance and tunable band structure, is a leading topic in the near future. Therefore, to put the existing flexible optoelectronic and energy storage devices into practical and industrial applications, the most feasible method and technology are needed to be further investigated [13].

Experimental procedure

In this work, molybdenum disulfide obtained by sol-gel technology was considered as an investigated material. Optical measurements were made by an optical microscope Leica DM 6000M, which has a resolution of 200 nm, the maximum magnification of 1500 and is equipped with high-resolution digital camera Leica DFC Twain.

The quality and uniformity of the surface condition of the obtained samples were studied using Raman spectroscopy. The Raman spectra of obtained samples were studied on NT-MDT NTEGRA by using blue laser light with a wavelength of $\lambda = 473$ nm and a spot diameter of 2 μm. Full range of Raman / fluorescence was recorded at each point of the test sample, followed by software processing. Due to the high quality of the optical system, two- and three-dimensional distribution of the spectral characteristics of the sample could be examined with a spatial resolution close to the theoretical limit.

To solve the problems of X-ray diffraction and X-ray analysis of the materials, X-ray diffractometer DRON-7 with a wavelength $\lambda_{CuK\alpha} = 1.54178$ Å was used.

The phase composition of molybdenum disulfide was analyzed at room temperature using a diffractometer Shimadzu XRD-7000S, type of anode – Cu, focus -0.4x 12 mm, and a maximal power –2,7 kW, and scan rate -1°/min with a 0,002°. Decoding of the data was performed using the database of JCPDS X-ray diffraction.

Experimental part

Synthesis of molybdenum sulfide was produced by slow precipitation (within 2 h) of molybdenum hydroxide from the 0.001 M $MoSO_2$ aqueous solution and sodium hydroxide solution, with constant magnetic stirring. As a result, following chemical processes were proceeded sequentially:

$$MoSO_2 + 2NaOH = Mo\,(OH)_2\downarrow + Na_2SO_2$$
$$Mo\,(OH)_2 + O_2 = H_2O + MoOOH\downarrow$$

Upon completion of the synthesis, a stable suspension of oxide hydroxide molybdenum was formed. Qualification of sedimentation stability of the slurry revealed that the obtained particles of oxide hydroxide molybdenum were not coagulated for 48 hours. This is due to the formation of micellar positively charged particles. Evaluation of zeta potential determined by a moving boundary has shown that the value of the zeta potential is 54 mV. The value of zeta potential clearly indicates that the processes of coagulation are not characteristic for the obtained particles in aqueous suspensions due to the predominance of the processes of repulsion between them [14].

In Figure 1, a micrograph of obtained layers of molybdenum disulfide deposited on a silicon substrate is presented. Treated disulfides are nanolayer powder and the particles of the obtained samples have a spherical shape. Particle size distribution has bimodal distribution: from 0.1 to 0.2μm with a maximum at 0.15 – 0.18 μm; from 0.4 to 5.0 μm, with a maximum of 3.0 μm.

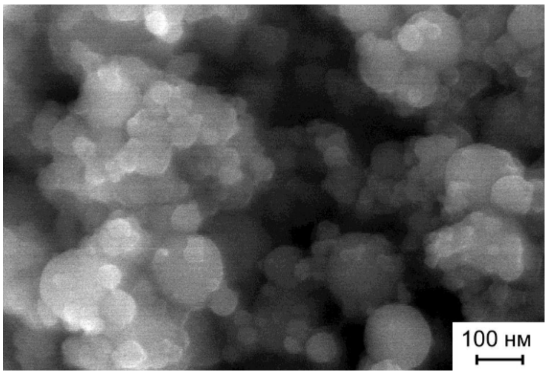

Figure 1 − A micrograph of molybdenum disulfide particles deposited on a silicon substrate, x20.

In Figure 2, the Raman spectrum of molybdenum disulfide is shown. The increased intensity of the peaks in the spectrum of a molybdenum disulfide indicates an elongated crystal structure. The peaks at ~ 388 and 407 cm^{-1} correspond to the vibration modes $E^1_{2g}$and E_{1g} .

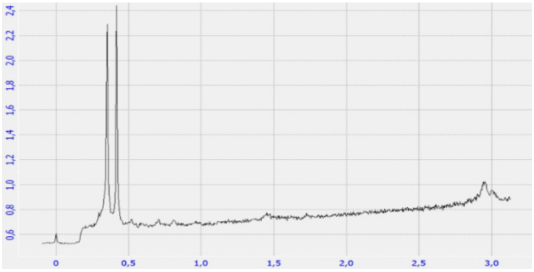

Figure 2 − Raman - spectrum of molybdenum disulfide on a silicon substrate.

In Figure 3, the X-ray diffraction analysis of samples at various excess of sulfur in the initial mixture with the powder of molybdenum is shown. It can be seen that in the composition of particles molybdenum oxide, oxide hydroxide molybdenum and predominant content of molybdenum sulphide phase are present and the main phase is a hexagonal disulfide with a space group of symmetry P63 / mmc. Molybdenum disulphide with a hexagonal crystal lattice is marked with characteristic reflexes of planes (002), (101), (103), (006), (110), (108). In addition, phase of rhombohedral MoS_2 is present in the sample. Unfortunately, according to XRD phase of elemental sulfur is not determined, this is connected either with its small amount, or with its X-ray amorphous state. From the XRD, it is shown that with increasing the excess of sulfur, the intensity and number of phase reflections are reduced and in the sample with 15% excess of sulfur it is not observed, which indicates the completeness of the conversion of initial mixture into the molybdenum disulfide.

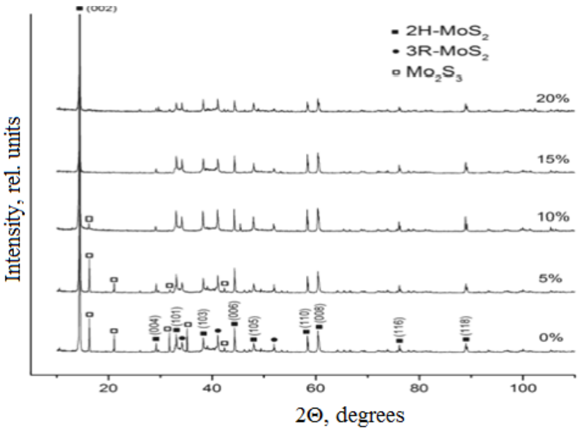

Figure 3 − XRD analysis of the samples at various excess of sulfur in the initial mixture with the powder of molybdenum.

Taking into the account that the process of synthesis takes place on the surface of the particles, the released sulfur gradually blocks surface of the particles. As a result, a process of gradual deceleration of the formation of molybdenum sulfide is observed. As a result, the particles are formed comprising a core of oxide hydroxide molybdenum covered by molybdenum sulfide film, and on the surface of which elemental sulfur is. This hypothesis is partially confirmed by X-ray diffraction data of the particles extracted from the solution, the results of which are shown in Table 1.

Table 1–X-ray diffraction data for the MoS_2– particles

Phase	Phase content, % wt	The size of coherent scattering, nm
MoS_2	68	30
MoO_2	22	123
$MoOH_3$	10	-

The increased peak intensity in the (002) on diffraction patterns of molybdenum disulfide indicates an elongated crystal structure (Figure 4). The results of X-ray diffraction analysis indicate that at least 95% of metal disulphide is contained in the final products of synthesis.

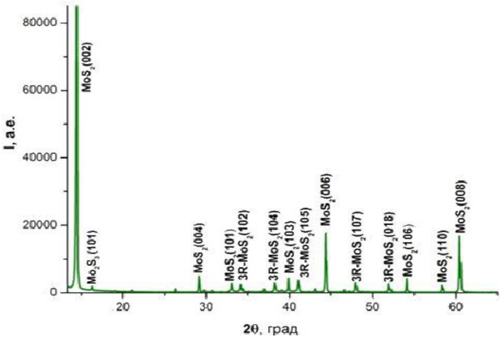

Figure 4 – X-ray image of molybdenum disulfide.

According to XRD data, the disulfide particles have an extended form, a layered structure, and the main phases are hexagonal disulfide with space group of symmetry P63 /mmc. Parameters of crystal lattice for hexagonal MoS_2 are a = 3.161 Å, c_1 = 12.27 Å, and for rhombohedral c_2 = 18.35 Å.

From the obtained data, it is clear that mostly molybdenum sulfides and disulfides with the presence of residual amounts of molybdenum oxide are formed by the proposed method of synthesis. This composition of obtained samples has a possibility to be used for photovoltaic cells.

Conclusions

1. As a result of the proposed procedure for obtaining molybdenum sulfides by sol-gel technology, sulfides and molybdenum disulfides with the presence of residual amounts of molybdenum oxide are formed.
2. The obtained disulfide particles have an extended form, a layered structure, and the main phases are hexagonal disulfide with space group of symmetry P63 / mmc.
3. An increase of the sulfur content in the mixture during the synthesis of nanostructured molybdenum disulfide reduces the rate and maximum temperature of combustion. Upon excess of more than 15% sulfur by weight mainly the phase of hexagonal molybdenum disulfide is observed in the product.
4. The value of the electrokinetic potential is 54 mV, according to zeta potential it clearly indicates that the processes of coagulation are not characteristic for the obtained particles in aqueous suspensions due to the predominance of the processes of repulsion of the particles.

MoS_2 has been triggering a new wave of research and far from being exhausted. Recently, stable preparation high quality MoS_2 in large area for applications in industrial-scale is still challenging. Research on van der Waals heterostructures reassembling has emerged over the past three years, while the interfacial contact between each building layer needs to be further optimized. In addition, the band engineering of MoS_2, achieving composite constructions with superior electrical performance and tunable band structure, is a leading topic in the near future [13].

References

1. Ray S. C. Structure and optical properties of molybdenum disulphide (MoS_2) thin film de-posited by the dip technique // Journal of materials science letters. – 2000. – Vol. 19. – P. 803-804.

2. Ganatra R, Zhang Q. Few-layer MoS_2: a promising layered semiconductor // ACS Nano. – 2014. – Vol.8. – P. 4074-4099.

3. Wi S, Kim H, Chen M, Nam H, Guo LJ, Meyhofer E, et al. Enhancement of photovoltaic response in multilayer MoS_2 induced by plasma doping // ACS Nano. – 2014. – Vol. 8. – P. 5270-5281.

4. Ding S, Zhang D, Chen JS, Lou XW. Facile synthesis of hierarchical MoS_2 microspheres com-posed of few-layered nanosheets and their lithium storage properties // Nanoscale. – 2012. – Vol.4. – P.95-98.

5. Li Y, Wang H, Xie L, Liang Y, Hong G, Dai H. MoS_2 nanoparticles grown on graphene: an advanced catalyst for the hydrogen evolution reaction // Journal of the American Chemical Society. – 2011.– Vol. 133. – P. 7296-7299.

6. Wu W, Wang L, Li Y, Zhang F, Lin L, Niu S, et al. Piezoelectricity of single-atomic-layer MoS_2 for energy conversion and piezotronics // Nature.– 2014.– Vol. 514. – P.470-474.

7. Klimenko I.V., Zhuravleva T.S., Lenenko N.D., Zhuravleva Yu.V. Vliyanie rastvoritelya na obrazovanie I spektry pogloshenіya nanodispers-

nogo disulfidamolibdena // Zhurnal physichesko i himii. − 2009. − Vol. 83. − P. 346-350.

8. Radisavljevic B, Radenovic A, Brivio J, Giacometti V, Kis A. Single-layer MoS_2 transistors // National Nanotechnology. − 2011. − Vol. 6. − P. 147-150.

9. Wang H, Liu F, Fang Z, Zhou W, Liu Z. Two-dimensional hetero-structures: fabrication, characterization, and application // Nanoscale.− 2014. −Vol. 6. − P. 12250-12272.

10. Ma Y, Dai Y, Guo M, Niu C, Huang B. Graphene adhesion on MoS_2 monolayer: an ab initio study // Nanoscale. − 2011. − Vol. 3. − P.3883-3887.

11. Bernardi M, Palummo M, Grossman JC. Extraordinary sunlight absorption and one nanometer thick photovoltaics using two-dimensional monolayer materials // Nano Letters. − 2013. − Vol. − P. 3664-3670.

12. Hong X, Kim J, Shi SF, Zhang Y, Jin C, Sun Y, et al. Ultrafast charge transfer in atomically thin MoS_2/WS_2 heterostructures // National Nanotechnology. − 2014. − Vol. 9. − P. 682-686.

13. Xiao Li, Hong wei Zhu. Two-dimensional MoS_2: Properties, preparation, and applications // Journal of Materiomics. − 2015. − Vol. 1. − P.33-44

14. Harnutova E.P., Petrov E.I. Synthessulfidov d-metallov I, II I VIII grupp periodicheskoi sistemy vzhidkih n-alkanah // Journal Materials Research. − 2004. − Vol. 19, – No 7.− P. 1924.

International Journal of Mathematics and Physics 7, №2, 76 (2016)

UDC 539.12.04; 539.1.08

Naurzbayeva A.Zh., Alimgazinova N.Sh., Oskomov V.V., *Saduyev N.O.,
Kalikulov O.A., Kenzhina I.E., Zhumabaev A.I., Iskakov B.A., Shinbulatov S.

Institute of Experimental and Theoretical Physics,
al-Farabi Kazakh National University, Almaty, Kazakhstan
*e-mail: lvcl@mail.ru

Study of anisotropy of extremely high energy cosmic rays

Abstract. The article shows investigations of anisotropy of high energy cosmic rays.We calculated the number of cosmic rays (events) of extremely high energies with different threshold energy, the direction of arrival of which lies on the angular distances from the active galactic nuclei, not large than given. Similar calculations were also carried with maximum of one hundred numerical experiments of concentrating around active galactic nuclei isotropic distribution of particles. For interval to ~3^0 in all cases, except for a local minimum at ~2^0 for distance <100 Mpc, these values were less than the observed in real distribution. Thus, our results indicate a clear correlation between the arrival directions of cosmic rays of extremely high energy and direction to close (within 100 Mpc) to the solar system active galactic nuclei, therefore, these objects are one of the real sources of such particles.

Key words: anisotropy, cosmic rays, galactic nuclei, isotropic distribution, galaxy

Introduction

Cosmic ray particles with energies more than 40EeV are called particles of extremely high energy (or ultra high energy). The complexity of such studies is that their intensity is very low, for example, the flux of cosmic rays with an energy of about 100 EeV is only 1 particle/(100 km^2 year).It is the reason why less than 100 of such particles have been registered, until 2000 in all over the world.

Since 2004, the installations of cosmic rays registration of Pierre Auger Observatory were started to operate. They registered particles of ultra-high energies, the square of each area were about 3,000 km^2, with an angular resolution of about 1%, and an energy resolution of ~ 10%. These parameters give the possibility to register for 10 years, more than two hundred of extensive air showers (EAS) generated by ultra-high energy particles of cosmic rays that allowed us to obtain a lot of new valuable information about their origin. Despite this, the issue of sources of ultra-high energy particles of cosmic rays still remains open. The most likely candidates for this role are being considered are active galactic nuclei.

In connection with the above, in the present work new observational data obtained in Pierre Auger Observatory were used. The correlation between the arrival directions of ultra-high-energy particles and directions to the closest solar system, galaxies with active nuclei were investigated.

In addition of Pierre Auger Observatory data of energies and coordinate axes of extensive air showers from cosmic rays particles of extremely high energies, we used data on the equatorial coordinates and redshifts of active galactic nuclei presented in Swift-BAT directory, which includes sources that are registered for 70 months of observations by BAT-detector of hard X-ray radiation on Swift satellite board [1].

Instruments and methods

Figure 1 shows the distribution at the celestial sphere of coordinates on the arrival of cosmic ray particles with extremely high energies by measuring of Pierre Auger Observatory and galaxies with active nuclei of Swift-BAT 70-month X-ray catalog in equatorial coordinates.

Using these data, we calculated the number of cosmic rays (events) of extremely high energies with different threshold energy, the direction of arrival of which lies on the angular distances from the active galactic nuclei, not large than given. The angular distance varied from 0.6^0 to 10^0 in increments of 0.2^0, the threshold energy were taken to be 50 and 60 EeV, for these values the amount of rainfall is still ensures a sufficient statistic. Calculations were made for active galactic nuclei with different maximum heliocentric distance to them: from 40 to 100 Mpc. Galaxies, which were lying at great distances, were not considered as due to the interaction of cosmic rays of extremely high energy with microwave background radiation of the Universe, particles with such distances should not reach the observer (blackbody cutoff of cosmic rays spectrum, Greisen – Zatsepin – Kuzmin effect (GZK effect)). To estimate the excess of particles at small angular distances from active galactic nuclei (i.e. directions concentration of their arrival around active galactic nuclei) the ratio particles number were calculated in the observed distribution with their numbers in isotropic distribution at the same other conditions (the same total number of particles, the same angular distance, the maximum distance from active galactic nuclei, etc.).In calculating the number of particles concentrating around active galactic nuclei in isotropic distribution, we took the average value of that number of hundreds numerical experiments results on the generation of random uniform distribution. The results of this study are shown in Figures 1-5.

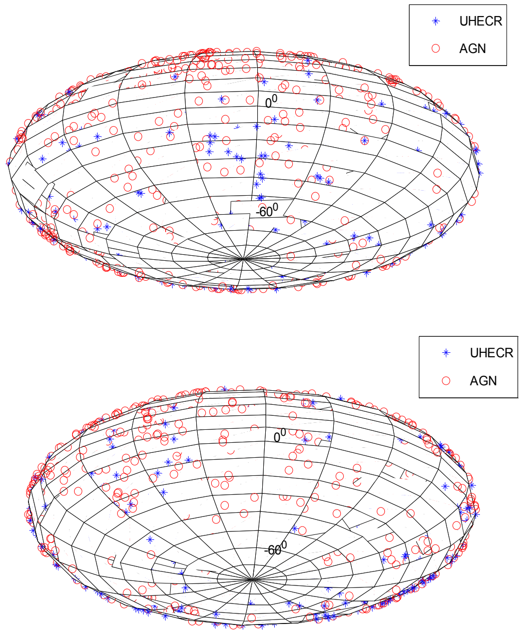

Figure 1 – Distribution of arrival directions of cosmic ray particles with energies $E>5\cdot10^{19}$eV on celestial sphere on measurements of Pierre Auger Observatory and galaxies with active nuclei of Swift-BAT 70-month X-raycatalog in equatorial coordinates (hemisphere of spring equinoxes points (a) and autumn equinoxes points (b))

From figures it is clear that the number of observed events within ~30 of active galactic nuclei exceeds the number of those for isotropic distribution, it is particularly clearly seen in the case of smaller distances to active galactic nuclei. The fact that this excess is greater the closer you are to the considered active galactic nuclei, can be explained by the influence of GZK effect. At an angular distance of ~20 in considered dependence in nearly all cases there is a local minimum, and we do not have assumptions about the reason for its occurrence.

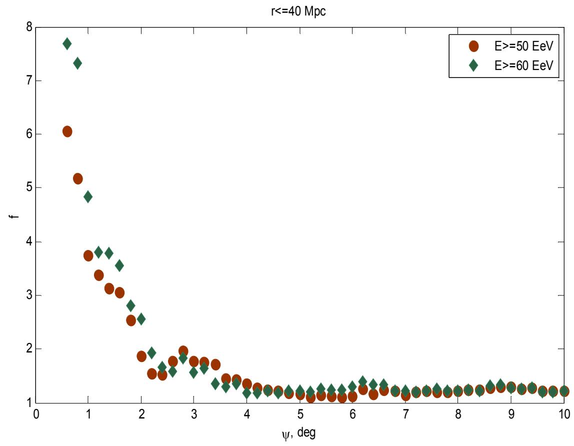

Figure 2 – Dependence of excess of events from the angular distance to active galactic nuclei, located closer than 40 Mpc, for different threshold energies

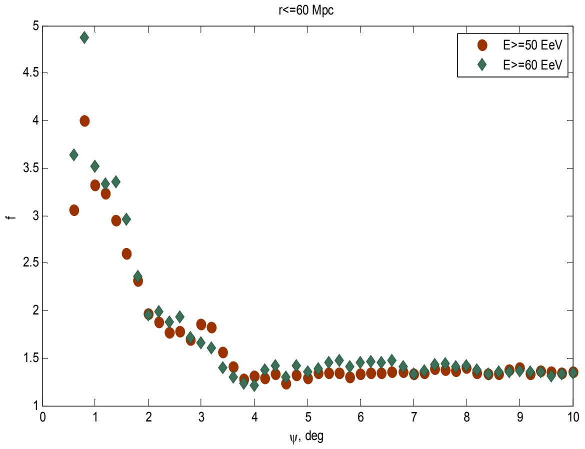

Figure 3 – Dependence of the excess of events from angular distance from the activegalactic nuclei that are closer than 60 Mpc, for different threshold energies

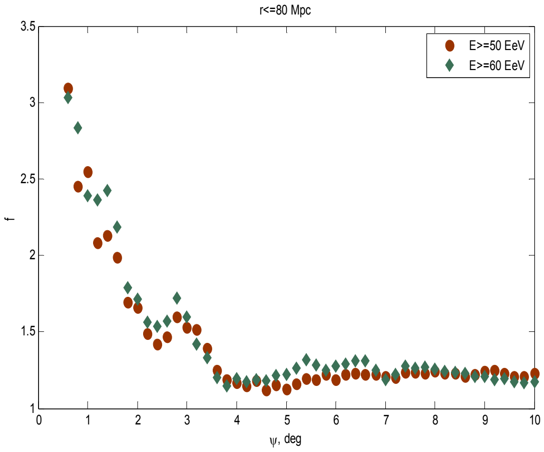

Figure 4 – Dependence of the excess of events from angular distance from the active galactic nuclei that are closer than80 Mpc, for different threshold energies

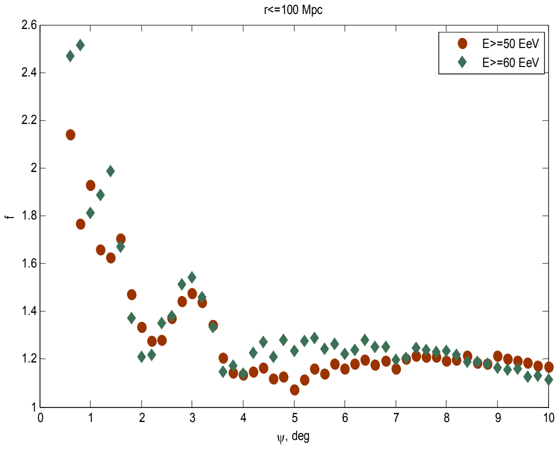

Figure 5 – Dependence of the excess of events from angular distance from the active galactic nuclei that are closer than100 Mpc, for different threshold energies

Conclusion

Similar calculations were also carried with maximum of one hundred numerical experiments of concentrating around active galactic nuclei isotropic distribution of particles. For interval to ~3^0 in all cases, except for a local minimum at ~2^0 for distance <100 Mpc, these values were less than the observed in real distribution.

Thus, our results indicate a clear correlation between the arrival directions of cosmic rays of extremely high energy and direction to close (within 100 Mpc) to the solar system active galactic nuclei, therefore, these objects are one of the real sources of such particles.

It is necessary to note that our results are qualitatively consistent with for example, [2-4].

Acknowledgments

The study was carried out under the support of grant #3842/GF4 of Ministry of Education and Science of Kazakhstan.

References

1. Baumgartner, W. H., Tueller, J., Markwardt, C. B., et al. The 70 Month Swift-BAT All-Sky Hard X-Ray Surve // Astrophysical journal supplement series. – 2013. – Vol. 207. – P. 19.
2. Aab A. Searches for Anisotropies in the Arrival Directions of the Highest Energy Cosmic Rays Detected by the Pierre Auger Observatory // The Astrophysical Journal. – 2015. – Vol. 804. – P.15.
3. Abreu P. et al. A search for anisotropy in the arrival directions of ultra high energy cosmic rays recorded at the Pierre Auger Observatory // JCAP – 2012. – Vol. 04. – P. 040.
4. Uryson A.V. Kosmicheskie luchipredel'no vysokih jenergij: otozhdestvlenie vozmozhnyh istochnikov, jenergeticheskij spektr, rasprostranenie. // Fizikaj elementarnyh chastici atomnogo jadra. – 2006. – P. 652-694.

International Journal of Mathematics and Physics 7, №2, 79 (2016)

UDC 539.17

[2]Burtebayev N., [1,2*]Mukhamejanov Y.S., [1,2]Alimov D.K.,
[2]Kerimkulov Zh.K., [3]Janseitov D.M., [4]Trzaska W.H.

[1]Physics and Technology Department, al-Faraby KazNU, Almaty, Kazakhstan,
[2]Institute of Nuclear Physics, Almaty, Kazakhstan,
[3]Physics and Technology Department, Eurasian National University, Astana, Kazakhstan
[4]University of Jyväskylä, Jyväskylä, Finland
[*]e-mail: y.mukhamejanov@gmail.com

Comparative analysis of elastic and inelastic scattering of d and α-particles from ^{11}B

Abstract. Experimental angular distributions of elastic and inelastic scattering of deuterons at E_d=14.5 MeV and alpha particles at E_α=29, 40.5 and 50.5 MeV from nuclei ^{11}B were measured on the extracted beam of isochronous cyclotron U-150M at the Institute of Nuclear Physics (Almaty, Kazakhstan) within angular range of 10-150 degrees in laboratory system. The analysis of experimental data on elastic scattering of deuterons and alpha particles from ^{11}B nucleus was made within the optical model and double folding model with literature data at different energies of the incident particles. The analysis of experimental data on inelastic scattering of deuterons and alpha particles from ^{11}B nucleus was made within the coupled channels method. The calculations were made using FRESCO computer code. The radii of the $1/2^-$ (2.125 MeV), $5/2^-$ (4.445 MeV), $7/2^-$ (6.742 MeV) and "exotic" $3/2^-$ (8.56 MeV) states of ^{11}B were determined within the modified diffraction model. As a result of the analysis, the optimal parameters of the phenomenological optical potentials and double folding potentials were determined for ^{11}B+d and ^{11}B+α systems.

Key words: deuterons, α-particles, optical model, double folding, modified diffraction model, nuclear radii, fresco.

Introduction

Study of elastic and inelastic scattering processes of light charged particles, such as deuterons and alpha particles, is one of the main sources of the information about the nuclear potentials, which are used to calculate the wave functions describing the relative motion of the colliding particles, as well as information about the properties of ground and low lying excited sates of nuclei. These processes take place during collisions of alpha particles at energies of tens of MeV and allow obtaining highly valuable information about the structural characteristics of nuclei, such as deformation parameters and nuclear radii. So called direct transitions from initial to some final state of the nucleus without any intermediate processes usually take place at mentioned energies. This is the reason why those kinds of transitions are the most convenient tool for receiving spectroscopic information about properties of various states of nuclei. This is due to the fact that direct mechanism as is dominates in direct processes and they do not mix much with more complex reactions and do not cause mixing of numerous excited states. For this reason elastic and inelastic processes quite selectively excite single-particle and quasi-hole as well as different types of collective states. That is why they are called the most pure method of studying mentioned states.

Of particular interest from the point of view of studying excited neutron halo-states of light nuclei are the states of ^{11}B nucleus, where both "exotic" cluster configuration (2α+t), and the shell model structure can co-exist at the same time. Indeed, several studies have suggested that low-lying states of ^{11}B, basically, have a shell structure, while the cluster structures are easily traced in the states with negative parity above or near the threshold of breakup into clusters.

Experimental details

The experiment was carried out at U-150M cyclotron at the Institute of Nuclear Physics Institute of Nuclear Physics (INP) (Almaty, Kazakhstan) which allows to accelerate protons up to 30 MeV, deuterons up to 25 MeV, ^{3}He up to to 60 MeV and alpha-particles up to 50 MeV. Charged particles in cyclotron are formed in source, located in the central part of camera in an arc discharge when supplying corresponding gas (hydrogen, deuterium, helium-3, helium-4). They are accelerated in the interpolar space of 1.5-meter magnet when particles fly between the dees.

Transportation scheme of accelerated ions beam from a cyclotron chamber to the scattering chamber, located at 24 meters away from the beam is shown in Figure 1. It includes a quadruple lens system, two bending, separating, two targeting magnets and collimators system. All these setups with the targeting and correction elements provide a charged particles beam at the target with angle spread not more than 0,4° and 3 mm in diameter. Adjusting positions of the collimator and the center of scattering chamber with respect to the ion guide axis was carried out by optical method and controlled by means of a 12-quartz screens and television cameras that transmit image to the cyclotron remote control.

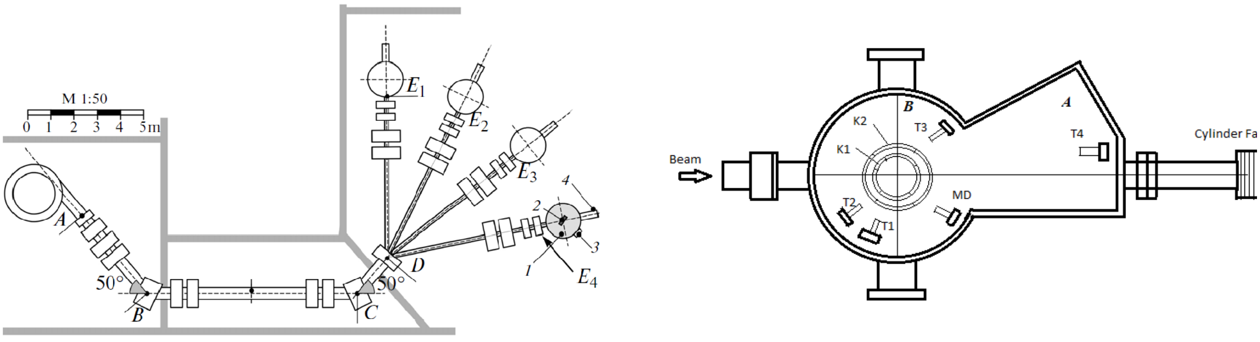

a

b

A, B, C, D, and E are the characteristic points and the accelerated ion beam bending points; (1) scattering chamber; (2) target; (3) rotating scattered particle detector; (4) Faraday cup.

K_1 and K_2 – independently rotating rings with step engine drives; T_1-T_4 – telescopes of E-ΔE detectors attached to K_1 and K_2; MD – detector for monitoring scattered beam

Figure 1 – (a) U-150M isochronous cyclotron with adjustable ion energy and the ion beam transport line to the scattering chamber. (b) Scattering chamber

Vacuum scattering chamber (60 cm in diameter) was used for measurements of angular distributions of nuclear reactions products with charged particles (Figure 2).

The chamber, made of stainless steel, consists of hollow cylinder B with internal diameter of 715 mm, 370 mm height and so called “pocket” A which is an additional volume extended along beam direction. There are three (E-ΔE) telescopes of silicon semiconductor detectors, which cover the scattering angles of 10–70° in the main volume B of the chamber. A fourth telescope with independent drive, designed for covering the measurements in the angular range of 2–20° is located in volume A. Considerable distance from the target (1000 mm) allows to reduce 10–15 times the load on detecting apparatus due to the elastic scattering measurements at extremely small angles. Monitoring window with a diameter of 290 mm located on the top cover of the chamber allows visual inspection of the experimental situation (angles of the telescopes, the state of the target, etc.).

For optimal focusing of the accelerated ^{4}He ions on the target, two collimators of diameter 2 mm were used. Pumping system which includes a high-vacuum turbo molecular pumps and pre-evacuation was tested and showed good results in achieving high vacuum inside the chamber of about 2.3x 10^{-6} Pa.

Targets were thin metal foils made of boron-11 isotope. ^{11}B isotopes were sputtered on a glass by electron sputtering method on VUP-5 setup. The foil was later taken off the glass on a surface of distilled water by dissolving intermediate salt layer.

Target thickness was determined at linear accelerator UKP-2-1 at INP. For determining the thickness of boron $^{27}Al(p,\gamma)^{28}Si$ reaction yield curves in the region of resonance at E_p=992 keV [1] were measured using aluminum foil and the sputtered target. The shift of this resonance in the

$^{27}Al(p,\gamma)^{28}Si$ reaction due to protons energy loss while passing ^{11}B film was 62.0 keV which responds to the target thickness equal to 320 μg/cm^2. This method allowed determining target thickness with accuracy not more than 5%.

The (*E-ΔE*) method was used in the registration and identification of reactions products. The method is based on simultaneous measurement of specific energy losses of charged particles in matter (*dE*/*dx*) and the total kinetic energy *E*. In the telescope of detectors "*E-ΔE*", *ΔE* - detector is a surface-barrier silicon detector- company ORTEC- thick active layer of 30 to 200 μm with thin inlet (~ 40μg/cm^2 Au) and outlet (~40μg/cm^2 Al) windows. The complete absorption *E* detector is used as a stop detector- company ORTEC high-purity silicon; thickness of 2 mm.

Elastic scattering

The analysis of elastic scattering of deuterons and alpha particles from ^{11}B nuclei including literature data at E_d=11.8, 13.6 and 27.7 MeV [2-4] and E_α=40.5, 50.5 [5], 48.7 [6] and 54.1 MeV [6] was made within both phenomenological optical model (OM) and semi-microscopic double folding (DF) model using computer code FRESCO [7]. Within phenomenological approach elastic scattering is described by complex radius dependent Woods-Saxon shaped interaction potential:

$$U(r) = -\,V\,f\,(x_V) - i\,[Wf(x_W)] + V_{\,C}(r), \quad (1)$$

where $f(x_i) = (1 + \exp(x_i))^{-1}$, $x_i = (r - R_i)/a_i$, $R_i = r_i A^{1/3}$, $V_C(r)$ – Coulomb potential of uniformly charged sphere with radius $R=1.28A^{1/3}$ fm, V – depth of real part of the potential, W – depth of the imaginary part of the potential, r and a are the values of radius and diffuseness, respectively. Taking into account compact size of the incident particle, we while analyzing the data at high energies limited with volume type of absorption potential for the imaginary part. The results of the comparison of calculated values of differential cross sections with the experimental angular distributions are given in Figure 3.

It is common to use the folding model to calculate the real potential and to use a Woods-Saxon (WS) form for the imaginary potential. Given correct nuclear densities as inputs for the DF calculation, it remains necessary to have an appropriate in-medium NN interaction for a reliable prediction of the (real) nucleus–nucleus OP. Most of the 'microscopic' nuclear reaction calculations so far still use different kinds of the effective NN interaction. Very popular choices have been the so-called M3Y interactions which were designed to reproduce the *G*-matrix elements of the Reid [8] and Paris [9] free NN potentials in an oscillator basis (further referred to as M3Y-Reid and M3Y-Paris interaction, respectively). The original M3Y interaction is density independent and given in terms of the Yukawa functions as follows:

M3Y-Reid:

$$v_D(s) = 7999.0\frac{\exp(-4s)}{4s} -$$

$$-2134.25\frac{\exp(-2.5s)}{2.5s}, \quad (2)$$

$$v_{EX}(s) = 4631.38\frac{\exp(-4s)}{4s} -$$

$$1787.13\frac{\exp(-2.5s)}{2.5s} - 7.8474\frac{\exp(-0.7072s)}{0.7072s},$$

M3Y-Paris:

$$v_D(s) = 11061.625\frac{\exp(-4s)}{4s} -$$

$$-\,2537.5\frac{\exp(-2.5s)}{2.5s}, \quad (3)$$

$$v_{EX}(s) = -1524.25\frac{\exp(-4s)}{4s} -$$

$$-\,518.75\frac{\exp(-2.5s)}{2.5s} - 7.8474\frac{\exp(-0.7072s)}{0.7072s},$$

The Yukawa strengths in equations (2) and (3) are given in MeV, and *s* is the distance between the two interacting nucleons. These interactions, especially the M3Y-Reid version, have been used with some success in the DF model calculations for the interaction between heavy ions (HI) at low energies [10], with the elastic data usually limited to the forward scattering angles and, thus, sensitive to the OP only at the surface. The inclusion of an explicit density dependence was needed to account for a reduction in the strength of the nucleus–nucleus interaction that occurs at small *R* where the overlap density of the nuclear collision increases. An early version of the density dependence of the M3Y-Reid interaction was constructed by Kobos *et al* [10] based upon the *G*-matrix results obtained by Jeukenne *et al* [11]. It was dubbed as the DDM3Y interaction and has been used to improve the folding model description of the elastic α-nucleus [11-13] and light HI [14] scattering. The obtained parameters of potentials are given in Table 1. The comparison of experimental differential cross sections of elastic scattering of deuterons and alpha particles with the calculations within OM and DF are given in figures 2 and 3.

Table 1 – Parameters of optical and folding potentials for deuterons scattering from ^{11}B nuclei

E_d MeV	Potential set	V MeV	r_v fm	a_v fm	N_r	W MeV	r_w fm	a_w fm
11.8	OM	72	1.17	0.845		13.0	1.322	0.509
	DF				0.80	17.0	1.211	0.519
13.6	OM	80.70	1.17	0.993		13.50	1.322	0.459
	DF				0.80	15.5	1.225	0.459
14.5	OM	86.8	1.17	0.993		17.50	1.322	0.505
	DF				0.80	15.5	1.250	0.455
27.7	OM	83.13	1.17	0.845		16.251	1.322	0.512

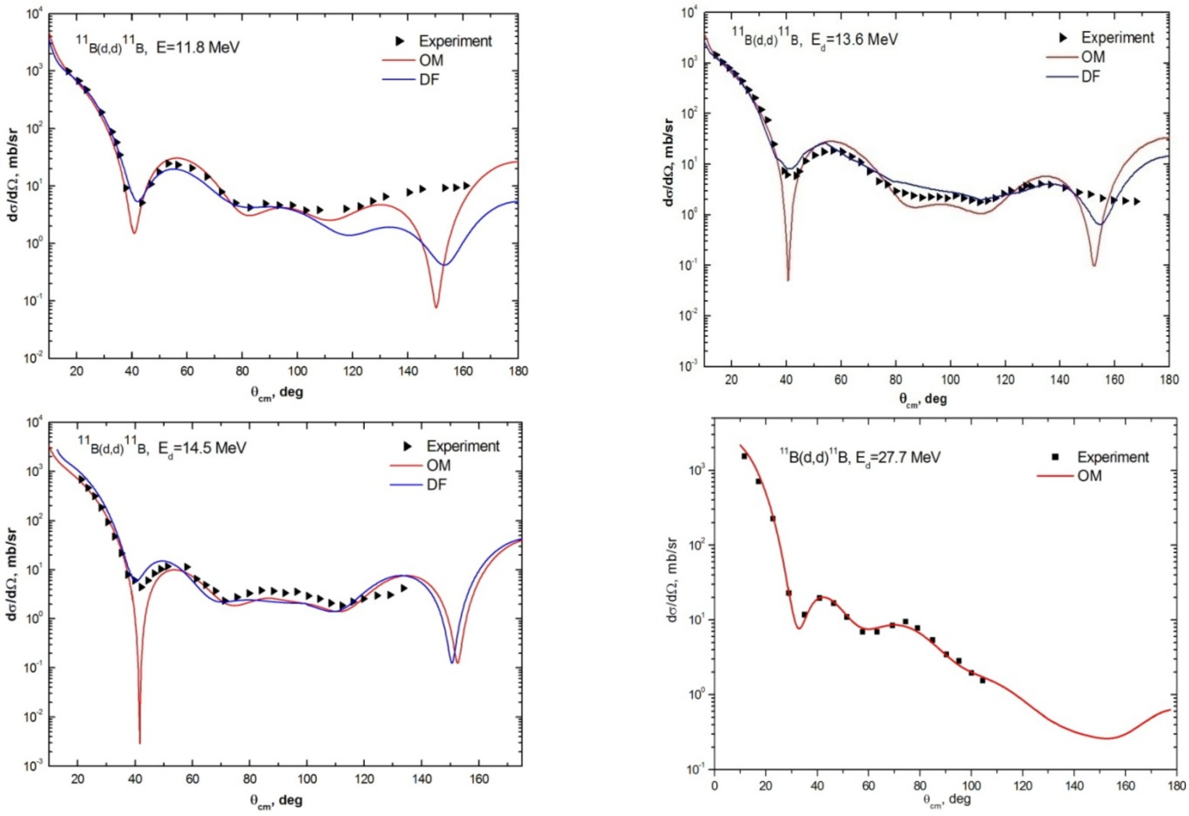

Symbols – experimental data for elastic scattering; solid curves – calculations within OM and DF.

Figure 2 – Angular distributions of elastic scattering of deuterons from ^{11}B nuclei at energies 11.8, 13.6 and 14.5 MeV in comparison with calculated differential cross sections

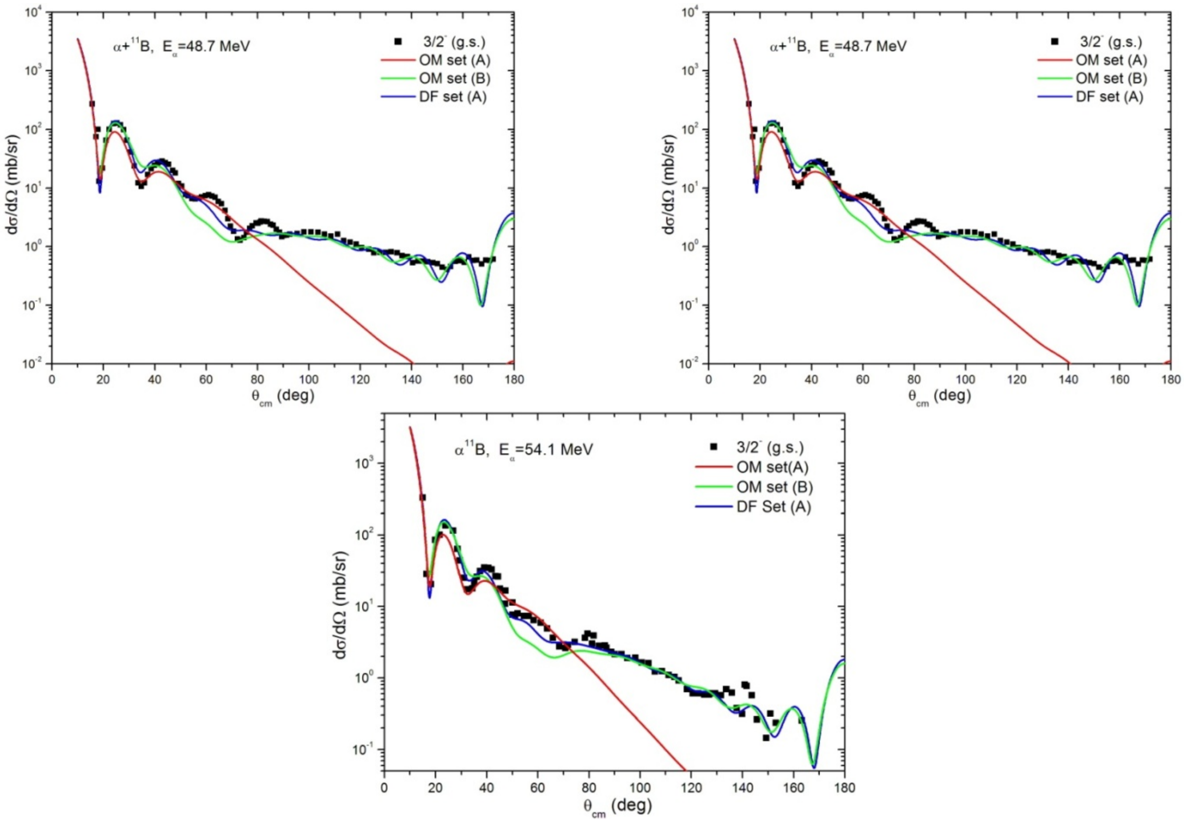

Symbols – experimental data for elastic scattering; solid curves – calculations within OM and DF.

Figure 3 – Angular distributions of elastic scattering of alpha particles from ^{11}B nuclei at energies 48.7, 50.5 and 54.1 MeV in comparison with calculated differential cross sections

Table 2 – Parameters of optical and folding potentials for deuterons scattering from ^{11}B nuclei

E MeV	Potential set	V_o MeV	r_v fm	a_v fm	Nr	W MeV	r_w fm	a_w fm	J_V MeV fm^3	Jw MeV fm^3
48.7	OM A	76.0	1.245	0.825		15.89	1.57	0.801	200	95.4
	OM B	123.0	1.245	0.74		18.91	1.57	0.623	388	106.7
	DF A				1.3	23.32	1.57	0.547		99.01
50.5	OM A	77.22	1.245	0.856		16.85	1.57	0.833	260	102.4
	OM B	120.0	1.245	0.752		18.14	1.57	0.731	381	106.1
	DF A				1.2	18.14	1.57	0.731		
	DF B				1.2	30.0	1.33	0.746		112.9
54.1	OM A	80.73	1.245	0.822		15.08	1.57	0.85	266	92.2
	OM B	125.0	1.245	0.746		19.56	1.57	0.628	396	110.6
	DF A				1.28	23.5	1.57	0.552		113.3

Inelastic scattering

The comparison between the experimental data and theoretical predictions for the $1/2^-$ (2.125 MeV), $5/2^-$ (4.445 MeV), $7/2^-$ (6.743 MeV) and "exotic" $3/2^-$ (8.56 MeV) states at E_d=14.5MeV and E_α=29, 40.5 [4], 50.5[4], 65 [15] MeV are shown in figures 4,5 and 6 respectively. The theoretical calculations of the angular distributions for the different excited states were performed using the coupled channel method implemented in code Fresco using different potential sets. The extracted deformation parameters for the $1/2^-$ (2.125 MeV), $5/2^-$ (4.445 MeV), $7/2^-$ (6.743 MeV) and "exotic" $3/2^-$ (8.56 MeV) states at energies 29, 40 and 50 MeV are listed in table 3

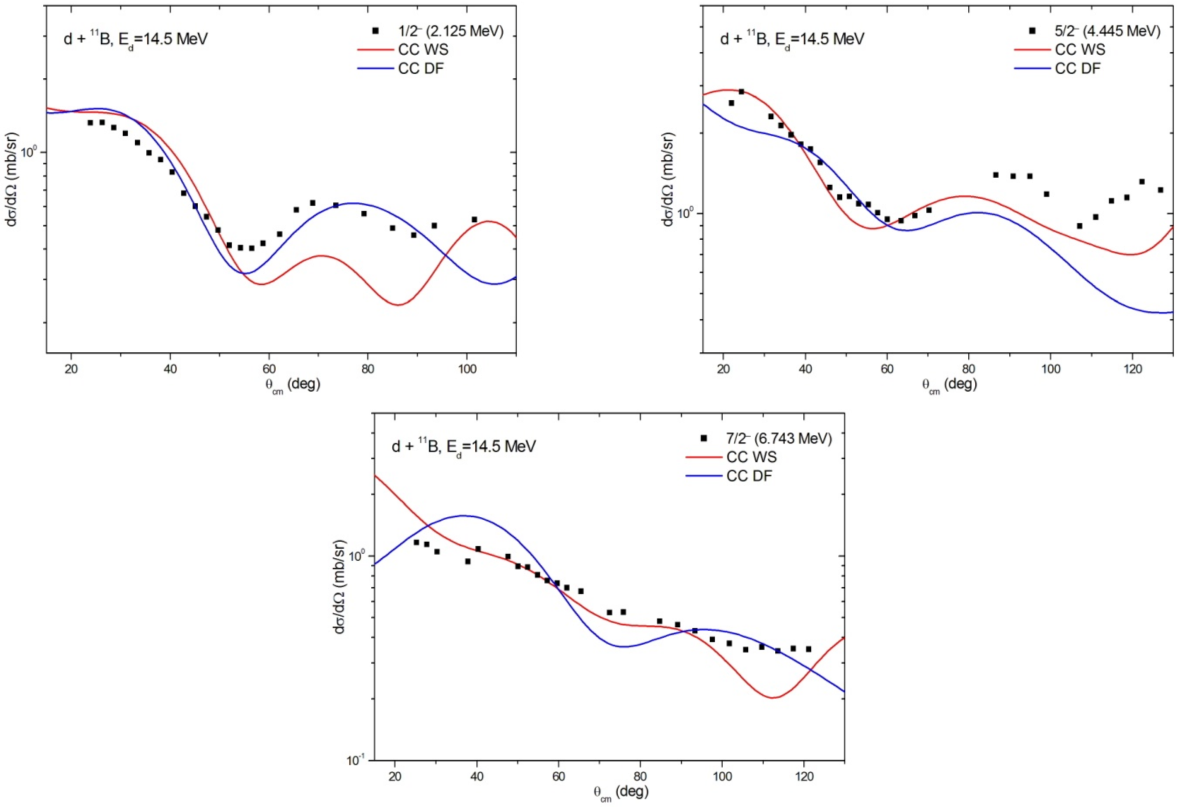

Symbols – experimental data for elastic scattering; solid curves – calculations within CC.

Figure 4 – Angular distributions of inelastic scattering of deuterons from ^{11}B nuclei at E_d=14.5 MeV in comparison with calculated differential cross sections

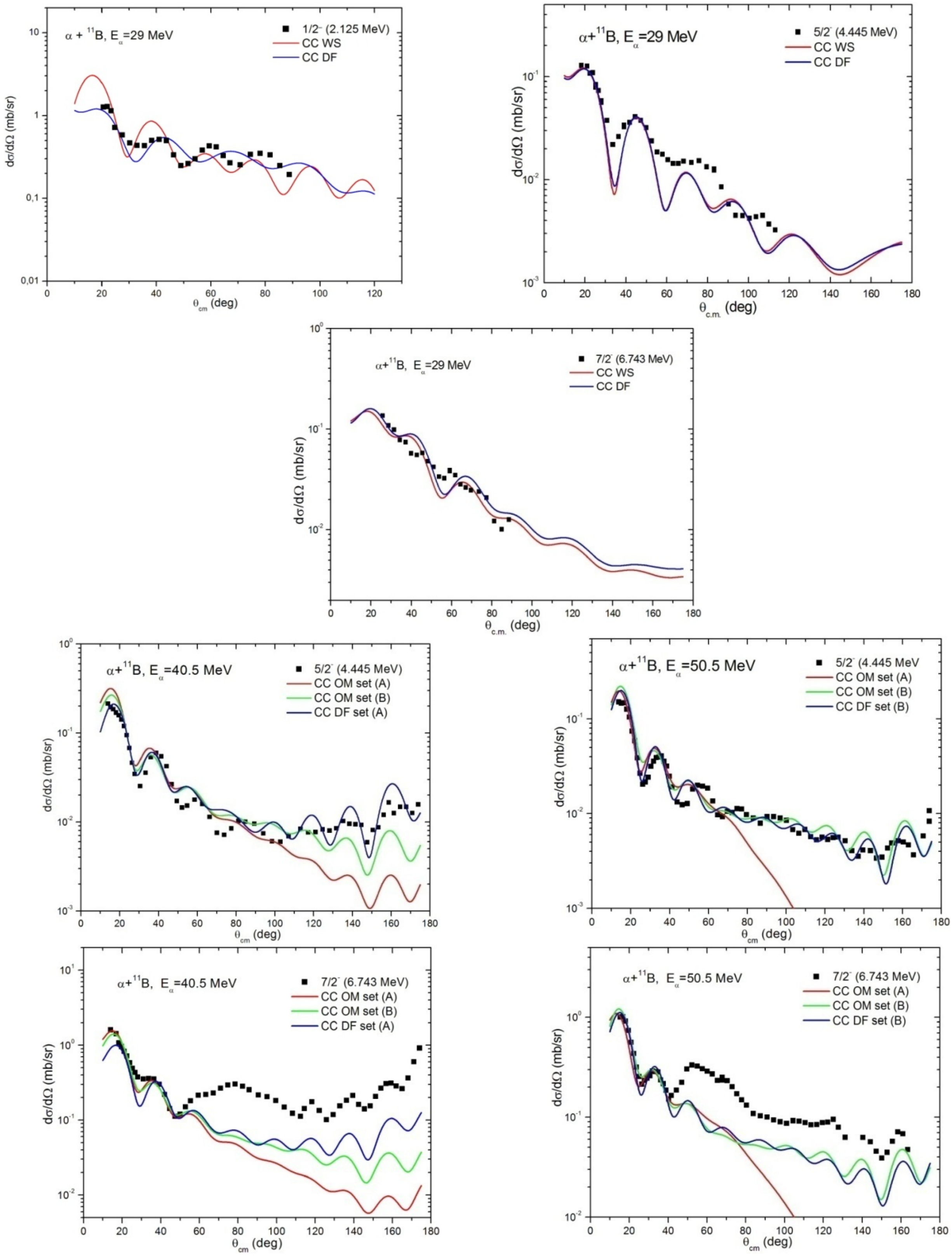

Symbols – experimental data for elastic scattering; solid curves – calculations within CC.

Figure 5 – Angular distributions of inelastic scattering of alpha particles from ^{11}B nuclei at E_α=29, 40.5 and 50.5 MeV in comparison with calculated differential cross sections

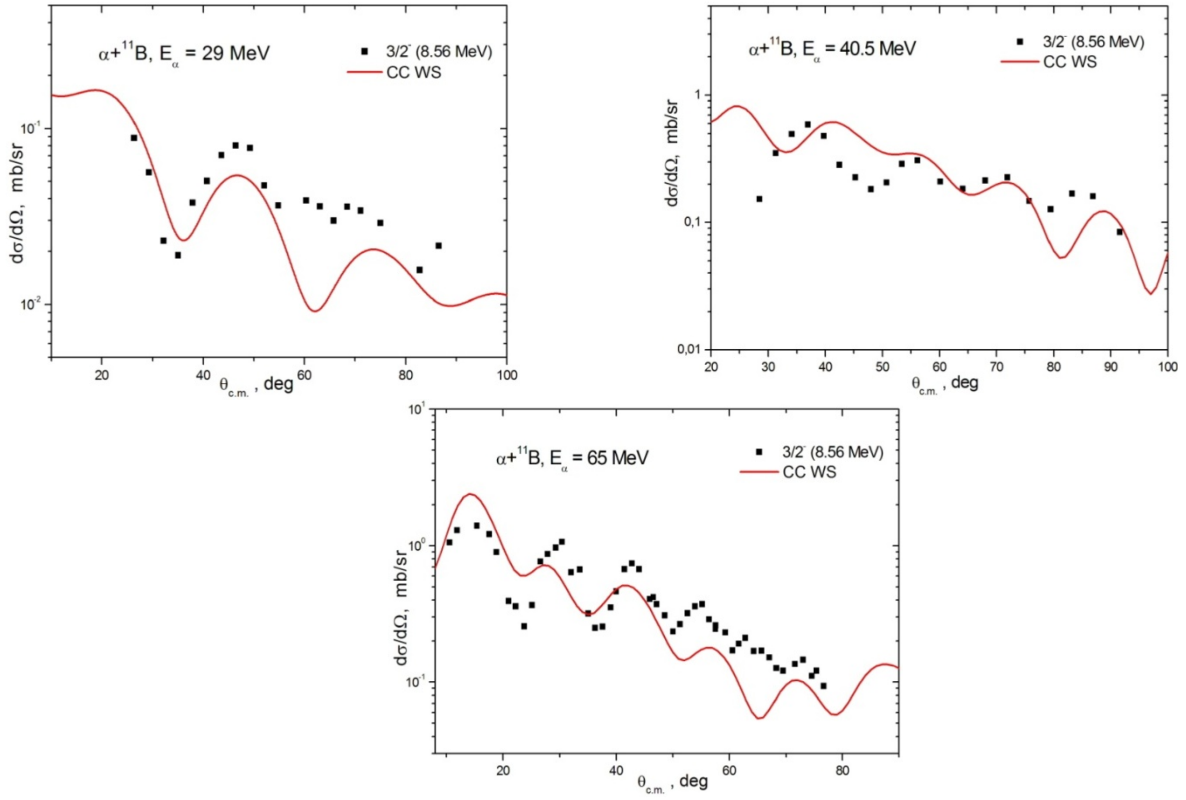

Symbols – experimental data for elastic scattering; solid curves – calculations within CC.

Figure 6 – Angular distributions of inelastic scattering of alpha particles from ^{11}B nuclei at $E_α$=29, 40.5, 65 MeV in comparison with calculated differential cross sections

Table 3 – Deformation parameters of ^{11}B excited states

E_{lab}, MeV	Potential	β (1/2$^-$)	β (5/2$^-$)	β (7/2$^-$)	β (3/2$^-$)
14.5 (E_d)	WS	0.46	0.47	0.47	
	DF	0.47	0.45	0.47	
29 ($E_α$)	WS	0.45	0.46	0.44	0.41
	DF	0.45	0.46	0.44	
40.5 ($E_α$)	WS		0.42	0.42	0.42
	DF		0.4	0.42	
50.5 ($E_α$)	WS		0.35	0.4	
	DF		0.35	0.4	
65 ($E_α$)	WS				0.42

Nuclear radii

The root mean square (rms) radii of 3/2$^-$ (0 MeV), 1/2$^-$ (2.125 MeV), 5/2$^-$ (4.445 MeV), 7/2$^-$ (6.743 MeV) and "exotic" 3/2$^-$ (8.56 MeV) states were estimated within the modified diffraction model (MDM) [16]. This method allows determining rms radius $\langle R^* \rangle$ of the excited state via the difference of diffraction radii of the exited and the ground states using the expression

$$R^* = R_0 + \left[R_{dif}^* - R_{dif}(0)\right] \quad (4)$$

Here R_0 is the rms of the ground state of the studied nucleus, R_{dif}^* and $R_{dif}(0)$ are the diffraction radii determined from the positions of the minima and maxima of the experimental angular distributions of elastic and inelastic scattering correspondingly. The rms radii of $3/2^-$ (0 MeV), $1/2^-$ (2.125 MeV), $5/2^-$ (4.445 MeV), $7/2^-$ (6.743 MeV) states are given in table 4 at E_α=29, 40.5 [5], 50.5 [5] and 65 [15] MeV. The radius of "exotic" $3/2^-$ (8.56 MeV) state was determined at E_α=29, 40.5 MeV. The obtained radii are in fair agreement with the results obtained in other works within MDM[16] and other approaches for determining the radii of excited states, such as antisymmetrized molecular dynamics (AMD) [17] and orthogonality condition model (OCM). The comparison of

Table 4 – Root mean square radii of ground and excited states of ^{11}B, obtained within MDM

E_{lab}, MeV	R_{rms} (0.00), fm	R_{rms} (2.12), fm	R_{rms} (4.445), fm	R_{rms} (5.02), fm	R_{rms} (6.74), fm
29	2.29	2.33±0.10	2.25 ±0.12		2.25 ± 0.15
40.5 [4]	2.29		2.17±0.08		2.22 ± 0.10
50.5 [4]	2.29		2.30±0.15		2.31 ± 0.11
65 [15]		2.37 ±0.20	2.27±0.10	2.44±0.14	2.32 ± 0.14

Table 5 - Root mean square radius of $3/2^-$ (8.56 MeV) state

	MDM (E_α=29 MeV)	MDM (E_α=40.5 MeV)	MDM [16] (E_α=65 MeV)	AMD [17]	OCM [18]
R_{rms} (fm)	2.88 ± 0.16	2.84 ± 0.12	2.87 ± 0.13	3.1	3.0

Results and Conclusion

The experimental angular distributions of elastic and inelastic scattering of deuterons from ^{11}B nuclei have pronounced diffraction pattern in the whole angular range. There is a notable enhancement at backward angles, this can be due to the contribution of other mechanisms to the scattering cross sections (contribution of compound nucleus, resonance scattering etc.). The calculated differential cross sections are in fairly good agreement with the experimental data.

The estimated radii of $3/2^-$ (8.56 MeV) state is increased with respect to the radius of ground states and are good agreement with literature data that were obtained using different approaches indicating that the radius of this state is indeed increased. Thus, the expected cluster structure of this state is verified.

References

1. Bulter J.W. Table of (p,γ) resonances by proton energy: E = 0.163 – 3.0 MeV. // U.S. Naval Research Laboratory. NRL Report. – 1959. – P. 5282-5299.

2. W. Fitz, R. Jahr, R. Santo. Scattering and pick-up reactions with deuterons on Be, B,C,N and O at 11.8 MeV // Nuclear Physics. Section A. – 1967. – Vol. 101 .– P .449.

3. A.N. Vereshchagin, I.N. Korostova, L.S. Sokolov, V.V.Tokarevskii, I. P.Chernov. Investigation of elastic scattering of deuterons on light nuclei with 13.6 MeV energy // Bull. Russian Academy of Sciences. – Physics. – 1969. – Vol. 32. – P.573.

4. Slobodrian R.J. Scattering of 27.7 MeV deuterons on beryllium and boron // Nuclear Physics. – 1962. – Vol. 32. – P.684–694.

5. Burtebaev N., Baktybaev M.K., Duisebaev B.A., Peterson R. J., and Sakuta S. B. Scattering of

α Particles on 11B Nuclei at Energies 40 and 50 MeV // Physics of Atomic Nuclei. – 2005. – Vol. 68. – P. 1303–1313.

6. Abele H. et al. Measurement of Folding-Potential Analysis of the Elastic α-Scattering on Light Nuclei // Zeitschrift für Physik A Atomic Nuclei. – 1987. – Vol. 326. – P. 373–381.

7. Thompson I.J. Coupled reaction channels calculations in nuclear physics // Comput. Phys. Re. – 1988. – Vol. 7. – P. 167–212.

8. Bertsch G, Borysowicz J, Mc Manus H and Love W G. Interactions for inelastic scattering derived from realistic potentials // Nucl. Phys. A. – 1977. – Vol. 284. – P. 399-419.

9. Anantaraman N, Toki H and Bertsch G An effective interaction for inelastic scattering derived from the Paris potential // Nucl. Phys. A. – 1983. – Vol. 398. – P. 269-278.

10. Satchler G.R. and Love W.G. Folding model potentials from realistic interactions for heavy-ion scattering // Phys. Re. – 1979. – Vol. 55. – P. 183-254.

11. Jeukenne J, Lejeune A and Mahaux C Optical-model potential in finite nuclei from Reid's hard core interaction // Phys. Rev. C. – 1977. – Vol. 16. – P. 80.

12. Kobos A.M., Brown B.A., Hodgson – P.E., Satchler G.R. and Budzanowski A. Folding model analysis of α-particle elastic scattering with a semirealistic density-dependent effective interaction // Nucl. Phys. A. – 1982. – Vol. 384. – P. 65-87.

13. Kobos A.M., Brown B.A., Lindsay R. and Satchler G.R. Folding-model analysis of elastic and inelastic α-particle scattering using a density-dependent force // Nucl. Phys. A. – 1984. – Vol. 425. – P. 205-232

14. Brandan M.E. and Satchler G.R. Folding model analysis of 12,13C+12C and 16O+12C scattering at intermediate energies using a density-dependent interaction // Nucl. Phys. A. – 1988. – Vol. 487.– P. 477-492

15. Danilov A. N. et al. Study of Elastic and Inelastic 11B +α Scattering and Search for Cluster States of Enlarged Radius in 11B // Physics of Atomic Nuclei. – 2015. – Vol. 78. – P. 777–793.

16. Danilov A.N., Belyaeva T.L., Demyanova A.S., Goncharov S.A. and Ogloblin A.A. Determination of nuclear radii for unstable states in 12C with diffraction inelastic scattering // Physical Review C. – 2009. – Vol. 80. – P. 054603

17. Suhara T. and Kanada-En'yo Y. Cluster structures in 11B // Phys. Rev. C. – 2012. – Vol. 85.– P. 054320

18. Yamada T. and Funaki Y. α + α + t cluster structures and 12C(0_2^+)-analog states in 11B // Phys. Rev. C. – 2010. – Vol.82. – P. 064315

International Journal of Mathematics and Physics 7, №2, 89 (2016)

UDC 533.9

[1*]Arkhipov Yu.V., [1]Ashikbayeva A.B., [1]Askaruly A., [1]Dubovtsev D.Yu.,
[1]Syzganbayeva S.A., [2]Tkachenko I.M.

[1]IETP, al-Farabi Kazakh National University, Almaty, Kazakhstan,
[2]Instituto de Matemática Pura y Aplicada, Universidad Politécnica de Valencia,
Camino de Vera s/n, 46022 Valencia, Spain
[*]e-mail: yarkhipov@yahoo.ca

Stopping power of non-ideal plasmas: the moment approach

Abstract. The moment approach to the description of dynamic properties of non-ideal plasmas takes into account convergent sum rules automatically and depends on the model of the Nevanlinna parameter function (NPF). A new model of the two-componet plasma NPF is suggested to satisfy the Perel'-Eliashberg high-frequency asymptote, to reproduce the static conductivity value, and the stopping power slow projectile asymptote. The coefficient of the latter is calculated in the extended random-phase approximation. The solution is reduced to that of a transcendental equation.

Key words: Stopping power, method of moments, non-ideal plasma, nevanlinna parameter

Introduction: hypothesis

The moment approach to the reconstruction of a plasma inverse dielectric function (IDF) $\varepsilon^{-1}(k,\omega)$ which satisfies three non-zero sum rules expresses it in terms of the Nevanlinna parameter function (NPF), $Q(k,\omega)$, as [1, 2]

$$\varepsilon^{-1}(k,\omega)= \\ =1+\frac{\omega_p^2\left(\omega+Q(k,\omega)\right)}{\omega\left(\omega^2-\omega_2^2(k)\right)+Q(k,\omega)\left(\omega^2-\omega_1^2(k)\right)}, \qquad (1)$$

where the characteristic frequencies, $\omega_2(k)$ and $\omega_1(k)$ are determined by three successive convergent non-zero power moments of the loss function, $\mathcal{L}(k,\omega)=-Im\varepsilon^{-1}(k,\omega)/\omega$ or the sum rules:

$$\omega_1(k)=\sqrt{\frac{C_2}{C_0(k)}}, \quad \omega_1(k)=\sqrt{\frac{C_4(k)}{C_2}},$$

$$C_\nu(k)=\frac{1}{\pi}\int_{-\infty}^{\infty}\omega^\nu\mathcal{L}(k,\omega)d\omega, \quad \nu=0,2,4.$$

Notice that odd-order moments vanish due to the parity of the integrand, higher even-order moments diverge [3].

The aim of the present research note is to specify the NPF for two-component plasmas (TCPs) so that we could simultaneously satisfy three limiting conditions:

1. the high-frequency Perel'-Eliashberg form for the plasma dielectric function [3];
2. the static conductivity value;
3. and the correct behavior of the plasma (polarizational) stopping power for slow projectiles together with the possibility to calculate the stopping power straggling [2].

Our hypothesis for the dimensionless NPF is the following:

$$\frac{Q(k,z)}{\omega_p}=\frac{A\omega_p\sqrt{\omega_p z}\,(1+i)}{\omega_2^2(k)-\omega_1^2(k)}+ \\ +i\left(Ba^2k^2+\frac{\omega_p H}{\nu(z)+(1-i)\sqrt{\omega_p z}}\right). \qquad (2)$$

Here: H is the electron-ion correlation contribution to the fourth moment of the loss function:

$$A=3^{-5/4}Z^3r_s^{3/4}\sqrt{2}\,; \qquad (3)$$

$$\nu(z)=\frac{\omega_p^2H\nu}{\omega_p^2H-iz\nu}, \qquad (4)$$

where is the static collision frequency such that the static conductivity

$$\sigma_0 = \sigma(0,0) = \frac{\omega_p^2}{4\pi\nu}.$$

The static collision frequency was calculated by [4]. As always, let us introduce the electronic Wigner-Seitz radius a, the Bohr radius, a_B, the system temperature in energy units, β^{-1}; then $\Gamma = \beta e^2 / a$ and $r_s = a / a_B$ are the coupling and degeneracy parameters, and $B > 0$ is the dimensionless parameter dependent on the plasma thermodynamic conditions selected so that the dimensionless polarizational stopping power of slow projectiles [2]

$$-\left(\frac{dE}{dx}\right)\beta a\Bigg|_{v\to 0} = \frac{2\left(Z_p e\right)^2 \beta a}{\pi v^2}\int_0^\infty \frac{dk}{k}\int_0^{kv}\omega^2 \mathcal{L}(k,\omega)\,d\omega\Bigg|_{v\to 0} \simeq C\frac{v}{v_F} \tag{5}$$

and the dimensionless straggling,

$$\Omega^2(v)\beta^2 a = \frac{2\left(Z_p \beta e\right)^2 a\hbar}{\pi v^2}\int_0^\infty \frac{dk}{k}\int_0^{kv}\omega^3 \mathcal{L}(k,\omega)\coth\frac{\beta\hbar\omega}{2}\,d\omega, \tag{6}$$

has a finite value. Here, v_F is the Fermi velocity and $Z_p e$ is the charge of the projectiles which traverse the target plasma with the velocity v.

The framework

The idea is, for a given set of thermodynamic parameters, to calculate the constant C in (5) in the extended random-phase approximation for a TCP and then solve the transcendental equation

$$\int_0^\infty \frac{a^3\omega_p^2 k^2\left[\omega_2^2(k)-\omega_1^2(k)\right]}{\left(Ba^2k^2+\dfrac{\omega_p H}{\nu}\right)\omega_1^4(k)}dk = \frac{3\pi\sqrt{3}}{2\sqrt[3]{\dfrac{9\pi}{4}}}\frac{C\sqrt{r_s}}{Z_p^2\Gamma}, \tag{7}$$

or

$$\int_0^\infty \frac{q^2\left[x_2^2(q)-x_1^2(q)\right]dq}{\left(Bq^2+\dfrac{\omega_p H}{\nu}\right)x_1^4(q)} = \frac{3\pi\sqrt{3}}{2\sqrt[3]{\dfrac{9\pi}{4}}}\frac{C\sqrt{r_s}}{Z_p^2\Gamma}, \tag{8}$$

stemming from (5) for small values of the projectile velocity since the zero-frequency value of the loss function is

$$\mathcal{L}(k,0) = \frac{\omega_p\left[\omega_2^2(k)-\omega_1^2(k)\right]}{\left(Ba^2k^2+\dfrac{\omega_p H}{\nu}\right)\omega_1^4(k)}. \tag{9}$$

In addition, in (8) we have introduced dimensionless variables:

$$x = \frac{\omega}{\omega_p},\quad x_1 = \frac{\omega_1}{\omega_p},\quad x_2 = \frac{\omega_2}{\omega_p},\quad q = ak.$$

The convergence of the integral on the l.h.s. of (7) and (8), can be guaranteed if we take into account the quantum-mechanical nature of the process and write the characteristic frequency $\omega_1(k)$ as in [5]:

$$\omega_1(q) = \omega_p\frac{\sqrt{q^4\kappa^2+q^2\varkappa^4+\kappa^2\varkappa^4}}{\kappa\varkappa^2}\underset{q\to\infty}{\simeq} q^2, \tag{10}$$

where, in a hydrogen-like plasma with

$$n_e = Zn_i,$$

$$\kappa^2 = 4\pi e^2 \beta a^2 \left(n_e + Zn_i\right),$$

$$\varkappa^4 = \frac{16\pi e^2}{\hbar^2} a^4 \left(n_e m_e + Z^2 n_i m_i\right) \approx$$
$$\approx \frac{16\pi Z e^2 n_e a^4 m_i}{\hbar^2} = 12 r_s \frac{m_i}{m_e}.$$

Then, in the short-wavelength approximation,

$$\frac{q^2}{Bq^2 + \frac{\omega_p H}{\nu}} \left(\frac{x_2^2(q)}{x_1^4(q)} - \frac{1}{x_1^2(q)} \right) \underset{q\to\infty}{\simeq} \frac{\alpha}{q^4}$$

and the integrals with B converge without any additional efforts applied.

The stopping of slow projectiles

As it was already mentioned, we precalculate the dimensionless constant C in the extended RPA and for hydrogen-like plasmas. Then the system dielectric function can be written as

$$\varepsilon\left(k,\omega\right) = 1 + \frac{3\Gamma}{q^2} \left(\frac{\Pi_e(k,\omega)}{\beta n_e} + \frac{Z\Pi_i(k,\omega)}{\beta n_i} \right), \quad (11)$$

where $\Pi_e(k,\omega)$ and $\Pi_i(k,\omega)$ are the subsystems' partial polarization operators. We presume that it suffices to introduce the local field correction $G(k)$ in the electronic component only:

$$\frac{\Pi_e(q,\omega)}{\beta n_e} = \frac{\left(\frac{\Pi_{e0}(q,\omega)}{\beta n_e} \right)}{1 - \frac{3\Gamma}{q^2} G(q) \left(\frac{\Pi_{e0}(q,\omega)}{\beta n_e} \right)}.$$

Expressions for $\Pi_{e0}(k,\omega)$ and $G\left(k\right)$ were provided in [2], while here we can simply put

$$\frac{\Pi_i(q,\omega)}{\beta n_i} = \frac{\Pi_{i0}(q,\omega)}{\beta n_i} = \frac{\Pi_{i0}(q,0)}{\beta n_i} = 1,$$

since for the present problem we need only the static value of the polarization operators and their imaginary parts, which vanish at $\omega = 0$.

Let

$$\frac{\Pi_{e0}\left(k,\omega\right)}{\beta n_e} = X\left(q,x\right) + iY\left(q,x\right),$$

where, then

$$X\left(q,0\right) = \frac{3r_s}{q\Gamma} \left(\frac{9\pi}{4}\right)^{-\frac{1}{3}} \int_0^\infty \frac{y\,dy}{\exp\left(Dy^2 - \eta\right) + 1} \ln \left| \frac{q + 2\left(\sqrt[3]{\frac{9\pi}{4}}\right) y}{q - 2\left(\sqrt[3]{\frac{9\pi}{4}}\right) y} \right|,$$

$$Y\left(q, x \to 0\right) = \frac{2x}{\sqrt{3}} \frac{r_s^{\frac{3}{2}}}{\Gamma q} \frac{e^{\eta - \frac{\Gamma q^2}{8 r_s}}}{e^{\eta - \frac{\Gamma q^2}{8 r_s}} + 1}.$$

We have now that

$$C_{\mathrm{xRPA}} = \frac{4Z_p^2}{3\pi} \left(\Gamma r_s\right) \left(\sqrt[3]{\frac{9\pi}{4}}\right) \int_0^\infty \frac{\left(1 + \exp\left(\frac{\Gamma q^2}{8 r_s} - \eta\right)\right)^{-1} \frac{dq}{q}}{\left(1 + \frac{3\Gamma X}{q^2}\left(1 + Z - G\right) - \left(\frac{3\Gamma X}{q^2}\right)^2 ZG\right)^2}. \quad (12)$$

Finally, we arrive to the following equation for the parameter B:

$$\int_0^\infty \frac{q^2\left[x_2^2(q)-x_1^2(q)\right]dq}{\left(Bq^2+\frac{\omega_p H}{\nu}\right)x_1^4(q)} = \int_0^\infty \frac{2\sqrt{3}r_s^{\frac{3}{2}}\left[1+\exp\left(\frac{\Gamma q^2}{8r_s}-\eta\right)\right]^{-1}\frac{dq}{q}}{\left[1+\frac{3\Gamma X}{q^2}(1+Z-G)-\left(\frac{3\Gamma X}{q^2}\right)^2 ZG\right]^2}, \qquad (13)$$

where

$$X = X(q,0), \quad G = G(q), \quad Z = 1$$

in hydrogen, and, as usually, the electronic dimensionless chemical potential $\eta = \beta\mu$ is defined by the normalization equation:

$$F_{1/2}(\eta) = \frac{2}{3}D^{3/2}$$

with

$$F_\nu = \int_0^\infty \frac{x^\nu dx}{\exp(x-\eta)+1},$$

$$D = \beta E_F = \beta\hbar^2 k_F^2 / 2m = \beta\hbar^2\left(3\pi^2 n\right)^{2/3} / 2m,$$

where $F_\nu(\eta)$, E_F, and k_F are the ν-th order Fermi integral, Fermi energy, and wavenumber, respectively.

Numerical results

We have calculated the coefficient C, the constant B (from (8) or (13) with (10)), computed the corresponding stopping and straggling with the NPF from (2), studied the asymptotic (at low velocities, $v/v_{th} \lesssim 0.1$, $v_{th} = \sqrt{\beta^{-1}m}$) behavior of the stopping power. The results are presented on the following figures. The number density of the electronic subsystem of the target plasma has been chosen to be equal to $n_e = 10^{23}\ cm^{-3}$ so that $r_s = 2.5256$. The high-velocity asymptotic form of the dimensionless stopping power taking into account the target plasma electron-ion interaction [6],

$$-\left(\frac{dE}{dx}\right)\beta a\bigg|_{v\to\infty} = \left(\frac{Z_p e\omega_p}{v^2}\right)^2 \beta a \ln\frac{2mv^2}{\hbar\omega_p\sqrt{1+H}},$$

is represented by continuous lines. Protons were chosen as projectiles.

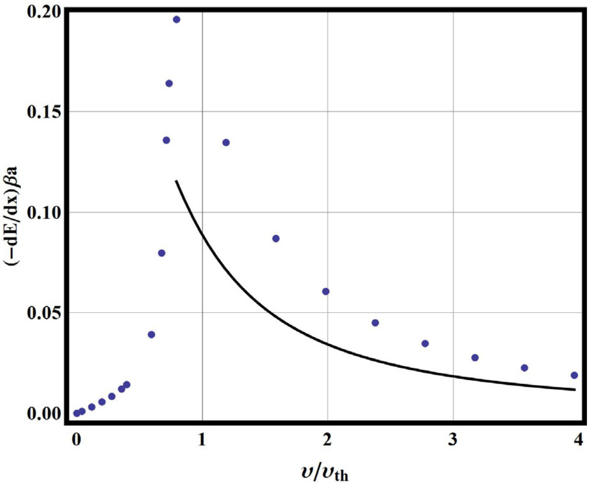

Figure 1a – The TCP stopping power for Γ = 0.1077

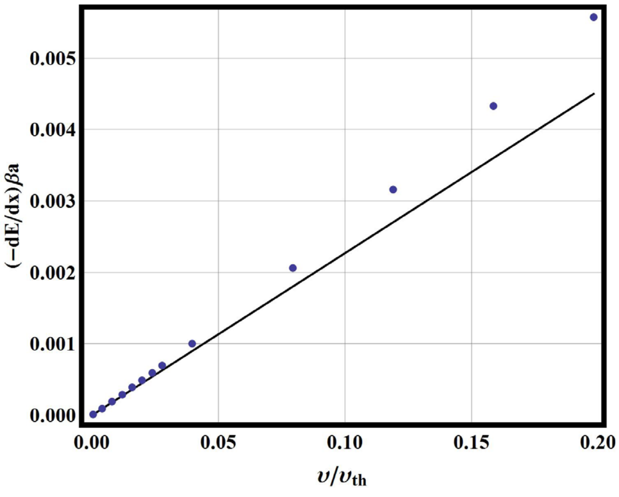

Figure 1b – The TCP stopping power for Γ = 0.1077, slow projectiles

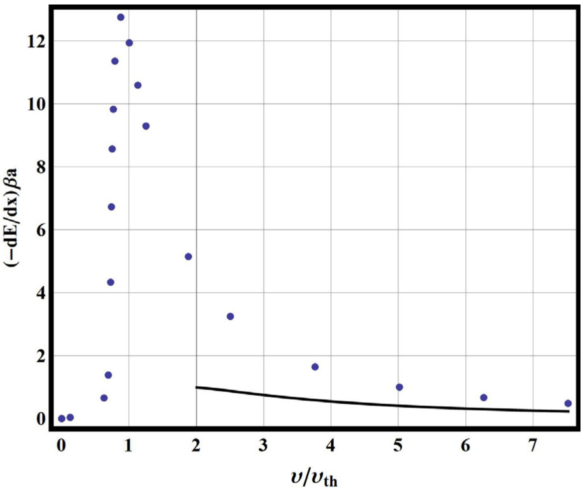

Figure 2a – As in Fig. 1a, but for Γ = 1.077

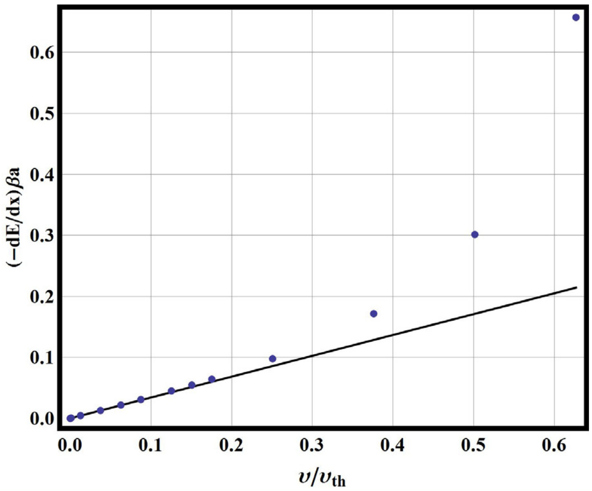

Figure 2b – As in Fig. 1b, but for Γ = 1. 077

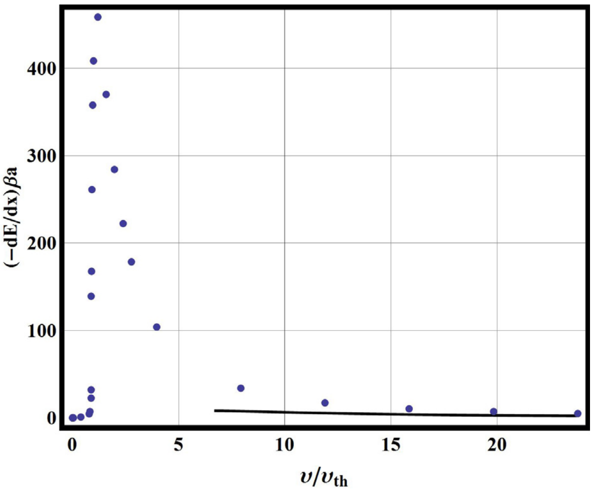

Figure 3a – As in Fig. 1a, but for Γ = 10.77

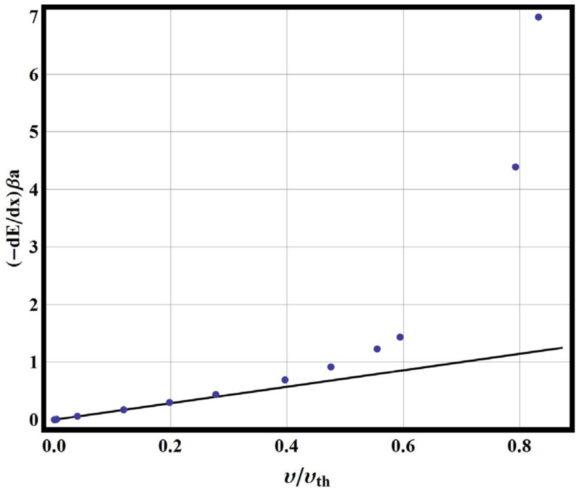

Figure 3b – As in Fig. 1b, but for Γ = 10.77

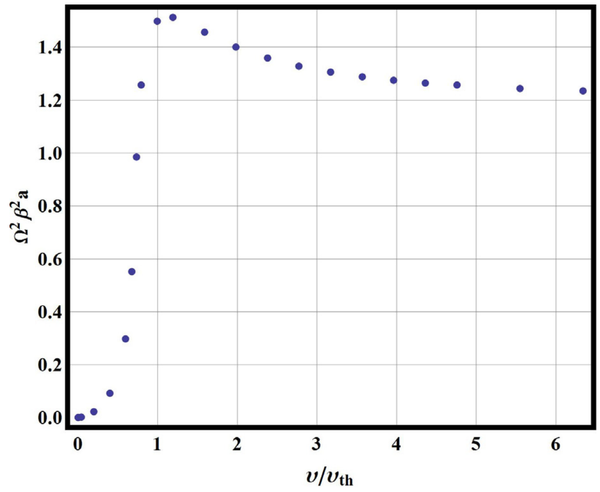

Figure 4a – The TCP straggling for Γ = 0.1077

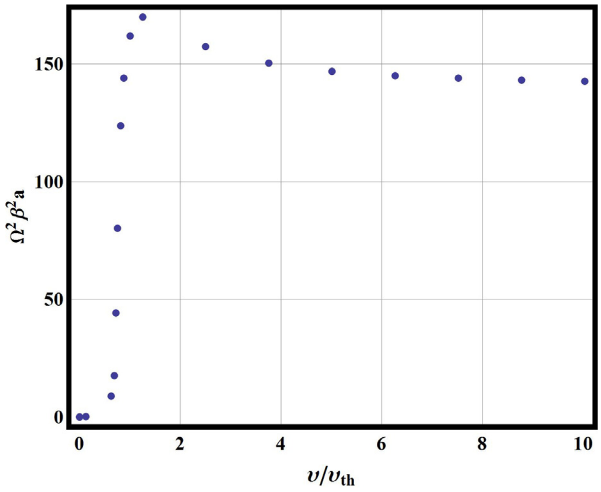

Figure 4b – As in Fig. 4a but for Γ = 0.1077

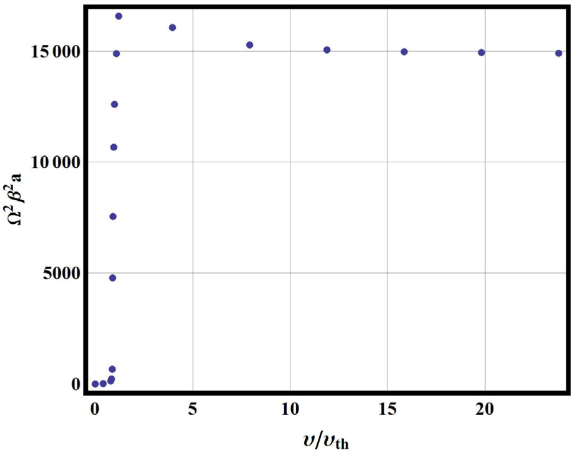

Figure 4c – As in Fig. 4a but for Γ = 10.77

The values of the parameters C and B are provided in the Table below for the reference.

Γ = 0.1077	Γ = 1.077	Γ = 10.77
C = 0.00774	C = 0.42848	C = 5.6685
B = 9.56152	B = 39.511	B = 491.671

Conclusions

We observe a significant enhancement of both stopping power and straggling of non-ideal or medium-coupled TCPs. This effect is to be confirmed experimentally. On the other hand, the form of the NPF is to be specified further in an attempt to describe simultaneously other dynamic characteristics, like the dynamic structure factor and mode dispersion [7].

Acknowledgements

Work supported by the Republic of Kazakhstan Ministry of Education and Science grant No. 3119/6GF4, 3831/GF4 and by the Spanish Ministerio de Economía, Ciencia e Innovación Project ESP2013-41078-R. A. A. expresses gratitude for the financial support provided by the grant "The Best Lecturer".

References

1. M.G. Krein and A.A. Nudel'man.*The Markov moment problem and extremal problems //* Trans. of Math. Monographs. Amer. Math. Soc. Providence. R.I. – 1977. – Vol. 50.
2. I.M. Tkachenko, Yu.V. Arkhipov, A. Askaruly. *The Method of Moments and its Applications in Plasma Physic*. LAMBERT Academic Publishing. – Saarbrücken. – Germany. – 2012.
3. Yu.V. Arkhipov, A.B. Ashikbayeva, A. Askaruly, A.E. Davletov, I.M. Tkachenko. Dielectric function of dense plasmas, their stopping power, and sum rules // Phys. Rev. E. – 2014. – Vol. 90. – P. 053102. ibid, Phys. Rev. E. – 2015. – Vol 91. – P. 019903.
4. V.I. Perel' and G.M. Eliashberg. Absorption of Electromagnetic Waves in Plasma // Zh. Eksp. Teor. Fiz. – 1961. – Vol. 41. – P. 886.
5. M. Baus, J.-P. Hansen, and L. Sjögren. Electrical conductivity of a strongly coupled hydrogen plasma // Phys. Lett. A. – 1981. – Vol. 82. – P. 180.
6. Yu.V. Arkhipov, A.B. Ashikbayeva, A. Askaruly, A.E. Davletov, D.Yu. Dubovtsev, I.M. Tkachenko. Screened Effective Interaction Potential for Two-Component Plasmas // Contr. Plasma Phys. – 2016. – Vol. 56. – P. 403.
7. B. Ballester, I.M. Tkachenko.Fast-Projectile Stopping Power of Quantal Multicomponent Strongly Coupled Plasmas // Phys. Rev. Lett. – 2008. – Vol.101. – P. 075002.
8. Yu.V. Arkhipov, A.B. Ashikbayeva, A. Askaruly, A.E. Davletov, S. Syzganbaeva, V.V, Voronkov, and I.M. Tkachenko. Dense Plasma Dynamic Structure Factor Simulation Data vs. the Method of Moments // Contr. Plasma Phys. – 2015. – Vol. 55. – P. 381.

International Journal of Mathematics and Physics 7, №2, 95 (2016)

UDC 533.9:51-73

[*]Davletov A.E., Yerimbetova L.T., Askaruly A., Mukhametkarimov Ye.

IETP, al-Farabi Kazakh National University, 71 Al-Farabi ave., 050040 Almaty, Kazakhstan
[*]e-mail: askar@physics.kz

OML evaluation of the dust grain charge under quasineutrality conditions

Abstract. Interaction potentials of electrons and ions with dust particles are developed to consistently treat plasma electrodynamics. It is assumed for the sake for simplicity that the material, the dust particles are made of, is a perfect conductor, and, then, the linear density-response formalism in the random phase approximation is used to take into account finite dimensions of grains. Additionally, the number density of protons is kept fixed such that the negative electric charge is allocated between the free electrons and the dust particles to assure the whole quasineutrality of the system. On the ground of the developed interaction potentials the electric charge of the dust particles is then calculated within the orbital motion limited (OML) approximation, which stems from the ballistic trajectories of the plasma particles at the charging process. It is rather clear that to advocate such a technique the mean free paths of the plasma particles must be much greater than the dimension of the dust grain. It is well known that under OML assumptions the conservation laws of energy and angular momentum are sufficient to determine the absorption cross sections of electrons and ions by the dust particle. The resultant absorption cross sections are then integrated over the velocity distribution distribution function to evaluate the fluxes of plasma particles on the grain surface, and the electric charge of the dust particle is stabilized when those fluxes are finally equalized.
Key words: dust grain charge, interaction potential, density-response formalism, orbital motion limit approximation, velocity distribution function.

Introduction

Over the past few decades, much attention of researchers in the field of plasma physics has been paid to the so-called dusty plasmas, which appear in a variety of situations, both in nature and in laboratory. In particular, dusty plasmas can be encountered in many kinds of astrophysical objects [1-3], space and earth experiments [4-6], nanotechnology [7.8], cancer therapy in medicine [9,10] and in many other industries. Moreover, dust plasmas are working substances in the installations designed for controlled thermonuclear fusion [11,12] and for plasma etching in the modern electronics industry [13,14] since solid particles of micron size easily penetrate into the plasma medium as a result of the destruction of electrodes and walls of plasma chambers. This results not only in immediate change of physical properties of the surface material, but also in considerable perturbation, mostly in an unpredictable way, of local plasma characteristics.

In this regard, the study of dusty plasma properties is of great scientific interest from both fundamental and applied physics points of view. An important role for the explanation of various phenomena in dusty plasmas is played by the plasma sheath theory, since, on the one hand, it is virtually impossible to completely avoid direct contact of the plasma medium with electrodes and chamber walls, and it is this contact which is responsible for dusty plasma generation. On the other hand, dust particles are themselves solid bodies, which are surrounded by the plasma sheath that ultimately governs their electric charge.

Plasma parameters

It is widely understood that typical dusty plasma consists of at least four particle species. For simplicity, assume in the following that the buffer plasma contains free electrons with the electric charge $-e$ and the number density n_e, and free protons with the electric charge e and the number density n_p. In addition, the buffer plasma is assumed to be filled with the dust particles of the same radius R to constitute another species with the number density n_d. It is exactly this system which is conventionally called a dusty plasma. The medium is normally non-isothermal such that the electron temperature T_e substantially exceeds the proton temperature T_p, whereas the dust particles temperature is supposed to be equal to the proton temperature. In real dusty plasmas uncharged particles are inevitably present, but in the sequel pure electrostatic interactions are in focus which somehow justifies further disregard of the neutral component.

It is rather convenient to introduce few dimensionless parameters describing the physical state of the dusty plasma. For reasons that are to become clearer later, the number density of protons is kept fixed and the coupling parameter of the buffer plasma is defined as:

$$\Gamma = \frac{e^2}{a_p k_B T_p}, \tag{1}$$

where k_B denotes the Boltzmann constant, and $a_p = (3/4\pi n_p)^{1/3}$ stands for the average distance between the protons.

In addition, we introduce the ratio of the number densities of dust particles and protons as follows

$$\beta = \frac{n_d}{n_p}. \tag{2}$$

The main objective of the following is to account for the dimensions of the dust particles by incorporating the size parameter

$$D = \frac{a_d}{R}, \tag{3}$$

where $a_d = (3/4\pi n_d)^{1/3}$ refers to the average distance between the dust particles.

Electric charge of the dust particles essentially depend on mobilities of surrounding plasma particles, whose ration is described by the non-isothermality parameter of the form:

$$\tau = \frac{T_e}{T_p}. \tag{4}$$

Note that the particle mobility strongly depends on its mass, but in the following subsequently the ratio of the proton mass m_p to the electron mass m_e is assumed to be known and equal to ~ 1637

Finally, he whole system remains quasi-neutral, i.e. the following condition holds

$$n_p = n_e + Z_d n_d, \tag{5}$$

where Z_d is a, still unknown, electric charge of the dust particles, which is, in the present consideration, a function of dimensionless parameters (1)-(4). Note that since the number density of of protons is fixed, condition (5) determines the balance between the charge of dust particles and the number density of electrons in the buffer plasma.

Interaction model

When considering the interaction of dust grains immersed in a plasma it is widely believed that their electric charge is governed by the normal component of the electric field near the particle surface what is incorrect in terms of plasma electrodynamics [15]. It was also shown [16] that engaging of plasma electrodynamics results in the following interaction potential $\Phi_{ab}(r)$ between the particles of dusty plasmas:

$$\begin{aligned}\Phi_{ab}(r) = \varphi_{ab}(r) - \\ -\frac{Q_{ab}}{r}\left[1 - \exp(-k_D r) - \frac{k_D R_{ab}}{2}\mathrm{B}_{ab}(r)\right],\end{aligned} \tag{6}$$

with

$$\begin{aligned}\mathrm{B}_{ab}(r) = \exp(k_D(R_{ab}+r))\,\mathrm{Ei}(k_D(R_{ab}+r)) - \\ -\exp(k_D(R_{ab}-r))\,\mathrm{Ei}(k_D R_{ab}) + \\ +\exp(-k_D(R_{ab}+r)) \\ \left[\mathrm{Ei}(k_D R_{ab}) - \mathrm{Ei}(-k_D(R_{ab}+r))\right]\end{aligned} \tag{7}$$

and the exponential integral function

$$\mathrm{Ei}(x) = \int_x^\infty \frac{\exp(-t)}{t}\,dt. \tag{8}$$

Here the micropotential is defined as $\varphi_{ab}(r) = Q_{ab}/(R_{ab}+r)$, r is counted from the dust surface, $Q_{ed} = -Q_{pd} = Z_d e^2$, $R_{ed} = R_{pd} = R$ and $Q_{dd} = Z_d^2 e^2$, $R_{dd} = 2R$. Note that the screening in (6) is only due to electrons and ions of the buffer plasma such that the Debye wave number reads as:

$$k_D = \sqrt{\frac{4\pi n_e e^2}{k_B T_e} + \frac{4\pi n_p e^2}{k_B T_p}}. \tag{9}$$

It is known from the literature that the shielding effects start to appear from the surface of the dust particles and the Debye theory together with the assumption that the electric charge of the dust particle is determined by the normal component of the electric field strength at the surface leads to the following interaction potential:

$$\Phi_{ab}(r) = \frac{Q_{ab}}{(r+R_{ab})(1+2k_D R)} \exp(-k_D r) \,. \quad (10)$$

Figure 1 shows comparative curves of the micropotential, potentials (6) and (10) as functions of the dimensionless distance. It is clearly observed that screened potential (6) and the micropotential lie higher than Yukawa-type potential (10). The resulting difference between the micropotential and the screened potential (6) at small interparticle separations is associated with the consistent use of plasma electrodynamics [16].

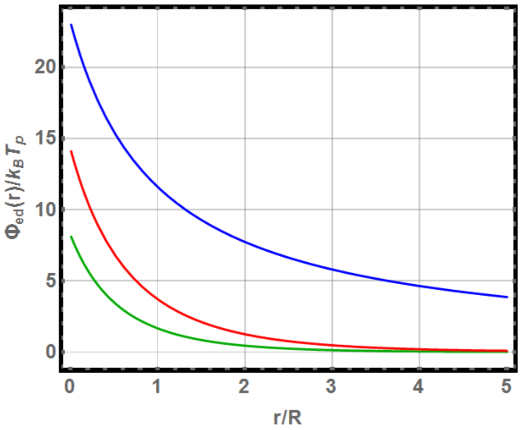

Figure 1 – Interaction potential $\Phi_{ed}(r)$ between the electron and the dust particle in a plasma at $\tau = 5$, $\Gamma = 0.05$, $\beta = 10^{-4}$, $D = 10$ and $Z_d = 1000$. Blue line: micropotential; green line: Yukawa potential (10); red line: screened potential (6)

OML for dust grain charge evaluation

To determine the charge of the dust particle of great significance is the orbital motion limited approximation, which is widely used in the theory of plasma probes and allows one to calculate the absorption cross sections of electrons and protons by a dust particle, based on single knowledge of the conservation laws of energy and angular momentum. It is assumed within that electrons and protons freely move on ballistic trajectories in the collective field, created by the dust particle and the plasma sheath, so that the following condition holds:

$$r_D \ll \ell_{e(p)}, \quad (11)$$

where $r_D = k_D^{-1}$ denotes the Debye screening length, and $\ell_{e(p)}$ designates the mean free paths of electrons and protons, respectively.

Consider the process of the dust particle charging in the orbital motion limited approximation [17]. The absorption cross section of protons is found from the conservation laws of energy and angular momentum as:

$$\sigma_p = \pi R^2 \left(1 - \frac{2\Phi_{pd}(0)}{m_p v_p^2} \right), \quad (12)$$

where v_p is the incident proton velocity, and $\Phi_{pd}(0)$ stands for the interaction potential energy of the dust particle with the proton on its surface.

Figure 2 reveals the dependence of the absorption cross section of protons as a function of their kinetic energy. As the proton kinetic energy grows, the corresponding absorption cross section decreases and it increases when the size parameter goes up, which is due to mutual attraction of those particles. Figure 3 shows the absorption cross section of protons as a function of the dust grain charge. Those dependences are practically linear and the cross section rapidly increases with the growth of the dust particle charge which is prescribed to strengthening of attraction of incident protons.

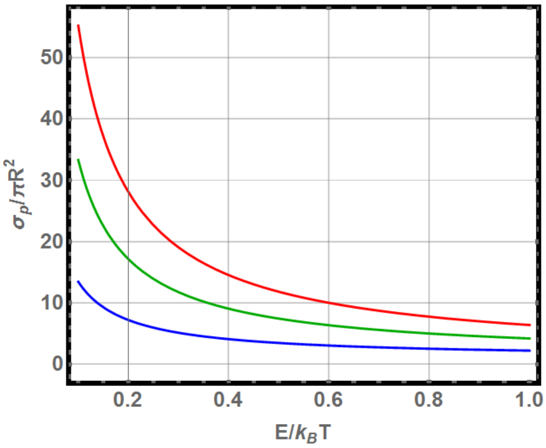

Figure 2 – Absorption cross section of protons (12) by the dust particle as a function of the proton kinetic energy at $\tau = 1$, $\Gamma = 0.1$, $\beta = 10^{-3}$ and $Z_d = 500$. Blue line: $D = 5$; green line: $D = 10$; red line: $D = 15$

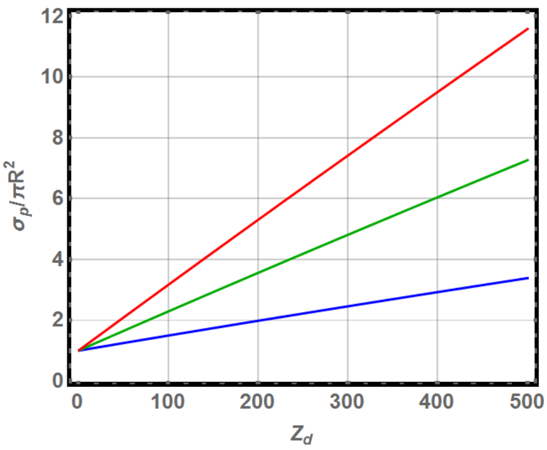

Figure 3 – Absorption cross section of protons (12) by the dust particle as a function of the dust grain charge at τ = 1, Γ = 0.1, β = 10^{-3}, and $E/k_B T = 5$.
Blue line: $D = 5$; green line: $D = 10$; red line: $D = 15$

Similarly, the absorption cross section of electrons is obtained as

$$\sigma_e = \begin{cases} 0, & m_e v_e^2 < 2\Phi_{ed}(0), \\ \pi R^2 \left(1 - \dfrac{2\Phi_{ed}(0)}{m_e v_e^2}\right), & m_e v_e^2 \geq 2\Phi_{ed}(0), \end{cases} \quad (13)$$

where v_e is the incident electron velocity, and $\Phi_{ed}(0)$ stands for the interaction potential energy of the dust particle with the electron on its surface. Note that since the dust particle is negatively charged, an electron must possess a certain threshold kinetic energy to be absorbed by the dust particle.

Figure 4 displays the dependence of the absorption cross section of electrons as a function of their kinetic energy. Since electrons are repelled by the negatively charged dust particle, there exists a threshold kinetic energy at which the absorption turns possible and the corresponding cross section becomes non-zero. As the kinetic energy of electrons grows the absorption cross section increases, and, at the same time, it decreases when the size parameter goes up. Figure 5 demonstrates the dependence of the absorption section of electrons as a function of the dust grain charge. Those dependences are practically linear and the cross section is greatly reduced with the growth of the dust particle charge due its repulsion of bombarding electrons.

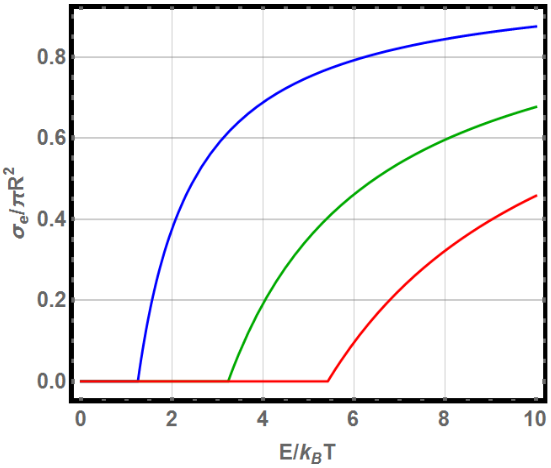

Figure 4 – Absorption cross section of electrons (13) by the dust particle as a function of the electron kinetic energy at τ = 1, Γ = 0.1, β = 10^{-3} and $Z_d = 50$.
Blue line: $D = 5$; green line: $D = 10$; red line: $D = 15$

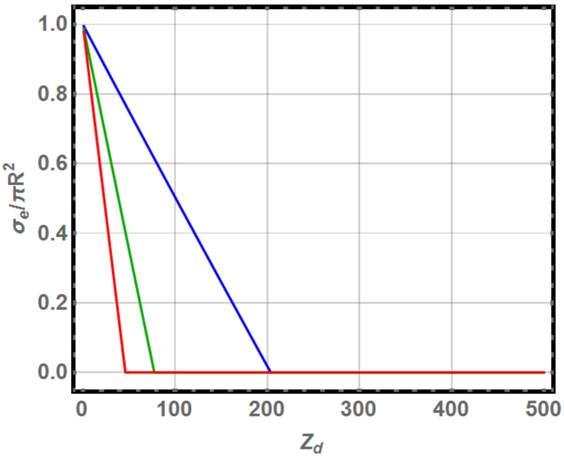

Figure 5 – Absorption cross section of electrons (13) by the dust particle as a function of the dust grain charge at τ = 1, Γ = 0.1, β = 10^{-3}, and $E/k_B T = 5$.
Blue line: $D = 5$; green line: $D = 10$; red line: $D = 15$

It is widely known that the flux I_a of particle species a on the surface of the dust grain is derived from the corresponding absorption cross section by integrating over the velocity distribution as:

$$I_a = n_a \int v \sigma_a f_a(v) d^3\mathbf{v} \quad (14)$$

where $f_a(v) = (2\pi v_{T,a}^2)^{-3/2} \exp(-v^2 / 2v_{T,a}^2)$ simply denotes the Maxwell distribution function with the thermal velocity $v_{T,a} = \sqrt{k_B T_a / m_a}$.

In expression (14) the corresponding absorption cross sections for electrons (13) and protons (12) are substituted, and the following expressions for the fluxes of electrons and protons on the dust grain surface are obtained:

$$I_e = 2\sqrt{2\pi} n_e R^2 v_{T,e} \exp\left(-\frac{\Phi_{ed}(0)}{k_B T_e}\right), \quad (15)$$

$$I_p = 2\sqrt{2\pi} n_p R^2 v_{T,p} \left(1-\frac{\Phi_{pd}(0)}{k_B T_p}\right). \quad (16)$$

The stationary electric charge of the dust particle can be considered established if it absorbs the same number of protons and electrons in a unit of time, i.e. the equality $I_e = I_p$ is to be satisfied and with the help of expressions (15) and (16) the following generalized equation is found

$$\frac{n_p}{n_e}\sqrt{\frac{m_e T_p}{m_p T_e}}\left(1-\frac{\Phi_{pd}(0)}{k_B T_p}\right) = \exp\left(-\frac{\Phi_{ed}(0)}{k_B T_e}\right), \quad (17)$$

and it retains its validity for any kind of interaction potential between the dusty plasma particles.

In case of the Coulomb interaction between the dusty plasma particles, expression (17) is reduced to the following classical form:

$$\frac{n_p}{n_e}\sqrt{\frac{m_e T_p}{m_p T_e}}\left(1+\frac{Z_d e^2}{k_B T_p R}\right) = \exp\left(-\frac{Z_d e^2}{k_B T_e R}\right). \quad (18)$$

In case of the Yukawa potential (10), equation (17) reads as:

$$\begin{gathered}\frac{n_p}{n_e}\sqrt{\frac{m_e T_p}{m_p T_e}}\left(1+\frac{Z_d e^2}{k_B T_p (1+k_D R) R}\right) = \\ = \exp\left(-\frac{Z_d e^2}{k_B T_e (1+k_D R) R}\right)\end{gathered}. \quad (19)$$

It should be emphasized that equations (18) and (19) implicitly imply that the charge of dust particle is determined by the normal component of the electric field strength at its surface, which is incorrect from the viewpoint of plasma electrodynamics.

In case of effective interaction potential (6) that takes into account the influence of the plasma sheath on the interaction with the dust particle of finite size, the following equation holds:

$$\begin{gathered}\frac{n_p}{n_e}\sqrt{\frac{m_e T_p}{m_p T_e}}\left(1+\frac{Z_d e^2}{k_B T_p R}\left[1-k_D R(1+k_D R \exp(k_D R)\,\mathrm{Ei}(-k_D R))\right]\right) = \\ = \exp\left(-\frac{Z_d e^2}{k_B T_e R}\left[1-k_D R(1+k_D R \exp(k_D R)\,\mathrm{Ei}(-k_D R))\right]\right).\end{gathered} \quad (20)$$

Equation (20) correctly treats the boundary condition, which is imposed by the plasma electrodynamics and states that the charge of the dust particle is determined by the normal component of the electric displacement vector at its surface.

Figure 6 indicates the dependence of the dust particle charge, calculated according to formulas (18), (19) and (20), on the non-isothermality parameter. For all three cases, the charge of the dust particles increases with the growth of the non-isothermality parameter, since the mobility of electrons in the plasma considerably increases. It is also seen that the use of the Coulomb potential greatly underestimates the charge of the dust particle, because the screening phenomena significantly weaken the repulsion of electrons that must inevitably lead to an increase in the corresponding flux, and, hence, to a growth of the dust particle charge. On the other hand the use of the correct boundary condition within the plasma electrodynamics, as it is done at the derivation of interaction potential (6), results in a reduction of the dust grain charge compared with the case of straightforward application of the Yukawa potential (10). Figure 7 shows the dependence of the dust particle charge on the size parameter. Again in all three cases, the charge of the dust particle increases with its size since a floating plasma potential remains virtually unchanged. Note that the Coulomb interaction leads to lower values of the dust particle charge because the repulsion of electrons is dramatically weakened.

Analysis of the numerical results reveal that the discrepancy, due to the use of different potentials, manifests itself for the values of the size parameter $D \leq 20$. It is vastly understood in terms of the difference between the proposed screened potential and the micropotential at short interparticle separations, and strengthening of the screening reduces the developed potential at small distances thereby increasing the electron and decreasing the proton absorption cross sections.

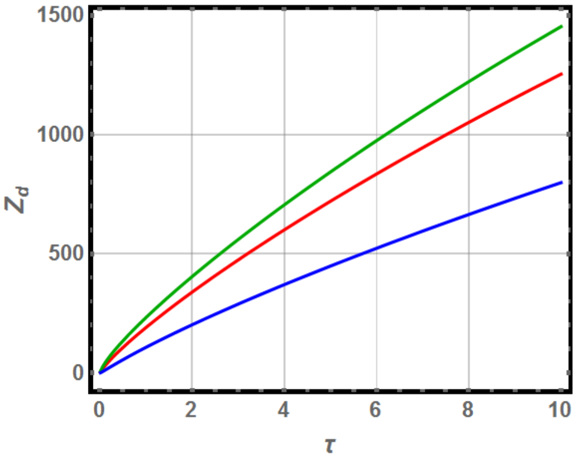

Figure 6 – Dust grain charge Z_d as a function of the non-isothermality parameter τ at D = 10, $\Gamma = 0.05$ and $\beta = 10^{-4}$. Red line: the formula (20); green line: formula (19); blue line: formula (18)

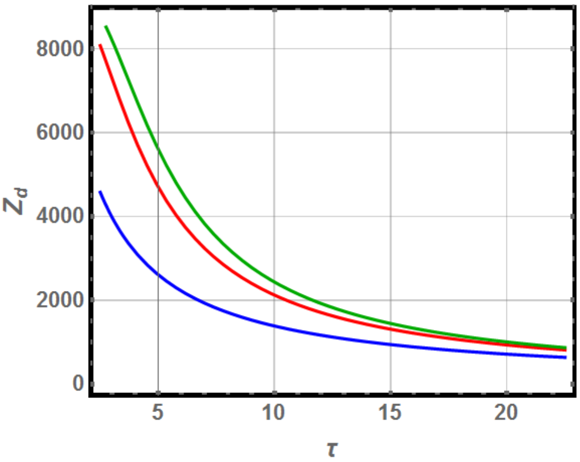

Figure 7 – Dust grain charge Z_d as a function of the size parameter D at $\tau = 20$, $\Gamma = 0.05$ and $\beta = 10^{-4}$. Red line: formula (20); green line: formula (19); blue line: formula (18)

Conclusions

On the basis of the investigations conducted it is possible to make the following conclusions:

1) With increasing the proton kinetic energy, the corresponding absorption cross section decreases, and it increases with the growth of the size parameter, which is explained by mutual attraction of protons and dust particles. It is also found that the absorption cross section of protons increases almost linearly with the increase of the dust particles charge.

2) Since electrons are repelled by the negatively charged dust particles, there exists a threshold kinetic energy at which the absorption becomes possible and the corresponding cross section turns non-zero. While the kinetic energy of electrons increases the absorption cross section drops, whereas it decreases with the growth of the size parameter. All these inferences are easily understood because dust particles repel electrons.

3) A general equation is derived to determine the charge of the dust particles within the OML approximation, which is valid for any kinf of the potential distribution around a dust grain.

4) The charge of the dust particles increases with the non-isothermality parameter, since the mobility of electrons in the plasma increases considerably. Using the Coulomb potential greatly underestimates the charge of the dust particles, because the screening is responsible for significant reduction in the repulsion of electrons that must inevitably lead to an increase of the corresponding flux, and, hence, to a decline of the dust particle charge. On the other hand the use of the strict boundary condition stemming from the plasma electrodynamics leads to a reduction of the dust graim charge compared with the case of direct use of the Yukawa potential. The charge of the dust particles increases with its size because a floating plasma potential remains virtually unchanged and numerical investigations demonstrate that the discrepancy between different potential model is observed for the size parameter $D \leq 20$. The latter is mostly due to the fact that the difference between the proposed screened potential and the micropotential manifests itself at short distances, and strengthening of the screening phenomena reduces the value of the screened potential at the origin, and, hence, increases the electron and decreases the proton absorption cross sections.

Acknowledgements

The authors acknowledge the support from the state grant number 3120/GF4, funded by the Ministry of Education and Science of the Republic of Kazakhstan. A. A. expresses gratitude for the financial support provided by the grant "The Best Lecturer".

References

1 Forsberg M., Brodin G., Marklund M., Shukla P. K. and Moortgat J. Nonlinear interactions between gravitational radiation and modified Alfvén modes in astrophysical dusty plasmas // Phys. Rev. D – 2006. – Vol. 74. – P. 064014 (5 p.).

2 Malmrose M.P., Marscher A.P., Jorstad S.G., Nikutta R. and Elitzur M. Emission from hot dust in the infrared spectra of gamma-ray bright blazars // Astrophys. J. – 2011. – Vol. 732. – P. 116-123.

3 Seok J. Y., Koo B. C. and Hirashita H. Dust cooling in supernova remnants in the large magellanic cloud // Astrophys. J. – 2015. – Vol. 807. – P. 100-106.

4 Izvekova Y.N. and Popel S.I. Charged Dust Motion in Dust Devils on Earth and Mars // Contrib. Plasma Phys. – 2016. – Vol. 56. – P. 263-269.

5 Heidemann H. J., CoueËdel L., Zhdanov S. K., SuËtterlin K. R., Schwabe M., Thomas H. M., Ivlev A. V., Hagl T., Morfill G. E., Fortov V. E., Molotkov V. I., Petrov O. F., Lipaev A. I., Tokarev V., Reiter T. and Vinogradov P. Comprehensive experimental study of heartbeat oscillations observed under microgravity conditions in the PK-3 Plus laboratory on board the International Space Station // Phys. Plasmas – 2011. – Vol. 18. – P. 053701 (10 p.).

6 Fedoseev A.V., Sukhinin G. I., Abdirakhmanov A.R., Dosbolayev M.K. and Ramazanov T.S. Voids in Dusty Plasma of a Stratified DC Glow Discharge in Noble Gases // Contrib. Plasma Phys. – 2016. – Vol. 56. – P. 234-239.

7 Szetsen L., Hsiu-Feng C., and Chien-Ju C. Spectroscopic study of carbonaceous dust particles grown in benzene plasma // J. Appl. Phys. – 2007. – Vol. 101. – P. 113303 (8 p.).

8 Kundrapu M. and Keidar M. Numerical simulation of carbon arc discharge for nanoparticle synthesis // Phys. Plasmas – 2012. – Vol. 19. – P. 073510 (9 p.).

9 Keidar M., Shashurin A., Volotskova O., Stepp M. A., Srinivasan P., Sandler A. and Trink B. Cold atmospheric plasma in cancer therapy // Phys. Plasmas – 2013. – Vol. 20. – P. 057101 (8 p.).

10 Walk R. M., Snyder J. A., Scrivasan P., Kirch J., Diaz S. O., Blanco F. C., Shashurin A., Keidar M. and Sandler A. D. Cold atmospheric plasma for the ablative treatment of neuroblastoma // J. Pediatr. Surg. – 2013. – Vol. 48. – P. 67-73.

11 Winter J. Dust: A new challenge in nuclear fusion research? // Phys. Plasmas – 2000. – Vol. 7. – P. 3862-3866.

12 Castaldo C., Ratynskaia S., Pericolli V., de Angelis U., Rypdal K., Pieroni L., Giovannozzi E., Mad-daluno G., Marmolino C., Rufoloni A., Tuccillo A., Kretschmer M. and Morfill G. E. Diagnostics of fast dust particles in tokamak edge plasmas // Nucl. Fusion – 2007. – Vol. 47. – P. L5-L9.

13 Kokura H., Yoneda S., Nakamura K., Mitsuhira N., Nakamura M. and Sugai H. Diagnostic of Surface Wave Plasma for Oxide Etching in Comparison with Inductive RF Plasma // Jap. J. Appl. Phys. – 1999. – Vol. 38. – P. 5256-5261.

14 Kersten H., Deutsch H., Stoffels E., Stoffels W. W., Kroesen G. M. W., and Hippler R. Micro-Disperse Particles in Plasmas: From Disturbing Side Effects to New Applications // Contrib. Plasma Phys. – 2001. – Vol. 41. – P. 598-609.

15 Davletov A.E., Yerimbetova L.T., Kissan A., Momynov S.B., Mukhametkarimov Ye.S. Influence of polarization phenomena on the dust grain charge in plasmas // Журнал проблем эволюции открытых систем. – 2016. – Вып.18, Т. 1. – С. 24

16 Davletov A.E., Arkhipov Yu.V., Tkachenko I.M. Electric Charge of Dust Particles in a Plasma // Contrib. Plasma Phys. – 2016. – Vol.56, No.3-4. – P.308-320.

17 Shukla P.K., Eliasson B. Fundamentals of dust-plasma interactions // Rev. Mod. Phys. – 2009. – Vol. 81. – P. 25-44.

International Journal of Mathematics and Physics 7, №2, 102 (2016)

UDC 620.197, 533.5:001.89;530.1, 681.3.06

[1,2]Zhukeshov A.M., [1,2*]Gabdullina A.T.,
[3,4]Daineko Y.A., [1,2]Amrenova A.U., [1,2]Fermakhan K.,
[1]Mukhamedryskyzy M., [1]Rysbekova Zh., [3]Sugraliyev S.A.

[1] Scientific – Research Institute of Experimental and Theoretical Physics, Almaty, Kazakhstan
[2] Nanotechnology Laboratory, al-Farabi Kazakh National University, Almaty, Kazakhstan
[3]International IT University, Almaty, Kazakhstan
[4]Institute of Applied Sciences and Information Technologies, Almaty, Kazakhstan
*e-mail: a_gabdullina@mail.ru

Application of vacuum arc deposition surface structural materials

Abstract. This paper presents experimental results of plasma flow impact on the surface of various materials. Using pulsed plasma generated by vacuum arc accelerator, managed to get a copper protective coating on the surface of materials, such as tool steel, carbon steel and aluminum. Treatment of test materials was carried out at various modes of plasma exposure. To demonstrate the deposition process, the paper presents the virtual model of the physical laboratory simulating the creation of the coating. This model allows analyzing this process, to control every stage of the plasma treatment and forms the basis for automation of the proposed deposition technique.

Key words: vacuum-arc accelerator, plasma spraying, protective coating, Virtual Physics Laboratory, Unity 3D.

Introduction

At present, the application of a protective layer on metal surface is one of the effective technological methods to improve the reliability of metal parts industrial equipment. The variety of available materials-coatings gives the possibility to change the properties of the surface layer of every detail depending on the purpose and destination. The use of structural materials is limited by their requirements and high cost. The protective coating on the surface with thickness of a few micrometers may solve the problem. Protective coatings are most commonly used in anticorrosion practice to isolate the metal from corrosive environment, but the coating must be continuous and have good adhesion with the base metal, be impervious to corrosive environment, evenly distributed over the surface, have a high wear resistance, heat resistance and hardness [1-3].

Among the material processing technologies in order to improve the physical and mechanical characteristics of the material is increasingly used plasma treatment of metals, in particular vacuum-arc deposition, which carried out the heating of details and materials to low temperatures (below the melting point of them). The essence of the method is that at certain geometry of electrodes and specific features of applied method is possible to be heated narrow zone of the processed material, which can lead to a local change of the coating structure and properties.

Experiment details

In this paper, experiments on the plasma spraying were conducted on experimental installation VDU-1 [4]. Pulsed discharge in VDU-1 (Fig. 1) occurs between the anode and cathode, arranged coaxially at a distance of 5 cm from each other. The voltage of the ignition is 360÷380 V, anode voltage varies between 120÷130V. Discharge with a frequency of 5 Hz is performed upon reaching a pressure of $44 \div 1{,}6 \times 10^{-4}$millibar for 30÷45 min.

a) b)

a) Front view; b) Side view

Figure 1 – Vacuum-arc accelerator (VDU-1)

High vacuum not only prevents oxidation of the particles of the applied substances, but also reduces the amount of contaminants in them due to their degassing during the flight from the source to the substrate. The use of compound cathodes allows preparing films of multi-component compositions, e.g., solid solutions of metals with the required ratio of components. On the other hand, ions of various metals can enter into active chemical interaction with working gases, specially introduced into the working chamber and this makes it possible to obtain an oxide, nitride, carbide, and other coatings. This paper presents the results of research on the production of coatings on surfaces of different materials, as samples used aluminum and carbon steel. The samples of the test material were loaded into the working chamber at a residual air pressure $1{,}33\times10^{-3}$Pa (1×10^{-5}Torr). After the gas inflow, electric arc evaporator is powered and sets the arc mode. The ignition of the arc discharge is ensured by transmission of the ignition pulse. The film on the cathode under the current action is evaporated and ionized in the area of ignition Operation of the evaporator based on the erosive destruction of the surface layer of the cathode that provides stable combustion of a vacuum-arc discharge between the cathode and the anode. The treatment time is 40 min, the cathode is copper.

Experimental data analysis

For the analysis of experimental data were applied methods of X-ray analysis (Pegasus 2000), electron microscopy (using scanning electron microscope Quanta 3D 200i and polarizing microscope Axio ScopeA1) and metallography (Vickers, Metaval, HVS-1000).

Figures 2 (a and b) shows the data of X-ray analysis of the surface of aluminum samples after processing on the VDU-1 at various parameters. The results of the experiment showed the presence of copper in elemental composition of the surface layer of the samples. In further experiments, were determined operationmodes of VDU-1, at which it was possible to increase copper content from 19.98 to 54.26 % (Fig. 2 b).

X-ray spectral analysis shows that the coating on the carbon steel surface protective layer is also had a positive effect, since the percentage of copper has reached 52,72%, while the iron content fell from 98,47% to 45,50%,which may be associated with structural changes. Along with this, the carbon content decreased from 1,53% to 1,05%, and the oxygen set at 0,73%.

In addition to x-ray analysis, the structure of the carbon steel samples were investigated using a polarizing microscope Axio Scope A1, in which it was found that the surface of the tool steel sample coated with copper protective coating, at least, there are three phase transition. The study of surface topography by electron microscopy showed that plasma treatment leads to surface smoothing, which is typical for aluminum, and carbon steel (Fig. 3-4).

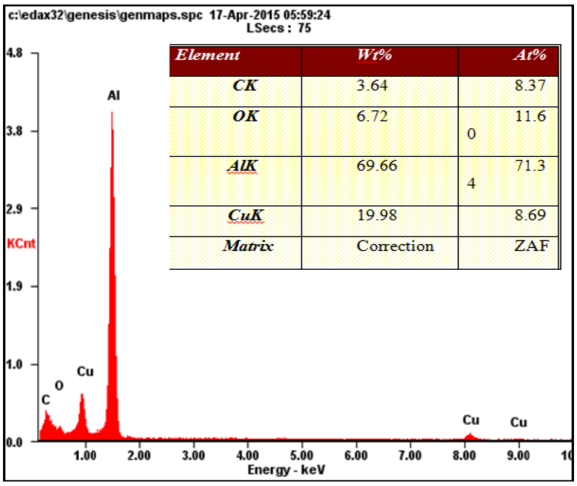

Element	Wt%	At%
CK	3.64	8.37
OK	6.72	11.60
AlK	69.66	71.34
CuK	19.98	8.69
Matrix	Correction	ZAF

a)

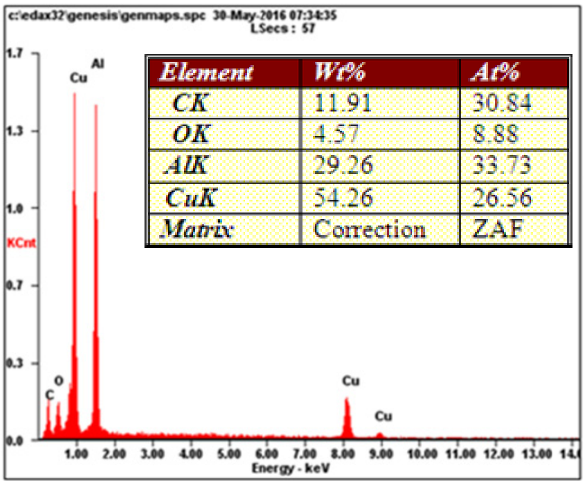

Element	Wt%	At%
CK	11.91	30.84
OK	4.57	8.88
AlK	29.26	33.73
CuK	54.26	26.56
Matrix	Correction	ZAF

b)

Metallographic investigations of carbon steel samples surface after processing on VDU-1 showed an increase of microhardness at average up 125.57 $H_v$to 148.80H_v.

Virtual physics laboratory

For each material it is difficult to find the optimal mode of the plasma processing, therefore, in this paper, was proposed a model for virtual physical laboratory, imitating the process of deposition, which was created in Unity 3D format [5]. This model allows analyzing and controlling every stage of plasma treatment and forms the basis for automation of the proposed deposition technique. The virtual physics laboratory «Studying the plasma spraying» was developed by International Information Technology University, the Computer Engineering and telecommunication department and Al-Farabi Kazakh National University, Physical and Technical Department.

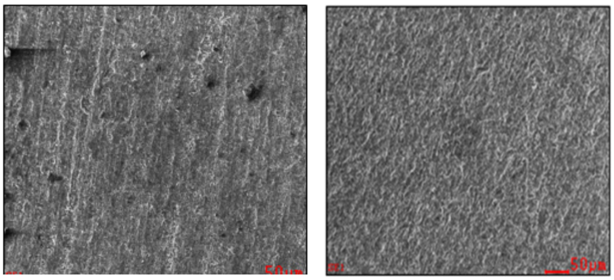

a) b)

Figure 3 – Surface topography of the aluminum samples before (a) and after (b) treatment on VDU-1

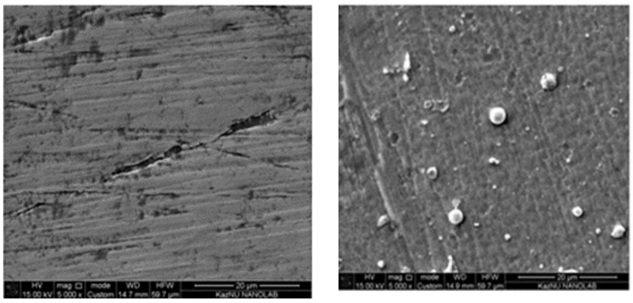

a) b)

a) the initial sample of carbon steel (×5000);
б) the structure of the carbon steel sample after coating surface by protective coating (×5000)

Figure 4 – Microstructure of the carbon steel sample

The developed virtual laboratory contains instructions and guidelines on conducting the experiment [6]. It includes the aim of the laboratory work, theory, the experiment equipment, a procedure of the experiment, a report. The experiment methodology is described in detail and the guidelines for the processing of the results are given.

Screenshot of the developed Virtual Physics Laboratory is presented on the Figure 5.

40

100 Presure * 10^(-4)

N	time, s	pressure, Pa	thickness,
1	100	1	384.9169
2	100	10	339.0128
3	100	100	395.9484
4	50	1	321.0364
5	40	10	363.5064
6	40	100	358.7885
7	40	100	331.6035

Figure 5 – Screenshot of the Virtual Physics Laboratory «Studying the plasma spraying»

In the virtual application, the panel of data input and calculation of the studied variables was established. Using it, students can change the course of the experiment, which in turn leads to a more detailed understanding of the essence of the studied laws.

Conclusion

Thus, proposed in this paper the method for surface modification of metallic materials using VDU-1 allows obtaining metallic coatings on substrates of structural steels and aluminum alloys with high performance characteristics and requires a small cost of production. The change in the internal structure and properties of the surface during plasma treatment were investigated by x-ray spectral analysis and electron microscopy was showed the presence of copper in all samples of steel and aluminum, there is also significant changes in percentage content of the main elements that may be associated with structural rearrangements in the surface layer after application of the protective coating and phase transitions.

The article discusses the successful example of the development of a virtual laboratory work in physics as part of such a laboratory application.

Acknowledgment

The studies presented in this paper was conducted under the applied research grant No3111 GF 4/2016 and No2622 GF4/2016.

References

1. A.M. Zhukeshov, N.N. Koval, A.U. Amrenova, A.T. Gabdullina, M. Mukhamedryskyzy, Zh.M. Moldabekov, S.K. Beysenbaev. Present status and perspectives of the using pulsed and electron beams for the hardening constructional steels // Journal of Engineering Thermophysics. – 2007. – Vol. 16. – P. 40-43.
2. V.V. Uglov, N.N. Cherenda, V.M. Anishyk, V.M. Astashinsky, N.T. Modifikasya materialov kompressionnimi plazmennimi potokami. – Minsk BGU, – 2013. – P. 248.
3. A.M. Zhukeshov. Plasma diagnostics in a pulsed accelerator used for material processing // Journal of Physics. Conference series. – 2007. – Vol. 63. – P. 12-14.
4. A.M. Zhukeshov, A.T. Gabdullina, A.U. Amrenova, K. Fermahan, K. Serik, N.N. Ahmetzhanova, Zh.K. Erenbayeva, Zh.R. Rysbekova. The specifics of coatings by pulsed arc method // Physical Science and Technology. – 2015. – Vol. 2. – P. 49-52.
5. Ye. Daineko, V. Dmitriyev. Software Module “Virtual Physics Laboratory” in Higher Education. 8th IEEE International Conference on Application of Information and Communication Technologies - AICT2014, Kazakhstan, Astana, 2014. – P. 452-454.
6. A.V. Trukhin. // Vidy virtualnykh kompyuternukh laboratoriy. Otkrytoe I distancionnoe obrazovanie. –2003. – Vol. 3. – P. 12–21.

International Journal of Mathematics and Physics 7, №2, 106 (2016)

UDC 523.98; 551.521:523; 551.590.21

[1]Morzabaev A., [1]Giniyatova Sh., [1]Shakhanova G., [1]Balabekov K.,
[1]Sakhabayeva S., [2]Makhmutov B., [2]Erkhov B.

[1]Faculty of Physics and Technical, L.N. Gumilyov Eurasian National University, Astana, Kazakhstan
[2]Lebedev Physical Institute, Moscow, Russia
*e-mail: giniyat_shol@mail.ru

Research of cosmic rays' variations in july-august 2016 with use of data of the carpet detector

Abstract. The paper reviews the CARPET cosmic ray detector placed into operation at physics and technical faculty of Eurasian National University in 2016. Observation data of the detector provide opportunity of researching nature of cosmic rays induced by processes on the Sun within interplanetary medium and earth's magnetosphere for different time intervals. It also considers results of analysis of cosmic rays' variations and solar flare activity in the period of July-August 2016 taken on the basis of the detector's experimental data, information of neutron monitor network and parameters of solar and geomagnetic activity. The dynamics of experimental data is considered.

Key words: cosmic ray, detector, telescope, astronomic complex, solar activity, secondary cosmic ray.

Introduction

In 2016 at physics and technical faculty of Eurasian National University named after L.N. Gumilyov (Astana, Kazakhstan, 51°10′48″ S, 71°26′45″ W; geomagnetic cutoff rigidity Rc~2,5GV), the first part of integrated unit for measuring flux density of general ionizing component of secondary cosmic rays - the CARPET detector - has been put into operation.

The detector [1] was designed and created in Physical Institute of Academy of sciences named after P.N. Lebedev in the framework of agreement on international cooperation between PIAS(Russia) and ENU (Kazakhstan).

The CARPET cosmic ray detector is designed for continuous monitoring of general ionizing component of secondary cosmic rays flux at the level of the Earth. Experimental data allow conducting analysis of secondary cosmic rays fluxes' variations, analyzing influence of geomagnetic and solar activity on the processes defining behavior of cosmic rays in near-Earth space and Earth's atmosphere, carrying-out monitoring of its radiation situation.

In 2006 prototypes of the detector CARPET/ASTANA – CARPET/CASLEO were installed in astronomical complex of CASLEO (Argentina), in 2009 CARPET/GCR was installed in European Nuclear Research Center (at Geneva, Switzerland) [2-4].

In the present work there are results of cosmic rays' variations within the period of July-August 2016 on experimental data of CARPET/ASTANA detector.

Experimental device and measured methods

The CARPET cosmic ray detector is the unit of 120 gas-discharged STS-6 counters mounted in vertical blocks (telescopes) located on metal platform. Each block consists of 10 counters and 7mm. aluminum filter that separates horizontal layer of upper counters (5 pieces) and lower counters (5 pieces). The filter absorbs all low-energetic particles (radioactivity) and passes only energetic particles of cosmic rays. The general view of the unit is shown in Figure 1.

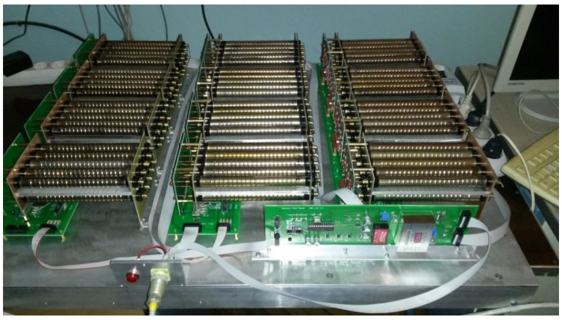

Figure 1 – General view of the CARPET cosmic ray detector

The CARPET detector is the integral register-summator of charged particles' flux: it counts and accumulates impulses from the flux of flying charged particles in the entire area of the device. The detector consists of 2 detecting vertical modules united with registering and summarizing electronics. The two-detector module – «telescope» - possesses upper and lower gas-discharged counters. The summarizing electronics of CARPET registers and accumulates impulses from the telescopes in such a way that:

– all the impulses from upper counters of all CARPET telescopes are summarized in the counter of 1st channel (data channel CH1);

– all the impulses from lower counters of all CARPET telescopes are summarized in the counter of 2nd channel (CH2 - channel);

– all the coincidences of simultaneous actuations of upper and lower counters of any telescope are summarized in the counter of 3rd channel(channel TEL). All the counters are placed into single rectangular-shaped case.

In table 1 there are energetic characteristics of charged particles' flux registration.

Table 1 – Registration ranges for charged particles of counter-telescope on the basis of STS-6 gas-discharged counter

	SinglecounterCTC-6 (CH1 andCH2 -channels)	Counter-telescope CTC-6 (TEL – channel)
electrons	>=0.2 MeV	>=5 MeV
protons	>=5 MeV	>=30 MeV

The CARPET detector consists of own detecting module described above, module of calculating and interfacing electronics and a computer.

All the interactions with the detector are performed by PC program via single standard serial communication port RS-232. The program of the detector performs full control for strokes of continuous fully-automatic experiment, including visualization of experiment's stroke on the screen of control PC.

The device logs time (milliseconds) of particle registration in data channel, the reference point is 00:00:00 of every day.

The CARPET complex includes telemetering sensors (temperature, pressure, voltage parameters U- 5V, 12V, 380V).

It also performs recalculation of data corrected to temperature and barometric effect with account of complex telemetering data.

Measurement data is logged, processed and recorded with help of specialized software. At the end of each day it forms two files: the file of particle registration data by three channels and the telemetering data file.

For processing of experimental data the CARPET detector uses a package of programs realized in R environment. At the current time the R language is in fact being a standard in the area of statistic data analysis[5].

The program pack includes:

a) pre-processing of experimental data:

– uploading and conversion of data into the system;

– data analysis – emissions, missing values, normality of distribution, etc.;

– standardization of experimental data;

b) Experimental data base formation (daily, monthly, annual);

c) Experimental data analysis;

d) visualization of obtained results (tables, diagrams, statistical values, etc.).

In figure 2 there is temporal variation of general ionizing component of secondary cosmic rays flux in three channels of the CARPET detector as on July 2016. The time of data integrator (accumulation) is 1 min.

In figure 3 there is dynamics of deviations in three channels of the CARPET detector (as on July 2016).

As opposed to land neutron monitors the CARPET detector is sensitive to low energetic charged secondary component of cosmic rays formed by primary galactic and solar cosmic rays in Earth's atmosphere.

In figure 4 there is temporal variation of data of telescope and neutron monitor in Almaty as on July 2016.

In figure 6 (a,b,c) there is temporal variation of general ionizing component of secondary cosmic rays flux in three channels of the CARPET detector as on July-September 2016 and the dynamics of variation of K-index - the geomagnetic activity [6].

In figure 5 there is temporal variation of data of counter and neutron monitor in Almaty as on July 2016.

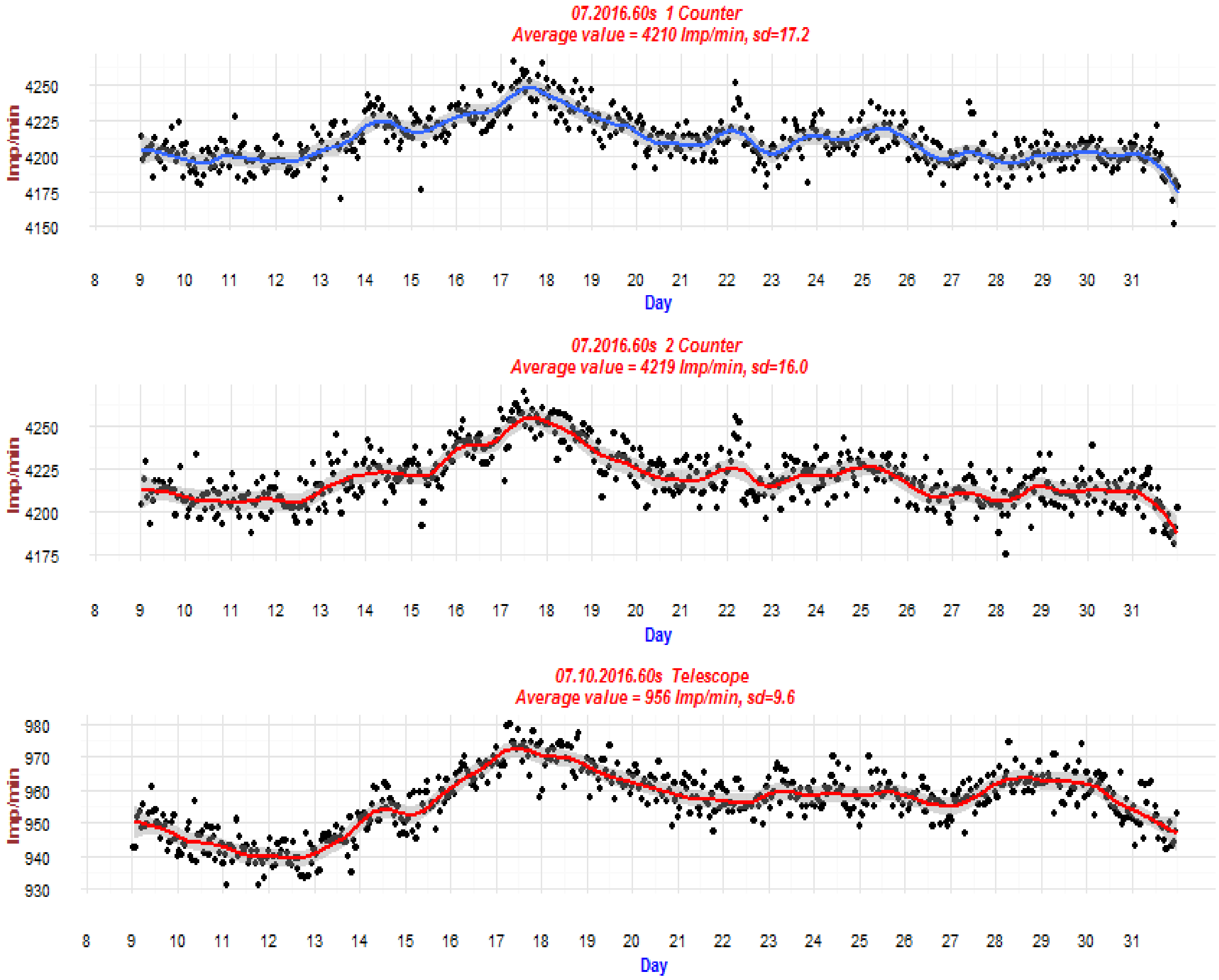
07.2016.60s 1 Counter
Average value = 4210 Imp/min, sd=17.2

07.2016.60s 2 Counter
Average value = 4219 Imp/min, sd=16.0

07.10.2016.60s Telescope
Average value = 956 Imp/min, sd=9.6

Figure 2 – Temporal variation of general ionizing component of secondary cosmic rays flux in three channels of the CARPET detector as on July 2016

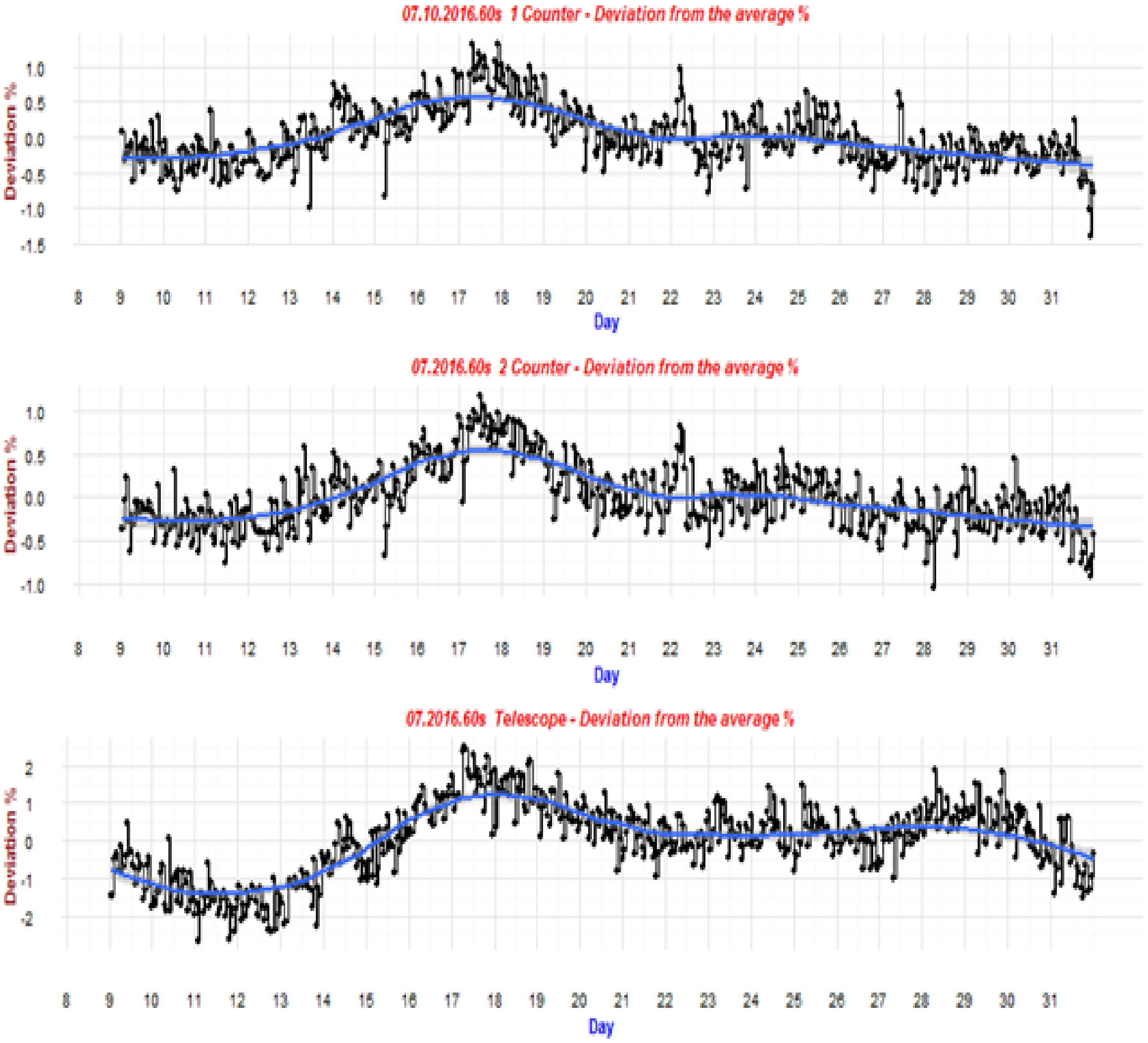

Figure 3 – Dynamics of deviations in three channels of the CARPET detector as on July 2016

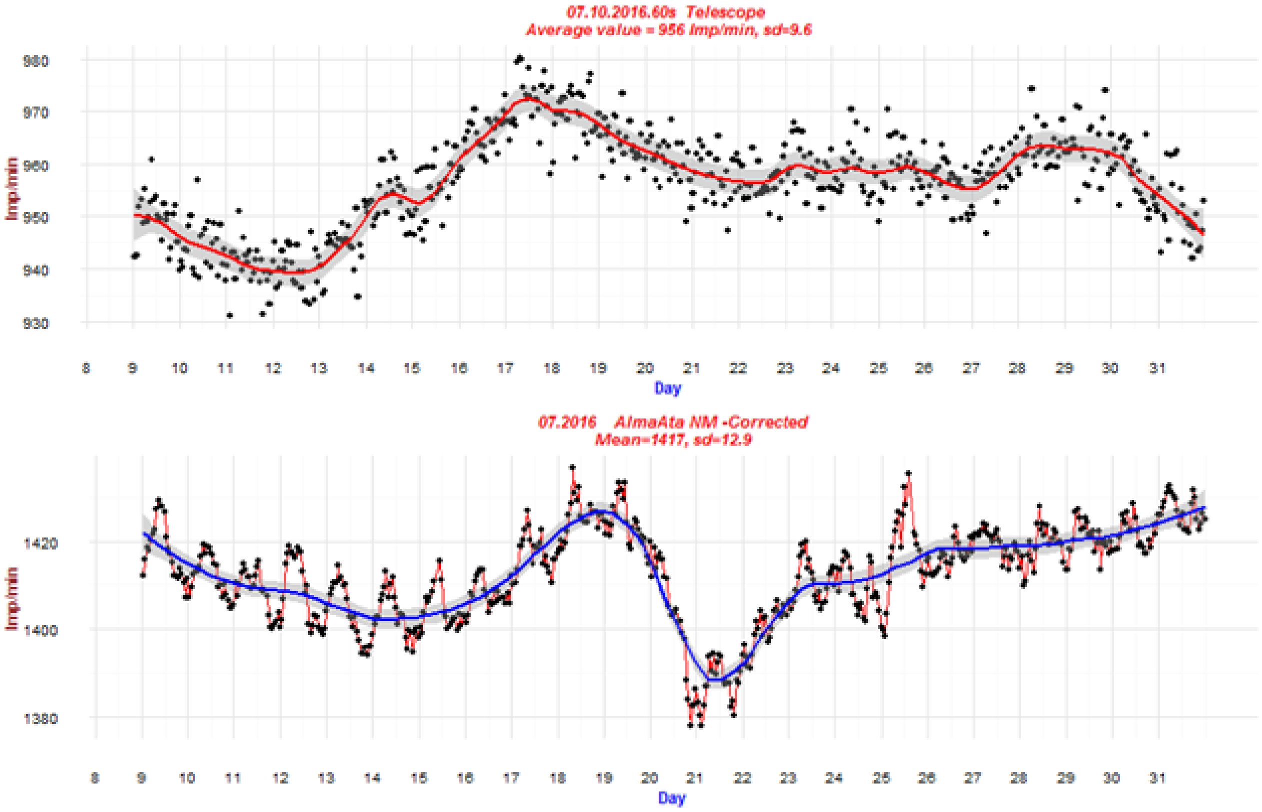

Figure 4 – Temporal variation of data of telescope and neutron monitor in Almaty (July 2016)

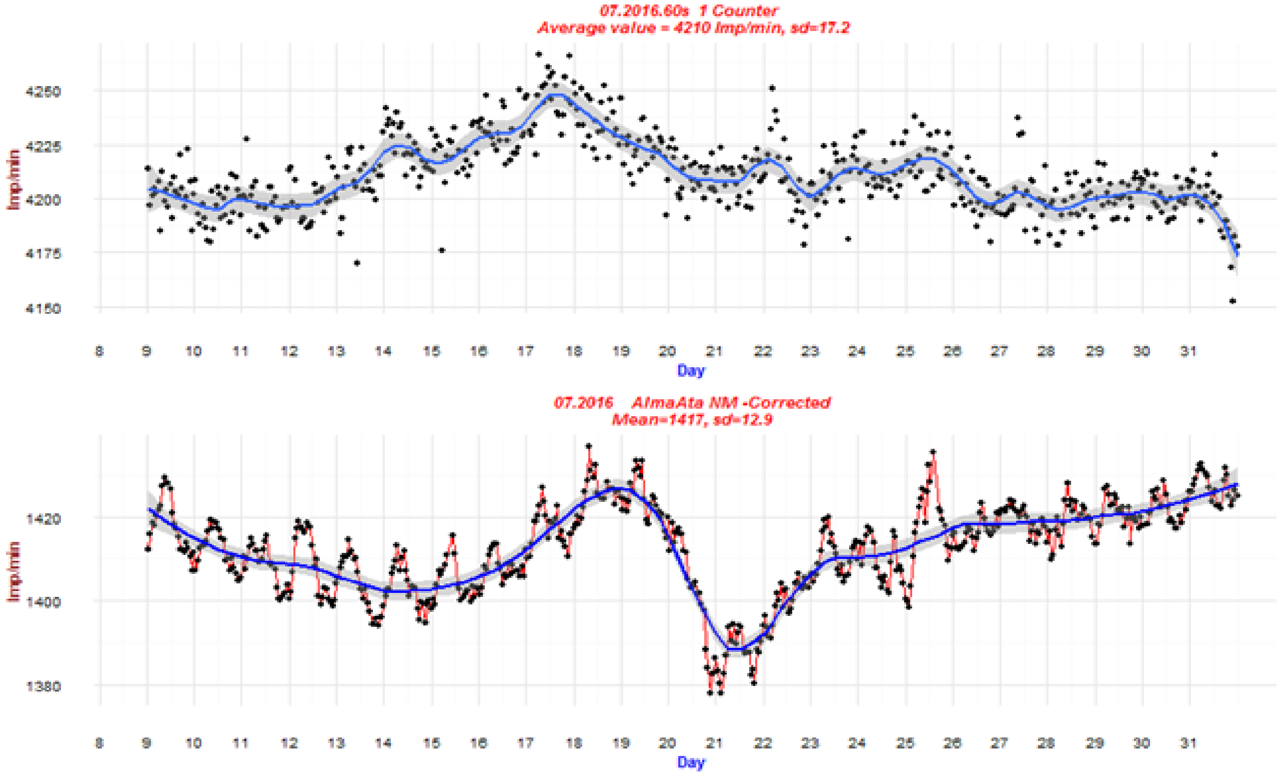

Figure 5 – Temporal variation of data of counter and neutron monitor in Almaty (July 2016)

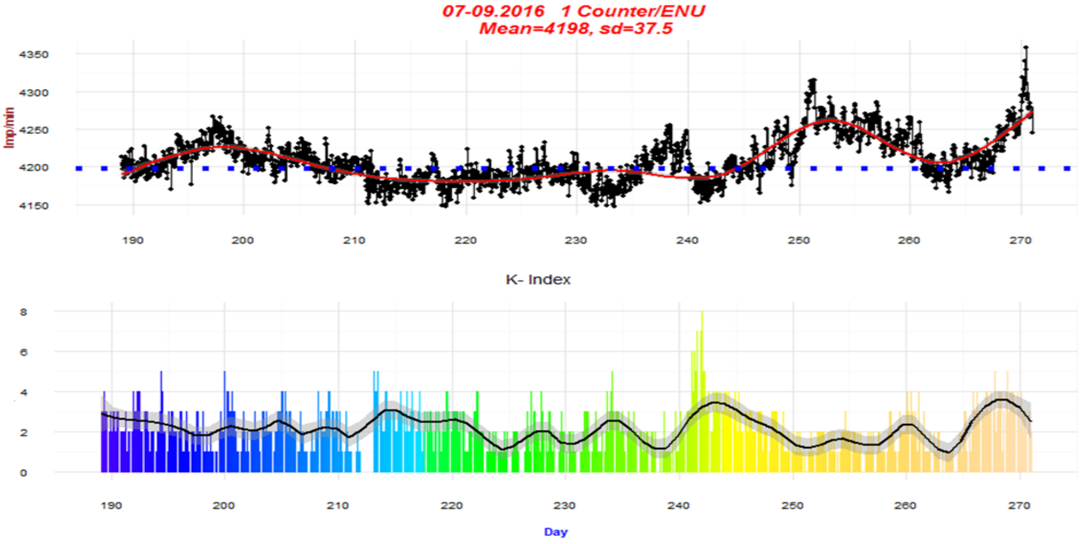

a)

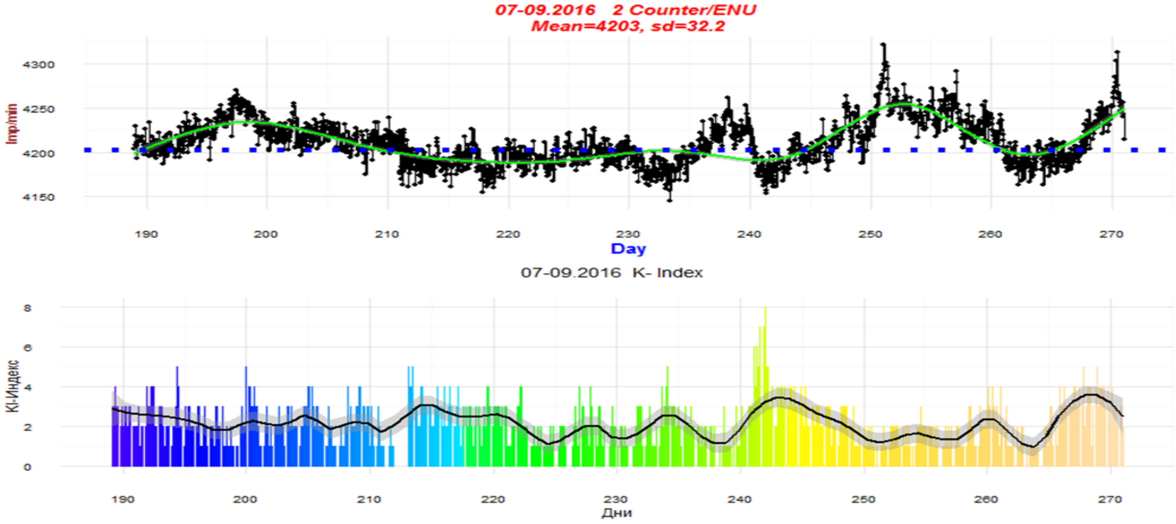

b)

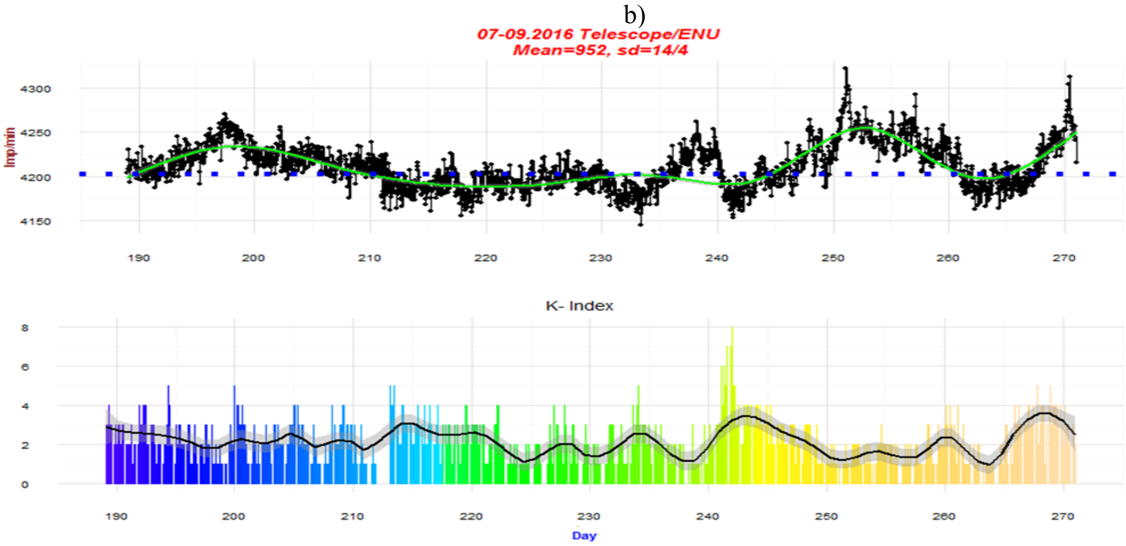

Figure 6 – Temporal variation of general ionizing component of secondary cosmic rays flux in three channels of the CARPET detector and the dynamics of variation of K-index - the geomagnetic activity

Experimental data of secondary cosmic rays of the CARPET detector provides researching wide time spectrum of variations of secondary cosmic rays - the short-term ones (Forbush decreases, solar flares, etc.) and long-term ones (27-day, 11-year, 22-year, etc.).

In figures 7-8 there are measurements of counting rate in TEL channel of the CARPET device and the data of land neutron monitors (NM Data Base – NMDB) in Almaty and Yakutsk.

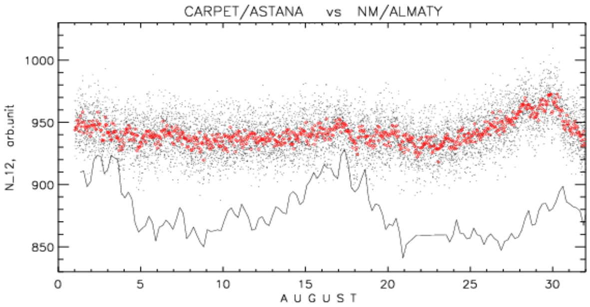

Figure 7 – Counting rate in TEL channel of the CARPET detector and neutron monitor of Almaty as on 2016

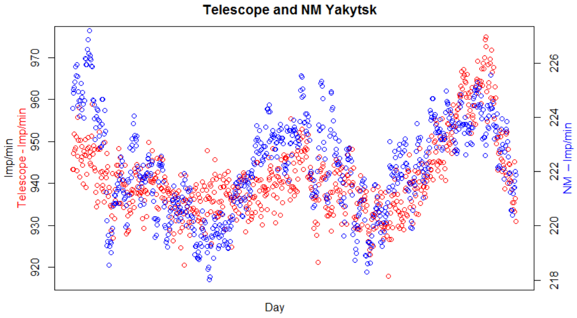

Figure 8 – Counting rate in TEL channel of the CARPET detector and neutron monitor of Yakutsk.

Conclusions

In the paper there is a review of the CARPET cosmic ray detector that has been put into operation at physics and technical faculty of Eurasian National University named after L.N.Gumilyov in 2016 within the framework of scientific project. The dynamics of experimental data is considered.

Acknowledgment

This work was supported by the Ministry of Education and Science of KR, grant №5230 GF4.

References

1. Mizin S.V., Makhmutov V.S., Maksumov O.S.// Kratk. Soobshch.Fiz. – 2011. – Vol.2. – P. 9-17.
2. http://www.casleo.gov.ar
3. Kirkby J. et.al. Role of sulphuric acid, ammonial and galactic cosmic rays in atmospheric aerosol nucleation // Nature.– 2011. – Vol. 476. – P. 429-1409.
4. De Mendonça R.R., Raulin J.-P., Bertoni F.C.P. Echer E., Makhmutov V.S., Fernandez G. Long-term and transient time variation of cosmic ray fluxes detected in Argentina by CARPET cosmic ray detector // J. Atmos. Solar-Terrestr. Phys. – 2011. – Vol. 73. – P. 11–12. – P.1410–1441.
5. R Development Core Team. R: A language and environment for statistical computing. R Foundation for Statistical Computing, Vienna, Austria. – 2009. ISBN 3-900051-07-0.
6. http://www.swpc.noaa.gov / products / planetary-k-index